



저작자표시-비영리-변경금지 2.0 대한민국

이용자는 아래의 조건을 따르는 경우에 한하여 자유롭게

- 이 저작물을 복제, 배포, 전송, 전시, 공연 및 방송할 수 있습니다.

다음과 같은 조건을 따라야 합니다:



저작자표시. 귀하는 원저작자를 표시하여야 합니다.



비영리. 귀하는 이 저작물을 영리 목적으로 이용할 수 없습니다.



변경금지. 귀하는 이 저작물을 개작, 변형 또는 가공할 수 없습니다.

- 귀하는, 이 저작물의 재이용이나 배포의 경우, 이 저작물에 적용된 이용허락조건을 명확하게 나타내어야 합니다.
- 저작권자로부터 별도의 허가를 받으면 이러한 조건들은 적용되지 않습니다.

저작권법에 따른 이용자의 권리는 위의 내용에 의하여 영향을 받지 않습니다.

이것은 [이용허락규약\(Legal Code\)](#)을 이해하기 쉽게 요약한 것입니다.

[Disclaimer](#)

Ph.D. DISSERTATION

**First-principles Study on the Surface
Chemistry for Catalytic Reaction
Mechanisms**

By

Tae Hyung Lee

August 2021

**DEPARTMENT OF MATERIALS SCIENCE AND
ENGINEERING**

COLLEGE OF ENGINEERING

SEOUL NATIONAL UNIVERSITY

First-principles Study on the Surface Chemistry for Catalytic Reaction Mechanisms

Advisor: Prof. Ho Won Jang

**By
Tae Hyung Lee**

A thesis submitted to Graduated Faculty of Seoul National University in
partial fulfillment of the requirements for Degree of Doctor of Philosophy

Department of Materials Science and Engineering

August 2021

Approved

by

Chairman of Advisory Committee: Jin Young Kim

Vice-Advisory Committee: Ho Won Jang

Advisory Committee: Soo Young Kim

Advisory Committee: Donghwa Lee

Advisory Committee: Jeong-Yun Sun

Abstract

With the rise of the energy crisis worldwide, there have been vigorous attempts to use energy in an efficient way. The energy crisis is strongly related to the dependence on fossil-based fuels for energy generation. It includes not only the energy shortage in the future but also the occurrence of pollution, such as greenhouse gas. As an answer to the crisis, renewable energy emerged as the solution. Among various renewable energies, solar energy is spotlighted with its universal availability, which is independent of geographical and environmental features. Still, the utilization of solar energy is suffering from its low efficiency, during the conversion to another energy source for storage. Therefore, to fully exploit the energy in the sunlight, intensive approaches to optimize the kinetics and thermodynamics of the conversion reaction.

To maximize the efficiency of the reaction, the application of the catalyst is essential. Depending on the type of reaction, the optimal catalyst material varies, and intensive studies are carried out to find out the catalyst candidates for each reaction. In most cases, noble metal elements are known to be the best catalyst with high activity and stability. However, due to the high cost of noble metals, most researches are focused on substituting noble metals. To catch up the superior properties of the noble metal catalyst, various modification strategies are applied to the catalyst materials, to further enhance their properties.

Along with the experimental approaches, simulation works also have been extensively carried out. Among various simulation methodologies, density functional theory-based first-principles calculations simulation is the most

commonly performed to predict the catalytic property of materials. As the catalytic reaction is directly related to the atomistic interaction of reactants at the catalyst surface, the appropriate simulation on surface chemistry can effectively reflect the catalytic property of the material. To date, investigation on the reaction mechanism on the pristine catalyst material has been covered by numerous studies. However, systematic approaches on catalysts to which the modification strategy is applied are relatively insufficient.

Herein, in this manuscript, the reaction mechanism of the catalysts modified with various strategies is investigated. Strategies are categorized as structural, atomistic modification, and co-catalyst application. In chapters 2 to 4, the enhancement of the catalytic property will be explained for water splitting reaction, CO₂ reduction reaction, and chemoresistive gas sensing based on the demonstration of the influence of each modification strategy.

In chapter 2, the influence of the face and optimal dopant selection is presented through the goethite oxygen evolution reaction (OER) catalyst. The pristine and transition metal-doped goethites were synthesized with the electrodeposition method. Synthesized goethites had similar morphology, surface area, and phase which are confirmed by various characterizations. The overpotential value was measured as 480 mV, 490 mV, 510 mV, and 530 mV for Co-doped, Ni-doped, Mn-doped, and pristine goethite respectively. To explain the trend of overpotential between goethites with various dopants, a first-principles calculations simulation was performed. To figure out the facet dependence of the goethite in catalytic property, (001), (021), and (111) surface models are constructed. With the lowest surface energy and overpotential, (001) surface of goethite is turned out to be the most influential surface for OER. Based on the modeled (001) surface, transition

metal atoms are substituted at the active site of goethite to investigate the atomistic doping effect on overpotential. From the calculation of OER 4 step energy levels, overpotential for each Co-doped, Ni-doped, Cr-doped, Mn-doped, and pristine goethite are determined as 0.4 V, 0.72 V, 0.72 V, 0.83 V, and 0.94 V, which has the same trend with experimental overpotential values. The trend of calculated overpotential is further explained through the energy level of adsorbed oxygen p-band center which can be the effective descriptor for the catalytic property.

In chapter 3, the simulation on CO₂ reduction reaction of Bi decorated GaN nanowire (NW) is carried out to explain the role of Bi and synergetic effect between GaN and Bi. From the experimental result achieved by W. J. Dong, by decorating the Bi nanoparticles (NPs) on GaN NW, it was possible to acquire superior selectivity and photocurrent for the formic acid generation. By comparing the performance of GaN/Si, Bi/Si, and Bi/GaN NW/Si samples, we could conclude that the Bi decoration contributes to the strong formic acid selectivity, while high photocurrent is achieved only from the combination of GaN and Bi. To understand the mechanism of enhancement in the selectivity and photocurrent, GaN/Si, Bi/Si, and Bi/GaN NW/Si samples are modeled as GaN with (001) surface, Bi₂O₃ with (010) surface, and GaN-Bi₂O₃ composite based on characterization results. The improvement of the selectivity toward the formic acid could be demonstrated by the reaction barrier calculation. As the reaction pathway mainly diverges into the formic acid generation pathway and the carbon monoxide generation pathway, the intermediate state for each pathway is presented as the oxygen bonding structure (*OCHO) and the carbon bonding structure (*COOH). Calculated reaction barrier values for the formic acid and the carbon monoxide generation were 1.93 eV, 2.10 eV on GaN (001) surface, and 1.93 eV, 1.04 eV on Bi₂O₃ (010) surface. Comparing

the reaction barrier for two different products on GaN (001) surface and Bi₂O₃ (010) surface, the difference of the reaction barrier was larger for Bi₂O₃, with the much lower barrier for the formic acid generation. Thus, it was concluded that the favorable reaction steps on Bi₂O₃ for the formic acid generation lead to the enhanced selectivity of Bi decorated samples. The photocurrent increase is mainly explained by the synergetic effect of GaN and Bi₂O₃. From the density of states plotted from GaN-Bi₂O₃ composite, the shift of conduction band to lower energy level is observed, which confirmed to be the contribution of surface Bi₂O₃. As the Bi₂O₃ has a conduction band below that of GaN, the extra built-in potential for an electron at the interface of GaN-Bi₂O₃ is generated, which improves the charge transfer to the Bi₂O₃ side. With the visualization of the differential charge density of GaN-Bi₂O₃, the charge accumulation at the interface, especially near the Bi₂O₃ is observed. Thus, we could conclude that a large increase in photocurrent for Bi/GaN NWs/Si is due to the improvement of charge transfer by forming the heterojunction.

In chapter 4, the theoretical approach to demonstrate the mechanism of selectivity change in the noble metal decorated MoS₂ gas sensor is presented. Fabrication, sensor measurement, and characterization are done by S. Y. Park and T. H. Kim. From the synthesized MoS₂ sensors with the noble metal decoration, the change of selectivity can be noticed by the response plot. For the pristine MoS₂, high selectivity toward ammonia is observed. When the noble metal particle is decorated, the response for gases, especially hydrogen and ammonia, changed. Pd and Pt decoration showed similar change, the increase in hydrogen response and decrease in ammonia response. In the case of Au decoration, only the response of ammonia stiffly decreased. As a result of variation in response, for Pd-decorated MoS₂, high selectivity toward hydrogen is acquired while Au-decorated MoS₂ achieved mild

selectivity for ammonia. As the dynamic change in response is observed only for ammonia and hydrogen gas, the simulation part focused on explaining the sensitivity variation of the two gases. To understand the strong ammonia selectivity of the pristine MoS₂, the basal plane and edge site are modeled for gas adsorption. As a result, the edge site of MoS₂ is found to be the major binding site for hydrogen and ammonia, and among the two gases, the binding energy of ammonia was larger more than 3 times than hydrogen, which leads to selective sensing for ammonia. For the modeling of decorated noble metal particles, the particle size and surface oxidation based on the characterization results are considered. With the large particle size of 20~30 nm and Pd-O bonding from XPS spectra, Pd is modeled as the bulk-like metal slab with a surface oxygen layer. In the case of Pt and Au particles, due to the small size of 2~3 nm, the nanocone cluster model is designed and surface oxidation is applied for Pt nanocone. Similar to the trend in the response curve, the binding energy of hydrogen on Pd and Pt increases, as the surface oxygen becomes the favorable binding site for the hydrogen. On the other hand, the tendency of the binding energy of ammonia mismatches with that of the response curve, while the binding energy on noble metal models is all decreased when compared to the MoS₂ edge site. We concluded that the decrease of the ammonia response for noble metal decorated samples is caused by the binding site blocking of decorated noble metals. To determine the degree of MoS₂ edge coverage for each noble metal, the clustering energy, and surface energy were calculated. Both clustering energy and surface energy lead to the conclusion that Pt particles are more favorable to be agglomerated while Au particles prefer to disperse along the MoS₂ edge, vigorously blocking the binding of ammonia.

In this dissertation, we presented a theoretical approach to demonstrate the

influence of various catalyst modification strategies on catalytic performance. Based on the experimental measurement and characterization, various catalyst reaction mechanisms are simulated with appropriate modeling, taking in consideration of size, facet, surface termination, and other variables. We believe that the extensive approach of studies in this dissertation can inspire further interpretation on the mechanism for the catalytic improvement for future works.

Keyword : First-principles calculations, Surface chemistry, Water splitting, CO₂ reduction, Gas sensor

Student Number: 2016-20817

Table of Contents

Abstract	i
Table of Contents	vii
List of Tables	x
List of Figures	xii
Chapter 1	1
1.1. Background of the Research	2
1.2. Objective of the Thesis	5
1.3. References	8
Chapter 2	9
2.1. Introduction	10
2.2. Theoretical Approach	14
2.2.1. Computational Details.....	14
2.2.2. Bulk Properties of the Goethite.....	16
2.2.3. Surface Modeling.....	18
2.2.4. Thermodynamics of OER.....	20
2.3. Experimental Section	23
2.3.1. Film Preparation.....	23
2.3.2. Characterization.....	25
2.3.3. Electrochemical Measurement.....	26
2.4. Result and Discussion	27
2.4.1. Surface Determination.....	27
2.4.2. OER on the Pristine Goethite.....	30
2.4.3. OER on the TM-doped Goethite.....	33
2.4.4. The Correlation between OER Acitivity and Oxygen p-band center.....	40
2.4.5. Structural and Electrochemical Characterization.....	42
2.5. Conclusion	53

2.6. References	55
Chapter 3	65
3.1. Introduction	66
3.2. Experimental Results	69
3.2.1. Fabrication of Bi/GaN NWs/Si.....	69
3.2.2. Characterization of Bi/GaN NWs/Si.....	70
3.2.3. Photoelectrochemical Measurement of Bi/GaN NWs/Si.....	74
3.3. Theoretical Approach	79
3.3.1. Computational Details.....	79
3.3.2. Surface Modeling.....	80
3.3.3. Reaction Pathway of CO ₂ Reduction.....	82
3.4. Result and Discussion	86
3.4.1. Surface Determination.....	86
3.4.2. CO ₂ Reduction on the GaN (100) Surface.....	90
3.4.3. CO ₂ Reduction on the Bi ₂ O ₃ (010) Surface.....	92
3.4.3. CO ₂ Reduction on the GaN-Bi ₂ O ₃ Composite Structure.....	95
3.5. Conclusion	99
3.6. References	101
Chapter 4	104
4.1. Introduction	105
4.2. Experimental Results	107
4.2.1. Fabrication of the Noble Metal NP Decorated MoS ₂	107
4.2.2. Characterization of the Noble Metal NP Decorated MoS ₂	109
4.2.3. Gas Sensing Properties of the Noble Metal NP Decorated MoS ₂	112
4.3. Theoretical Approach	117
4.3.1. Computational Details.....	117
4.3.2. Details on the System Modeling.....	118
4.3.2. Details on the Binding Energy Calculation of Gas Molecules.....	120

4.4. Result and Discussion	122
4.4.1. Gas Adsorption on the Pristine MoS ₂	122
4.4.2. Gas Adsorption on the Bulk-like Noble Metal Slab Model....	127
4.4.3. Gas Adsorption on the Noble Metal Nanocone Cluster Model.....	132
4.4.4. Coverage Effect of the Noble Metal NPs on the NH ₃ Gas Sensitivity.....	136
4.5. Conclusion	139
4.6. References	141
Abstract in Korean	144

List of Tables

Table 2.1. U_{eff} values for the dopants in goethite based on the oxide formation energy.....	15
Table 2.2. Gibbs free energy of the fully relaxed goethite unit cell with antiferromagnetic and ferromagnetic configuration.	17
Table 2.3. The lattice parameter of fully relaxed unit cell of goethite obtained from the DFT calculation and experiment values.	17
Table 2.4. DFT total energy, zero-point energy and entropic contribution of H_2O , H_2 molecules and reaction intermediates. Entropic contribution are values under the standard conditions which are $T=298\text{K}$, $P=1$ bar.	22
Table 2.5. Magnetic moments of various transition metals in different structures obtained from the GGA+U calculation. All the transition metals are in octahedron configuration and U values used in this paper are equally applied.....	29
Table 2.6. The total contribution of zero-point energy and entropic contribution for each OER step.....	31
Table 2.7. Magnetic moment values with the oxidation state of active site iron for each interstate and the Gibbs energy difference for 4 steps. The overpotential value is calculated by dividing the highest Gibbs energy difference value with e and subtracting 1.23 V. The Gibbs free energy of the potential determining step is colored with red. The oxidation state of Fe is determined based on the magnetic moment value of various oxidation state Fe in Table 2.5.	31
Table 2.8. Magnetic moment values with the oxidation state of adjacent Fe atom in dopant doped goethite for each interstate and the Gibbs energy difference for 4 steps.....	34
Table 2.9. Magnetic moment values with the oxidation state of introduced dopant atom for each interstate and the Gibbs energy difference for 4 steps.	37
Table 2.10. SEM EDS result of Mn, Co, and Ni-doped goethite.....	44

Table 3.1. Calculated total energy and zero-point energy of reactants and product molecules.....	85
Table 4.1. Response values for various gases measured from pristine MoS ₂ and noble metal decorated MoS ₂ gas sensors.....	114
Table 4.2. H ₂ and NH ₃ gas response change in noble metal decorated MoS ₂ sensors when compared to the pristine MoS ₂ sensor. The amount of response change is presented in brackets.....	114
Table 4.3. Calculated DFT energy and zero-point energy of H ₂ and NH ₃ gas molecule.....	121
Table 4.4. Calculated zero-point energy of adsorbed H ₂ and NH ₃ gas molecule on MoS ₂ and noble metal surface.....	121
Table 4.5. Adsorption energy of the noble metal atom at the MoS ₂ basal plane and edge site.....	136
Table 4.6. Surface energy of the Au, Pd, and Pt slab with (111) surface.....	138

List of Figures

Figure 1.1. The process toward high-throughput screening and examples of descriptors for water splitting.	4
Figure 1.2. Overall flow of the dissertation.	7
Figure 2.1. The bandgap of the goethite with various U_{eff} values.	15
Figure 2.2. The unit cell of orthorhombic structure goethite. The spin state of each iron atom is represented on the atom. Iron atoms with + mark have the up-spin while those with – mark have down-spin. (a) Ferromagnetic configuration and (b)-(d) 3 antiferromagnetic configurations are presented.	16
Figure 2.3. (a) Surface energy of (001), (021), (111) surfaces with various terminations. Atomic structures of (b) (001) surface, (c) (021) surface, and (d) (111) surface with OH-H surface termination. The adsorption sites for OER intermediates are marked with green circle.	27
Figure 2.4. Schematic and magnetic configuration of the Fe^{3+} (a) octahedral geometry and (b) square pyramidal geometry.	29
Figure 2.5. Four intermediate states of the 4-step oxygen evolution reaction on the H and OH adsorbed (001) surface of goethite.	30
Figure 2.6. Free energy diagrams of the (a) (001), (b) (021), and (c) (111) surface. The free energies of each intermediated state under zero bias, ideal bias of 1.23 V for OER, and minimum bias for OER are denoted with black, red, and blue colors, respectively.	32
Figure 2.7. (a) Dopant incorporated slab model of (001) goethite surface. (b) Free energy diagram of dopant-doped goethites (001) surface.	33
Figure 2.8. The top view of the dopant-doped (001) surface goethite slab. Two different active sites for OER are represented as dopant atom site, adjacent Fe site.	34

Figure 2.9. Overpotential values of pristine, dopant doped goethites with surface dopant concentration of 25% (colored), and 50% (slash line).	35
Figure 2.10. Overpotential value of pristine and Co-doped goethite from GGA+U and HSE06 calculation.....	37
Figure 2.11. (a) Scaling relation between ΔG_{OOH^*} , ΔG_{OH^*} and (b) volcano curve based on the OER of pristine and dopant-doped goethite. The hollow symbols stand for the adjacent Fe site of dopant-doped goethites. The black, red, blue, green, orange colors denote pristine and Mn, Cr, Co, Ni-doped goethite, respectively.	39
Figure 2.12. (a) Free energy diagram between the OH* state and the OOH* state (b) Oxygen p-band center of the adsorbed oxygen at the active site for pristine goethite and dopant-doped goethites.	40
Figure 2.13. SEM image of (a) pristine, (b) Mn-doped, (c) Co-doped, and (d) Ni-doped goethites. (e) XRD data of pristine and dopant doped goethites. FTO reference peaks are marked with a black circle.....	42
Figure 2.14. Linear Sweep voltammograms of pristine and dopant-doped goethites.....	45
Figure 2.15. Tafel plot of pristine and dopant-doped goethites.....	47
Figure 2.16. Capacitive currents of the pristine and dopant-doped goethites.	49
Figure 2.17. Nyquist diagrams of EIS for pristine and dopant-doped goethites in 1M NaOH.....	51
Figure 3.1. Reaction pathways of the CO ₂ reduction reaction by S. Nitopi et al.....	68
Figure 3.2. SEM images of the (a) GaN NWs and, (b) Bi NPs decorated GaN NWs.....	70
Figure 3.3. TEM images of Bi NPs decorated GaN NWs.	71
Figure 3.4. XPS spectra of GaN NWs, Bi/GaN NWs, and Bi/GaN NWs after CO ₂ reduction reaction.	73

Figure 3.5. Band alignment diagram of the Bi/GaN NWs/Si.	74
Figure 3.6. Faradaic efficiency for CO ₂ reduction reaction products of (a) GaN NWs/Si, (b) Bi/Si, and (c) Bi/GaN NWs/Si sample.....	76
Figure 3.7. Partial current density of photoelectrochemical CO ₂ reduction reaction products for (a) GaN NWs/Si, (b) Bi/Si, and (c) Bi/GaN NWs/Si.	77
Figure 3.8. Initial steps of the CO ₂ reduction reaction.....	83
Figure 3.9. (a) Calculated binding energy of various adsorbates on the GaN (001) surface. (b) Top view image and (c) side view image of the water molecule chemisorbed GaN (001) surface.....	87
Figure 3.10. (a) Calculated binding energy of H ₂ O chemisorption with various coverage on the GaN (001) surface. (b) Top view image and (c) side view image of the GaN (001) surface fully covered with the chemisorbed water molecule.....	87
Figure 3.11. (a) Calculated binding energy of various adsorbates on the Bi ₂ O ₃ (001) surface. (b) Top view image and (c) side view image of the water molecule chemisorbed Bi ₂ O ₃ (001) surface.....	88
Figure 3.12. (a) Top view image and (b) side view image of the GaN-Bi ₂ O ₃ composite with surface water chemisorption.....	89
Figure 3.13. (a) Reaction intermediate binding site for each reaction pathway. (b) Potential energy diagram of the carbon monoxide and formic acid generation on the GaN (001) surface. (c) The optimized structure of reaction intermediate binding for each pathway.....	91
Figure 3.14. (a) Potential energy diagram of the carbon monoxide and formic acid generation on the Bi ₂ O ₃ (010) surface. (b) The optimized structure of reaction intermediate binding for each pathway.....	92
Figure 3.15. Scheme of the reaction intermediate bond strength with GaN or Bi ₂ O ₃	94
Figure 3.16. (a) Potential energy diagram of the carbon monoxide and formic acid generation on the GaN-Bi ₂ O ₃ composite. (b) The optimized structure of reaction intermediate binding for each pathway.....	95

Figure 3.17. (a) Density of states diagram for the GaN slab and GaN with Bi ₂ O ₃ . (b) Partial density of states diagram for GaN with Bi ₂ O ₃	96
Figure 3.18. (a) Band alignment diagram of Bi ₂ O ₃ /GaN NWs/Si based on the calculated GaN-Bi ₂ O ₃ composite density of states. (b) Visualized differential charge density with its linear plot.	98
Figure 4.1. Schematic illustration of the noble metal decorated MoS ₂ synthesis and energy diagram showing the work function of MoS ₂ with reduction potential of each noble metal.	108
Figure 4.2. HRTEM images of MoS ₂ and synthesized noble metal particles with the diffraction pattern acquired from FFT.....	110
Figure 4.3. Low magnification TEM images and STEM images of decorated noble metal particles.....	110
Figure 4.4. XPS spectra of the (a) Au-decorated MoS ₂ , (b) Pd-decorated MoS ₂ , and (c) Pt-decorated MoS ₂ samples.....	111
Figure 4.5. The response curves of (a) pristine MoS ₂ , (b) Au-decorated MoS ₂ , (c) Pd-decorated MoS ₂ , and (d) Pt-decorated MoS ₂	113
Figure 4.6. Polar plot of response values acquired from pristine MoS ₂ and noble metal decorated MoS ₂ sensors.	116
Figure 4.7. Adsorption site of the (a) NH ₃ molecule and (b) H ₂ molecule on the MoS ₂ basal plane.....	122
Figure 4.8. (a) Top and side view of the pristine MoS ₂ . Edge energy of (b) Mo-edge and (c) S-edge with various number of sulfur atoms.....	124
Figure 4.9. (a) The structure of MoS ₂ edge model with the most stable edge termination. (b) H ₂ and NH ₃ molecule binding energy at MoS ₂ basal plane and edge site.....	126
Figure 4.10. Side and top view of the bulk-like noble metal slab with (111) surface. Inequivalent oxygen adsorption sites of FCC, HCP and ontop sites are colored with red, blue and silver.....	127
Figure 4.11. (a) Oxygen adsorption energy on various sites of Pd and Pt (111) surface slab. (b) Oxygen adsorption energy on FCC site of Pd and Pt	

(111) surface slab with variety of coverages. 128

Figure 4.12. Top view of the bulk-like metal slab for various oxygen coverage, respectively (a) 25 %, (b) 50 %, (c) 75 %, and (d) 100 %. The metal atoms at the outermost layer are colored with dark gray while the other metal atoms are light gray and oxygen atoms are red. The unit cell used for calculation is marked with green line. 129

Figure 4.13. Top view of the surface structure of (a) Pd and Pt bulk-like slab and (b) Au bulk-like slab which used for the gas molecule binding energy calculation. The outermost metal atoms are colored with dark grey and oxygen atoms are colored with red. 129

Figure 4.14. Comparison of calculated binding energy from bulk like noble metal slab and experimental response value for (a) H₂ gas and (b) NH₃ gas. 130

Figure 4.15. The binding structure of H₂ and NH₃ molecule on the bulk-like slab of (a) Pd, (b) Pt, and (c) Au. 131

Figure 4.16. Oxygen adsorption energy on Pt nanocone cluster with variety of coverages. 133

Figure 4.17. Nanocone cluster model of (a) Au and (b) Pt. 133

Figure 4.18. Comparison of calculated binding energy from bulk-like Pd slab, Au, Pt nanocone cluster and experimental response value for (a) H₂ gas and (b) NH₃ gas. 135

Figure 4.19. Clustering Energy of Au and Pt at the edge site of MoS₂. For the structure of clustered metal atoms in inset, each Mo, S, Au, and Pt atoms have the purple, yellow, orange, and grey color. 138

Chapter 1.

Necessity to Understand the Reaction Mechanism of the Catalysis

1.1. Background of the Research

Nowadays, theoretical approaches toward various catalytic reactions have been performed. Among various simulation methodologies, density functional theory based first-principles calculations are intensely utilized to imitate the intrinsic properties of various materials on an atomic scale. As the catalytic reaction itself occurs at the surface of the catalyst material, most simulation works to understand the reaction mechanism concentrate on imitating the surface chemistry of the real reaction environment.

Though the interpretation of the reaction mechanism itself can be somehow scientifically meaningful, from the viewpoint of engineering, the ultimate goal of simulation works is the high-throughput screening of various catalyst material candidates. As the range of materials applied as a catalyst increases, exploring the optimal catalyst by comparing experimental results has become a very time-consuming process and is no longer an effective screening method. Furthermore, due to the variations in electrochemical measurement settings or the quality of samples, it is difficult to compare the performance of various catalyst materials from different studies. However, through the high-throughput screening, the catalytic performance can be compared under the fixed external variables.

For the high-throughput screening of the catalyst materials, it is essential to find the descriptor, which can represent the catalytic property of the material. In addition, descriptors should be obtained with the moderate calculation

resource. With the effectiveness of the descriptor, there have been intensive attempts to find out the universal descriptors for various catalytic reactions. Among those approaches, studies of the Noroskov group on the descriptor for water splitting reaction are regarded as the most universal and popular outputs.^[1-3] As a representative example, the Noroskov group presented the study of the relation between the exchange current for hydrogen evolution reaction and hydrogen adsorption energy in 2005.^[4] Based on the simple reaction steps composed of the adsorption and desorption of hydrogen atoms, the adsorption energy of the hydrogen determines the reaction barrier of the hydrogen evolution. This correlation can be plotted as the famous volcano curve, which indicates the materials with the optimal catalytic property.

To find out the descriptor of the catalytic reaction, the comprehension of the reaction mechanism should be preceded, just as the process of finding hydrogen evolution reaction descriptor. As understanding of the reaction mechanism cannot be solely conducted by experiment or simulation, mutual verification is essential. By comparing the trends of experimental and simulation results, the catalytic reaction steps can be defined in atomistic scale, which becomes the milestone for descriptor investigation as can be seen in Figure 1.1.

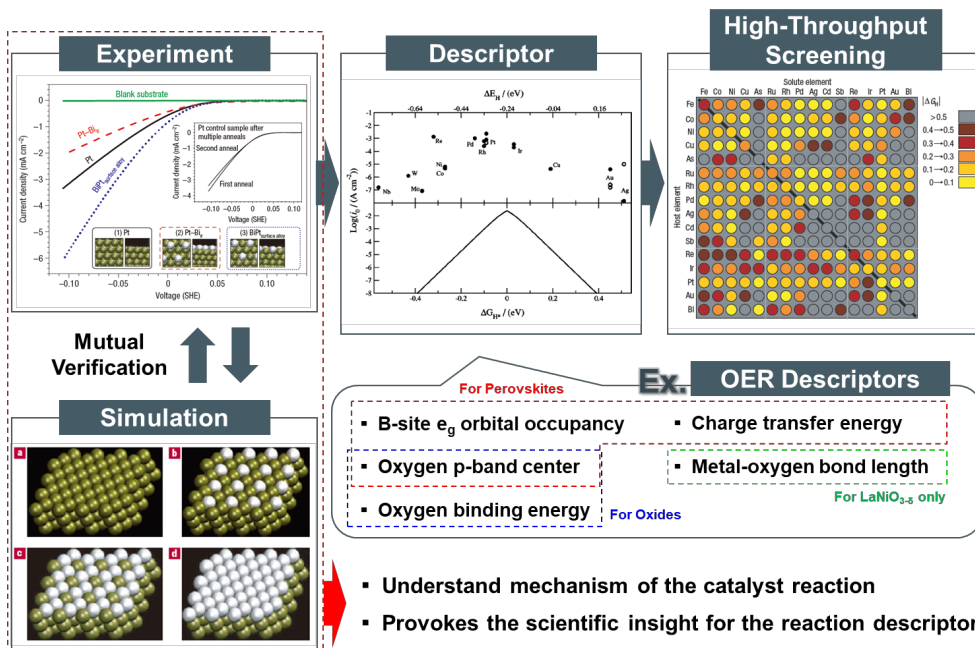


Figure 1.1. The process toward high-throughput screening and examples of descriptors for water splitting

1.2. Objective of the Thesis

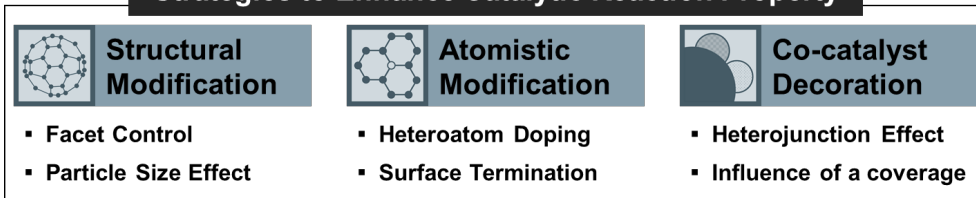
As mentioned above, numerous attempts to understand the mechanism of catalytic reactions for various materials have been performed. Though, in recent days, most approaches to enhance the catalytic performance are not conducted with a single material. For the better reactivity of the catalyst materials, various elaborate modification strategies have been applied. Modification strategies can be categorized as structural modification, atomistic modification, and co-catalyst decoration.

The structural modification can be represented as the morphology control of the catalyst materials. By controlling the morphology, the surface area of the catalyst material can be maximized or the highly reactive facet dominant catalyst structure can be acquired. The atomistic modification is mainly focused on generating the reactive site at the surface of the catalyst by modifying the physical and electronic structure. The heteroatom doping is the most common way to modify the electronic structure of the material. With the introduction of the element possessing different intrinsic properties, the local environment, such as the bond length or charge density, changes, and this leads to the variation in the reaction mechanism. Also, the elemental termination of the material is critical to the surface chemistry of catalytic reaction. The surface termination can be affected by conditions during the synthesis, or even after the synthesis. Terminated atoms or molecules are directly involved in the reaction mechanism. Finally, the

application of a co-catalyst can generate the synergetic effect by forming the heterojunction. With the combination of appropriate band alignment, the built-in potential in direction of favorable carrier transfer can be constructed. With the types of co-catalyst, the optimal coverage also has to be determined.

Despite various catalyst modification strategies are applied in experimental studies, theoretical approaches on the influence of modification on reaction mechanisms are relatively less intensive. Therefore, in this manuscript, the effect of modification methodologies will be expressed in simulation results and will be verified through the comparison with experimental results. As shown in Figure 1.2, the application to water splitting, CO₂ reduction, and gas sensors will be covered in the following chapters.

Strategies to Enhance Catalytic Reaction Property



Understand the Contribution Through Surface Chemistry

Application on Various Catalytic Reactions

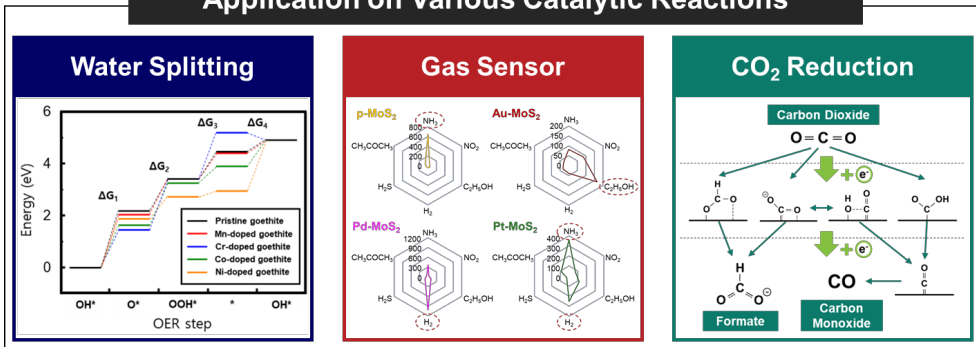


Figure 1.2. Overall flow of the dissertation

1.3. References

- [1] J. K. Norskov, J. Rossmeisl, A. Logadottir, L. Lindqvist, Origin of the Overpotential for Oxygen Reduction at a Fuel-Cell Cathode. *J. Phys. Chem. B*, **2004**, 108, 17886-17892
- [2] J. Rossmeisl, Z.-W. Qu, H. Zhu, G.-J. Kroes, J. K. Norskov, Electrolysis of water on oxide surfaces, *J. Electroanal. Chem.* **2007**, 607, 83-89
- [3] M. Garcia-Mota, A. Vojvodic, H. Metiu, I. C. Man, H.-Y. Su, J. Rossmeisl, J. K. Norskov, Tailoring the Activity for Oxygen Evolution Electrocatalysis on Rutile TiO₂(110) by Transition-Metal Substitution. *ChemCatChem*. **2011**, 3, 1607-1611
- [4] J. K. Norskov, T. Bligaard, A. Logadottir, J. R. Kitchin, J. G. Chen, S. Pandelov, U. Stimming, Trends in the Exchange Current for Hydrogen Evolution. *J. Electrochem. Soc.* **2005**, 152, J23-J26

Chapter 2.

Understanding the Enhancement of the Catalytic Properties of Goethite by Transition Metal Doping: Critical Role of O* Formation Energy Relative to OH* and OOH*

2.1. Introduction

Electrochemical water splitting has attracted intensive attention in recent years as a sustainable hydrogen generation method that can be an alternative to fossil fuels.^[1,2] The water-splitting reaction is divided into hydrogen evolution reaction (HER) and oxygen evolution reaction (OER). While HER catalysts reached the overpotential (η) less than 100 mV at 10 mA/cm², the overpotential of the most active OER catalysts is still near 200 meV.^[3-5] The complicated 4 electron pathway attributes to the sluggish kinetics of the OER, which makes the OER the bottleneck of the water-splitting reaction. For the OER catalyst, Ru and Ir-based oxides are known to be the most superior electrocatalysts. However, due to their scarcity and high cost, their utilization as water splitting catalysts is severely limited. Therefore, there have been extensive efforts to investigate cost-effective and durable OER catalysts.

With their terrestrial abundance and long-term stability, first-row transition metal oxides have attracted huge interest from many researchers.^[6-8] Among various transition metals, nickel or cobalt-based oxides have shown superior catalytic properties.^[9] On the other hand, iron that is extremely cost-effective when compared to cobalt or nickel has not caught the attention of researchers. Because of the high recombination rate and inert surface activity, iron-based oxides are regarded as inferior OER catalysts. Despite the above disadvantages, taking into account the abundant resources of

ferrite in Earth, Fe-based OER catalysts are most suitable for large-scale water electrolysis. Recently, there have been various attempts to overcome the inferior catalytic properties of the Fe-based oxides. Not only hematite or magnetite, which are the most commonly known Fe-based oxides, hydroxides and oxyhydroxides of the Fe are receiving interests from researchers.^[10-12]

Adopting the multi-metal system by doping or alloying are the most representative methods used to improve the catalytic properties of materials.^[13-15] By introducing extra elements into the material, the electronic structure of the material can be controlled to be beneficial for the catalytic reaction, and the surface-active site with better reactivity can be generated. Based on the transition metals, a large diversity of multi-metal combinations and compositions has been exploited. Among various multi-metal OER catalysts, Co- or Ni-based (oxy)hydroxides with the addition of Fe are reported to have the highest activity in the alkaline electrolyte. The incorporation of the Fe in Co- or Ni-based (oxy)hydroxide enhances the intrinsic properties such as electrical conductivity by changing the electronic structure.^[16,17] Furthermore, the incorporated Fe itself acts as an active site, which is more thermodynamically preferable for the OER.^[18-20] In spite of numerous studies about doping in the transition metal-based oxides, they are still mostly concentrated on the Ni-based multi-metal catalyst. Several studies have proposed iron oxyhydroxides with doping as an OER catalyst, but they mainly concentrated on only catalytic properties, not on their

mechanism.^[21,22] In addition, the criteria for selecting the appropriate dopant for oxides are unclear. There have been many descriptors for the OER catalysts such as eg orbital occupancy,^[23] metal-oxygen bond length,^[24] oxygen p-band center,^[25-27] and charge transfer energy.^[28,29] These descriptors are mainly based on the bulk state of perovskites. Therefore, an atomistic investigation for surface reaction based on the oxide system is required.

In this study, we investigated the effect of doping at the surface of goethite and suggested the systematic methodology to predict the enhancement of catalytic property for the different doped goethites based on both first-principles calculations and experimental verification. In the calculation, the surface that mainly contributes to the OER of goethite is predicted. Transition metal dopants (TM = Cr, Mn, Co, and Ni) are substituted with the surface iron atom, and OER mechanism on the TM-doped goethite is investigated. For the study, the active site and potential determining step (PDS) are identified. A scaling relation determined from the change in Gibbs free energy shows that the relative energy level of the adsorbed oxygen is critical to the overall overpotential of the OER of goethite. We further find out that the stability of the adsorbed oxygen is determined by the bond strength between the surface active site metal and the adsorbed oxygen and is proportional to the occupied p-band center of the adsorbed oxygen. To verify our findings, pristine and TM-doped goethites are synthesized by the electrodeposition. From the measured overpotential of

the pristine and TM-doped goethites, we have confirmed that the effect of doping on the catalytic activity matches well with our calculation results. We believe that our work does not only provide a way to enhance the Fe-based catalysts but also shows an effective way to design the water-splitting catalyst by doping.

2.2. Theoretical Approach

2.2.1 Computational Details

All DFT calculations were performed with the Vienna ab initio simulation package (VASP)^[30,31] based on spin-polarized density functional theory (DFT).^[32,33] To replace the core electrons to pseudopotentials, the projector-augmented wave (PAW)^[34,35] method is implemented. The exchange-correlation energy was described by the generalized gradient approximation (GGA) using the Perdew-Burke-Ernzerhof (PBE) functional.^[36] For the better description of the on-site Coulomb interaction of the transition metal d-electrons, the GGA+U method based on the Dudarev's approach was adopted. The effective Hubbard U parameter (U_{eff}) for Fe in the goethite was set to be 5.0 eV. It was demonstrated that the value of $U_{\text{eff}} = 5$ eV provides the reasonable geometric, electronic structure of the goethite, including the lattice parameter and bandgap. We calculated the band gap of goethite with various U_{eff} values from 3 eV to 5 eV. As seen in Figure 2.1, with the increase of U_{eff} value, bandgap increases either. Considering that the experimental bandgap of goethite ranges from 2.1 ~ 2.5 eV, it is reasonable to use the U_{eff} value of 5 eV.^[37-39] Furthermore, the electron transfer and surface adsorption behaviors, which will be mainly dealt with in this study, are also well described by the value.^[40-43] For dopant elements such as Mn, Cr, Co and Ni, U_{eff} values obtained from the work of Jain et al., which are fitted from the oxide formation energy, are chosen.^[44] The values

of U_{eff} for dopants are specified in Table 2.1. The kinetic cutoff for the plane-wave basis was 400 eV throughout all calculations in this study. For the electronic self-consistency and force tolerance, criteria of 10^{-5} eV and 0.01 eV/Å are implemented.

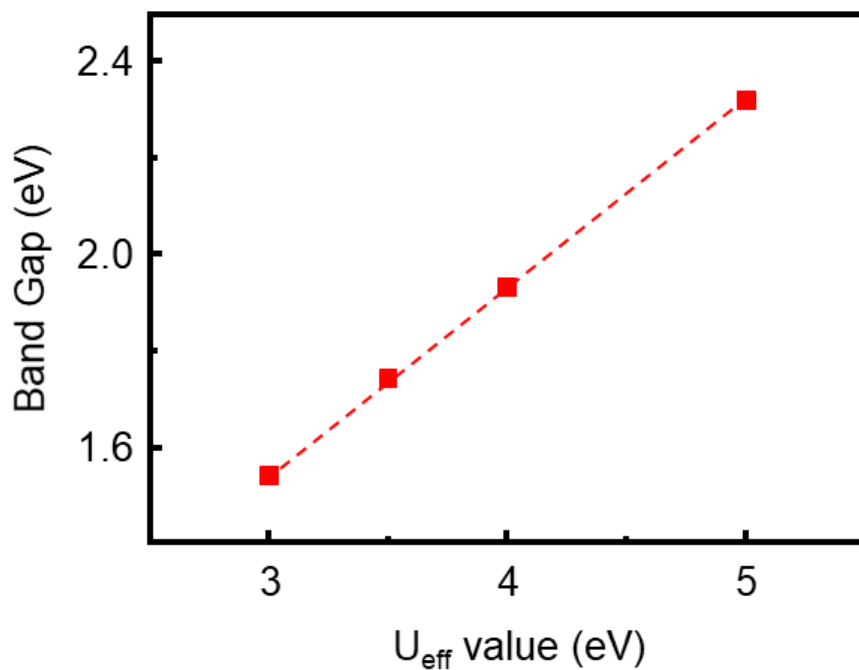


Figure 2.1. The bandgap of the goethite with various U_{eff} values

	Cr	Mn	Co	Ni
U value	3.5	3.9	3.4	6.0

Table 2.1. U_{eff} values for the dopants in goethite based on the oxide formation energy from study of Jain et al.^[44]

2.2.2 Bulk Properties of the Goethite

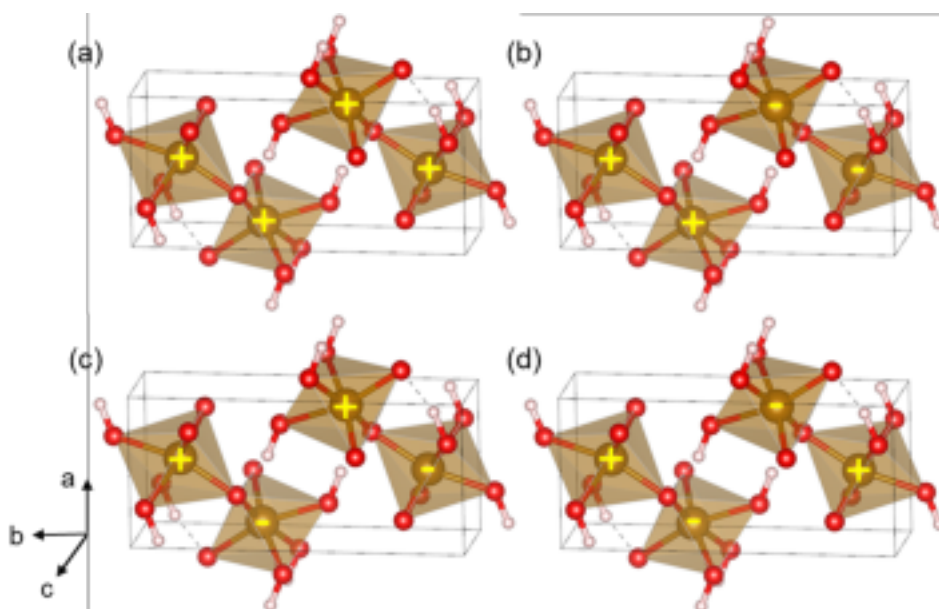


Figure 2.2. The unit cell of orthorhombic structure goethite. The spin state of each iron atom is represented on the atom. Iron atoms with + mark have the up-spin while those with – mark have down-spin. (a) Ferromagnetic configuration and (b)-(d) 3 antiferromagnetic configurations are presented

Before constructing the slab model for the surface reaction of goethite, the bulk structure of goethite is fully relaxed to reach the ground state. For the bulk goethite relaxation, we used the k-point grid of $3 \times 9 \times 5$ in the Monkhorst-Pack scheme. To find out the most stable magnetic configuration of goethite, various configurations of Fe atom magnetic moments are investigated. From the unit cell of goethite, composed of 4 iron atoms, 8 oxygen atoms, and 4 hydrogen atoms, 4 different magnetic configurations can be considered, which can be seen in Figure 2.2. The spin-polarized DFT energies are calculated and compared for 4 different configurations. Among the 3 different antiferromagnetic configurations, the

configuration of Figure 2.2(c) has the lowest energy of -97.323 eV while the ferromagnetic configuration has the value of -96.756 eV as presented in Table 2.2. This result fits well with the former study on theoretical and experimental studies of the goethite.^[45,46] Therefore, for further calculations in this study, the antiferromagnetic configuration of Figure 2.2(c) is applied. Lattice parameter values of the antiferromagnetic configuration goethite are also checked, as shown in Table 2.3. Lattice parameters coincide well with the experimental lattice parameters, which has an error of ~1%.^[47] Fe atoms in the bulk goethite have the oxidation state of 3+ with the octahedral coordination. Fe³⁺ has the 5 d-electrons and prefers to be in the high spin state with the magnetic moment of ~4.3 μ_B .

	Antiferromagnetic			Ferromagnetic
	2.2(b)	2.2(c)	2.2(d)	2.2(a)
Energy per unit cell (eV/cell)	-97.184	-97.234	-96.66	-96.756

Table 2.2. Gibbs free energy of the fully relaxed goethite unit cell with antiferromagnetic and ferromagnetic configuration.

	Calculation (Å)	Experimental (Å)	Error
a	4.538	4.602	1.3 %
b	9.896	9.952	0.5 %
c	2.998	3.021	0.7 %

Table 2.3. The lattice parameter of fully relaxed unit cell of goethite obtained from the DFT calculation and experiment values from reference^[47]

2.2.3 Surface Modeling

All surface slabs are constructed to have 6 layers of Fe atoms with a minimal thickness of 11 Å. The vacuum layer of 15 Å is inserted to avoid the interaction between edges of the surface. Surfaces at each side of the slabs are controlled to be symmetric to the center of the slab. The center 2 layers of slabs are fixed to mimic the state of the inner bulk region, and 4 layers at each side of the slab are relaxed. To alleviate the computational load, sparse k-point meshes of 3×5×1 for (001), (111) surfaces and 5×3×1 for (021) surface are used. A dipole moment correction was used to correct the residual dipole moments perpendicular to the slab surface.^[48]

To determine the surface termination of the slab, the chemical potential (μ_i) of the adsorbed species are defined. The chemical potential of the adsorbed species, which mainly exist in the aqueous solution, is presented.

$$\begin{aligned}\mu_{\text{O}} &= [\text{G}(\text{H}_2\text{O}) - \text{G}(\text{H}_2)] - 2\Delta\text{G}_{\text{H}^+}(\text{pH}) \\ \mu_{\text{OH}} &= \left[\text{G}(\text{H}_2\text{O}) - \frac{1}{2}\text{G}(\text{H}_2) \right] - \Delta\text{G}_{\text{H}^+}(\text{pH}) \\ \mu_{\text{H}_2\text{O}} &= \text{G}(\text{H}_2\text{O}) \\ \mu_{\text{H}} &= \frac{\text{G}(\text{H}_2)}{2} + \Delta\text{G}_{\text{H}^+}(\text{pH})\end{aligned}$$

Except for the bare surface termination, it is assumed that all the metal dangling bonds at the surface are fully terminated with the adsorbates. For the pH term, pH=14 is used for all chemical potentials. To calculate the surface energy, the method of Reuter and Scheffler is applied, which gives the following expression:^[49]

$$\gamma = \frac{1}{2A} \left[G_{\text{slab}} - N_{\text{Fe}} g_{\text{bulk}} - \sum_i (N_i - x_i N_{\text{Fe}}) \mu_i \right]$$

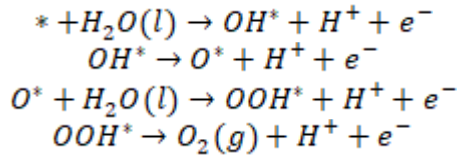
where A is the area of the single side slab surface. The subscript i stands for adsorbed atoms/molecules at the goethite surface. G_{slab} is the free energy of the slab and N_i is the number of atoms of terminated species in the slab cell. g_{bulk} is the free energy of the bulk unit cell of goethite and x_i is the number of atoms per bulk unit cell. The subtraction of the first and second term gives the surface energy of the stoichiometric slab. For the slab with the nonstoichiometric slab, the chemical potential of the extra atom/molecules is subtracted by the third term.

2.2.4 Thermodynamics of OER

The water oxidation reaction can be written as below.

$$\mu_{\text{O}} = [\text{G}(\text{H}_2\text{O}) - \text{G}(\text{H}_2)] - 2\Delta\text{G}_{\text{H}^+}(\text{pH})$$

If the reaction proceeds ideally, the reaction requires the thermodynamic potential of 1.23 V under the standard conditions of $T = 298.15$ K, $P = 1$ bar and $\text{pH} = 0$. However, the complicated multi-electron reaction leads to the sluggish reaction rate of the OER, which generates the overpotential of the OER. To calculate the overpotential of the OER, the elementary proton-coupled electron transfer (PCET) steps based on the study of Rossmeisl and Norskov is considered.



The * represents the active site without any adsorbed species and OH^* , O^* , OOH^* represent the hydroxide, oxygen and oxyhydroxide adsorbed on the active site of the slab, respectively. The reaction at the active site proceeds in the sequence of intermediates *, OH^* , O^* and OOH^* . Because, in our goethite slab models, active site metal atom is initially adsorbed with OH, the reaction starts from the OH^* reaction intermediate. The Gibbs free energy difference of step 1-4 (ΔG_{1-4}) can be calculated with the following equations:

$$\begin{aligned} \Delta\text{G}_1 &= \Delta\text{G}_{\text{O}^*} - \Delta\text{G}_{\text{OH}^*} - eU + \Delta\text{G}_{\text{H}^+}(\text{pH}) \\ \Delta\text{G}_2 &= \Delta\text{G}_{\text{OOH}^*} - \Delta\text{G}_{\text{O}^*} - eU + \Delta\text{G}_{\text{H}^+}(\text{pH}) \\ \Delta\text{G}_3 &= 4.92 - \Delta\text{G}_{\text{OOH}^*} - eU + \Delta\text{G}_{\text{H}^+}(\text{pH}) \\ \Delta\text{G}_4 &= \Delta\text{G}_{\text{OH}^*} - eU + \Delta\text{G}_{\text{H}^+}(\text{pH}) \end{aligned}$$

In equations, U is the electrode potential respect to the normal hydrogen electrode (NHE) at the standard condition. For the non-zero pH condition, the Gibbs free energy change of a proton is expressed as

$\Delta G_{H^+}(\text{pH}) = -k_B T \ln(10) \times \text{pH}$ according to the Nernst equation. To avoid calculating the O₂ bond energy, which is difficult to obtain accurately with GGA-DFT, the sum of ΔG_{1-4} is fixed to the formation energy of two water molecules ($1.23 \times 4 = 4.92$ eV). The Gibbs free energy change (ΔG_i) in equations is expressed as $\Delta G_i = \Delta E_i - T\Delta S + \Delta ZPE$. ΔE_i , ΔZPE , and $T\Delta S$ denote the adsorption energy of the intermediate species on the active site, the zero-point energy, and the entropy correction, respectively. The ZPE is calculated only for the adsorbed species and reactant molecules. For the entropy correction, liquid water molecule and gas hydrogen molecule, which mainly contribute to the total energy, are considered. The formation energy, ZPE, and entropy correction values are presented in Table 2.4. The adsorption energy of the adsorbed intermediates is calculated with the equations below:

$$\begin{aligned}
 \Delta E_{OH^*} &= E_{OH^*} - E_* + \frac{1}{2}E(H_2) \\
 \Delta E_{O^*} &= E_{O^*} - E_* + [E(H_2O) - E(H_2)] \\
 \Delta E_{OOH^*} &= E_{OOH^*} - E_* + \left[2E(H_2O) - \frac{3}{2}E(H_2)\right]
 \end{aligned}$$

E_{OH^*} , E_{O^*} , E_{OOH^*} , E_* represent the total energy of slabs in intermediate states calculated by DFT. Using the standard hydrogen electrode (SHE), the state of proton and electron is in equilibrium with half of the hydrogen molecule under zero potential. As can be seen in equations of Gibbs free energy difference, because the potential and pH correction terms change the Gibbs free energy in the same amount for all steps, the potential determining step (PDS) is not affected by the pH or potential. Thus the step with the largest

Gibbs free energy difference among 4 steps becomes the theoretical potential determining step and the overpotential is expressed as below.

$$\eta = \frac{\max[\Delta G_1, \Delta G_2, \Delta G_3, \Delta G_4]}{e} - 1.23 \text{ V}$$

	H ₂ O	H ₂	O*	IH*	OOH*
E^{DFT} (eV)	-14.026	-6.759	-	-	-
ZPE (eV)	0.57	0.35	0.15	0.431	0.614
TAS (eV)	0.67	0.403	-	-	-

Table 2.4. DFT total energy, zero-point energy and entropic contribution of H₂O, H₂ molecules and reaction intermediates. Entropic contribution are values under the standard conditions which are T=298K, P=1 bar.

2.3. Experimental Section

2.3.1 Film Preparation

Pristine goethite and TM-doped goethite were deposited onto the Fluorine-doped Tin Oxide (FTO) glass by the electrodeposition. Because other studies that synthesize the goethite for water electrolysis mostly selected the FTO as substrate, to compare the catalytic property with our result, we chose the FTO as the electrodeposition substrate.^[41,50] For the goethite electrodeposition, aqueous solution of 0.01 M ammonium iron sulfate hexahydrate (Fe(NH₄)₂(SO₄)₂•6H₂O, DAEJUNG) and 0.04 M potassium

acetate (CH_3COOK , DAEJUNG) were used and for TM-doped goethite, sulfates of dopant elements (0.002 M MnSO_4 , 0.0005 M CoSO_4 , 0.001 M NiSO_4 , DAEJUNG) are added. The concentration of the dopant precursors is determined to maintain the percentage of dopant element in the range of 2~4 %. Before preparing precursor solutions, deionized water is purged with nitrogen gas for 30 minutes in the beaker covered with the parafilm, which suppresses the formation of insoluble iron(III) hydroxide. Precipitation of iron hydroxide interferes with the electrodeposition of pure phase goethite because it consistently lowers the pH condition of the solution.^[51] Therefore, purging is maintained during the electrodeposition. Temperature is fixed with 60°C, which is an appropriate condition to achieve a goethite phase among various iron oxyhydroxide phases.^[52,53] In the case of pH, as mentioned above, the precipitation of iron(III) (oxy)hydroxides consistently lowers the pH of the solution during the electrodeposition. It is possible to slow down the change of pH with nitrogen purging, but as time goes on, the pH value becomes far from the initial value of 6.5. To prevent severe pH change, the precursor solution is titrated during the electrodeposition with the 1 M sodium hydroxide solution (DAEJUNG), which maintains the pH value in the range of 6.0 ~ 6.5.

For the electrodeposition, the standard three-electrode cell was used with Pt-plate counter electrode and Ag/AgCl (3 M KCl) reference electrode. FTO for the cathode is sonicated in acetone, isopropyl alcohol and deionized water for the cleaning. Then it is covered with ketone tape to make

deposition area of 1 cm². The deposition was carried out at the voltage of -0.2 V vs Ag/AgCl (3 M KCl), as mentioned in other references,^[52,53] which gave the current density of 300~400 μA/cm². For TM dopant-doped goethites, similar current density ranges of 300~400 μA/cm² were observed. After electrodeposition, 1 cm² of the deposited area is rinsed with deionized water and ketone tapes are removed.

2.3.2 Characterization

With x-ray diffraction (XRD, D8-Advance) analysis, crystal structures of the synthesized goethite and doped-goethite are investigated (Cu Kα1 X-ray, incident angle of 0.02 step size). Scanning electron microscope (SEM) images and Energy Dispersive Spectrometer (EDS) result of the elements' proportion are acquired from MERLIN Compact (FE-SEM, JEISS) operating at 20 kV.

2.3.3 Electrochemical Measurement

Electrochemical measurements in this paper were performed with the three-electrode system, Ag/AgCl (saturated) as a reference electrode and Pt plate as a counter electrode. All measurements were done in the 1M sodium hydroxide electrolyte using the potentiostat (Ivium Technologies, Nstat). Cyclic voltammetry scans were done at the scan rate of 10 mV/s, toward the anodic direction. The measured potential versus the Ag/AgCl reference electrode was converted to the reversible hydrogen electrode (RHE) scale through the Nernst equation.

$$E_{RHE} = E_{Ag/AgCl} + 0.059 \times pH + E_{Ag/AgCl}^{\circ}$$

E_{RHE} is the converted potential versus RHE, $E_{Ag/AgCl}^{\circ}$ has the value of 0.198

at 25 °C, and $E_{\text{Ag}/\text{AgCl}}$ is the potential measured experimentally versus the Ag/AgCl reference electrode.

2.4. Result and Discussion

2.4.1 Surface Determination

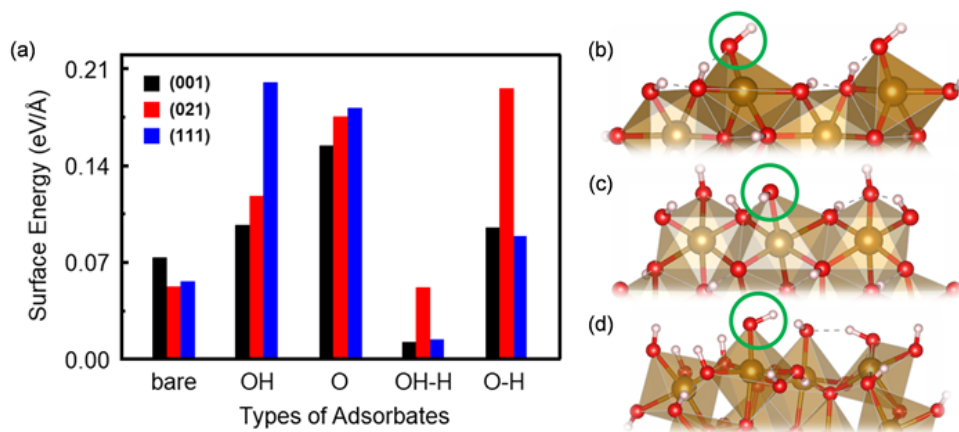


Figure 2.3. (a) Surface energy of (001), (021), (111) surfaces with various terminations. Atomic structures of (b) (001) surface, (c) (021) surface, and (d) (111) surface with OH-H surface termination. The adsorption sites for OER intermediates are marked with green circle.

To construct the slab for the OER step calculation, the facet and the surface

termination are determined. Based on the former studies and XRD data, which will be presented in the experimental section, facets of (001), (021) and (111) are selected.^[54-56] On facets, various types of surface terminations that can occur in the aqueous solution are considered. Terminations of O, OH, H₂O are adsorbed on the exposed surface metal atoms, while H is adsorbed on the exposed surface oxygen atoms. The variation in the surface energy of each surface with different terminations are shown in Figure 2.3. For the bare surface without any adsorbed molecules, (021) surface exhibits the lowest surface energy, which fits well with the result reported before.^[54,55] However, when the molecules are adsorbed at the surface of the slab, for all 3 facets, surface termination with OH and H adsorbed termination (OH-H) shows the lowest surface energy. Therefore, in this study, OH and H adsorbed termination is used for the calculation of OER steps. For OH and H adsorbed surfaces, the (001) surface has the lowest surface energy, which means that the (001) surface has the largest portion among various surfaces.

Figure 2.3(b)-(d) shows the surface geometry of the slabs. Our study focuses on the energetics of molecules adsorbed on the outermost Fe atom since it is the most probable site for the catalytic reaction. In Figure 2.3(b)-(d), we can see that the active site Fe atom has different molecular geometries in (001) and (021), (111). In (001) surface, active site Fe atom has the geometry similar to the square pyramidal while (021) and (111) has the geometry of octahedral. To check the oxidation state of the surface active site Fe atom,

magnetic moments are inspected. Each Fe atom of the active site has the magnetic moment of 4.301 μB , 4.347 μB , and 4.321 μB for (001), (021), (111) surface, respectively. From the bulk goethite Fe atom, it is figured out that the high spin Fe^{3+} state with 5 lone pair d-orbital electrons have the magnetic moment of ~ 4.3 μB . Magnetic moments of the Fe in other Fe-based oxides are also checked in Table 2.5, and we can confirm that the magnetic moment is almost constant for the specific number of lone pair d-orbital electrons. The schematic and electron arrangement in the d-orbital of octahedral and square pyramidal configuration is presented in Figure 2.4.

	Oxidation state	# of d-electron	# of lone pair electron	Magnetic moment (μB)
Fe_2O_3	Fe^{3+}	d^1	5	4.39
Fe_3O_4	Fe^{2+}	d^4	6	3.87
	Fe^{3+}	d^5	5	4.31
FeO_2	Fe^{4+}	d^3	4	3.91
CoO	Co^{2+}	d^7	3	2.74
Ni_3O_4	Ni^{2+}	d^8	2	1.65
	Ni^{3+}	d^7	1 (low spin)	1.03
NiO	Ni^{2+}	d^8	2	1.81

Table 2.5. Magnetic moments of various transition metals in different structures obtained from the GGA+U calculation. All the transition metals are in octahedron configuration and U values used in this paper are equally applied.

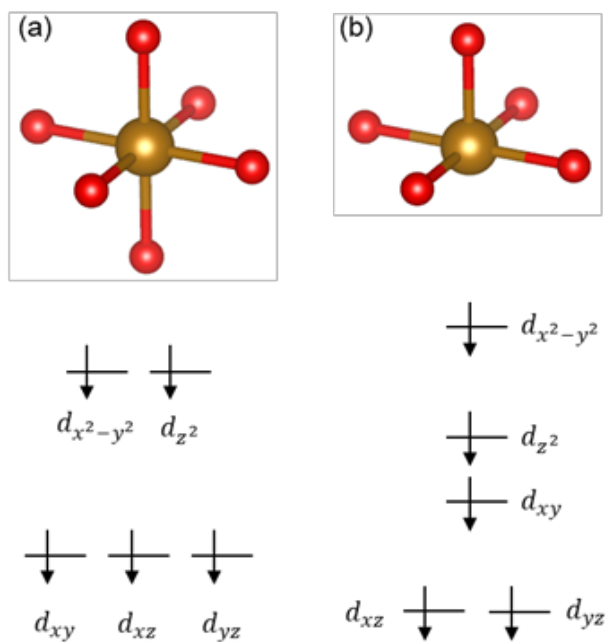


Figure 2.3. Schematic and magnetic configuration of the Fe³⁺ (a) octahedral geometry and (b) square pyramidal geometry.

2.4.2 OER on the Pristine Goethite

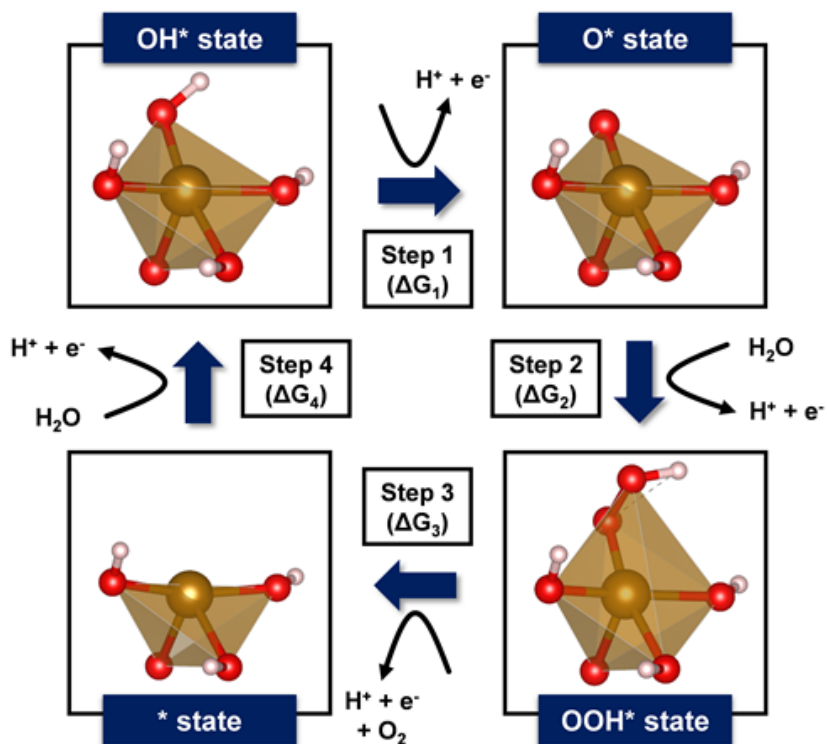


Figure 2.5. Four intermediate states of the 4-step oxygen evolution reaction on the H and OH adsorbed (001) surface of goethite.

To figure out which surface majorly contributes to the water oxidation of goethite, Gibbs free energy differences of OER steps are calculated on the (001), (021), and (111) surface. The zero-point energy (ZPE) and entropic contribution for each reaction steps are presented in Table 2.6. The schematic of OER steps based on the (001) active site is depicted in Figure 2.5. The reaction starts from the OH* and returns to the OH* again through O*, OOH*, *. For each OER intermediate, the magnetic moment of the active site Fe atom is checked to see how redox reaction occurs during the OER. Magnetic moment values and the oxidation state of the active site

metal are presented in Table 2.7. For all surfaces, the active site Fe^{3+} oxidized to Fe^{4+} in step 1 ($\text{OH}^* \rightarrow \text{O}^*$) is reduced back to Fe^{3+} in step 2 ($\text{O}^* \rightarrow \text{OOH}^*$). In step 3 ($\text{OOH}^* \rightarrow *$), only the Fe of (021) stays in Fe^{3+} while that of the other two surfaces reduce to Fe^{2+} and in step 4 ($* \rightarrow *\text{OH}$), the oxidation state of all surface returns to the initial state of Fe^{3+} .

Reaction Step	Reaction	$\Delta\text{ZPE-T}\Delta\text{S}$ (eV)
Step 1	$\text{OH}^* \rightarrow \text{O}^* + 1/2\text{H}_2$	-0.308
Step 2	$\text{H}_2\text{O} + \text{O}^* \rightarrow \text{OOH}^* + 1/2\text{H}_2$	0.538
Step 3	$\text{OOH}^* \rightarrow \text{O}_2 + * + 1/2\text{H}_2$	-0.735
Step 4	$\text{H}_2\text{O} + * \rightarrow \text{OH}^* + 1/2\text{H}_2$	0.505

Table 2.6. The total contribution of zero-point energy and entropic contribution for each OER step.

	OH*	→	O*	→	OOH*	→	*	→	OH*	Overpotential (V)
	μ	ΔG_1 (eV)	μ	ΔG_2 (eV)	μ	ΔG_3 (eV)	μ	ΔG_4 (eV)	μ	
(001)	4.301 (+3)	2.17	3.584 (+4)	1.24	4.267 (+3)	1.06	3.734 (+2)	0.45	4.301 (+3)	0.94
(021)	4.347 (+3)	2.20	3.744 (+4)	1.09	4.335 (+3)	0.08	4.311 (+3)	1.55	4.347 (+3)	0.97
(111)	4.321 (+3)	2.20	3.561 (+4)	1.05	4.301 (+3)	0.77	3.760 (+2)	0.90	4.321 (+3)	0.97

Table 2.7. Magnetic moment values with the oxidation state of active site iron for each interstate and the Gibbs energy difference for 4 steps. The overpotential value is calculated by dividing the highest Gibbs energy difference value with e and subtracting 1.23 V. The Gibbs free energy of the potential determining step is colored with red. The oxidation state of Fe is determined based on the magnetic moment value of various oxidation state Fe in Table 2.5.

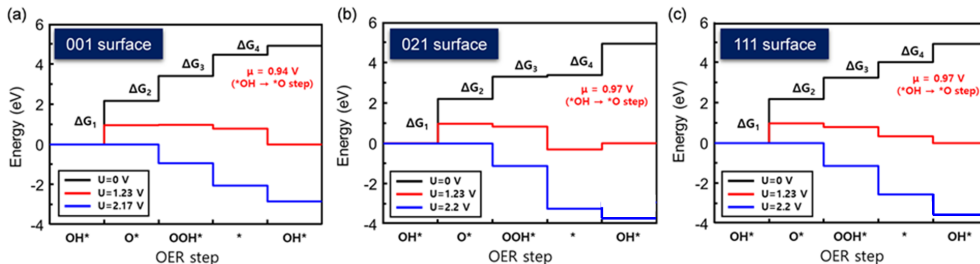


Figure 2.6. Free energy diagrams of the (a) (001), (b) (021), and (c) (111) surface. The free energies of each intermediated state under zero bias, ideal bias of 1.23 V for OER, and minimum bias for OER are denoted with black, red, and blue colors, respectively.

To determine the PDS and the overpotential value, the Gibbs energy difference of OER steps are calculated and represented as a diagram in Figure 2.6. The exact Gibbs free energy value can be seen in Table 2.7. The step with the largest energy difference (ΔG) becomes the PDS and the overpotential can be acquired by subtracting 1.23 V from it as mentioned in the thermodynamics of OER section. For all surfaces, step 1 was the PDS. The overpotential value is lowest in the (001) surface with the value of 0.94 V while (021) and (111) surfaces have the value of 0.97 V. The difference of overpotential between (001) and (021), (111) seems to be derived from the geometry of active site Fe atom.

Therefore, for goethite, it is assumed that the square pyramidal configuration is more suitable for lowering the barrier of reaction. Because the (001) has lower overpotential value, the reaction is easiest to proceed. Considering that (001) surface has the largest portion with the lowest barrier for OER, we discussed the doping on only (001) surface in the following session.

2.4.3 OER on the TM-doped Goethite

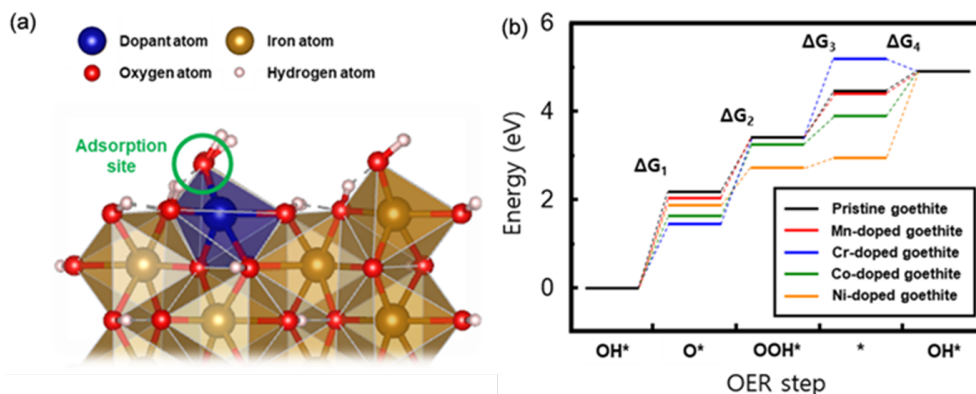


Figure 2.7. (a) Dopant incorporated slab model of (001) goethite surface. (b) Free energy diagram of dopant-doped goethites (001) surface.

To enhance the catalytic property of the goethite, we investigated the overpotential change of the TM-doped goethite. The main purpose of dopant doping in this study is to investigate how the dopant atom directly affects the OER steps. Therefore, only the case that the dopant atom is introduced at the site of the outermost layer Fe is considered. The dopant-introduced (001) surface is illustrated in Figure 2.7(a). When the dopant is introduced, we can think of two different sites for the OER, which are presented in Figure 2.8. To see whether the introduced dopant atom influences the near Fe atom at the outermost layer, OER steps in an adjacent Fe site are also calculated. The OER steps in Mn, Cr, Co-doped goethites are almost identical to those of pristine goethite as can be seen in Table 2.8, which means that the dopant does not affect the OER at adjacent Fe atom site. For Ni-doped goethite, large distortion near the introduced Ni affects the adjacent Fe atom site. The overpotential value is near 0.94 V for Mn, Cr,

Co-doped goethite and even worse in Ni-doped goethite with the value of 1.27 V. Therefore, we could conclude that the enhancement of catalytic property in TM-doped goethite is mainly due to the OER at the dopant atom as an active site.

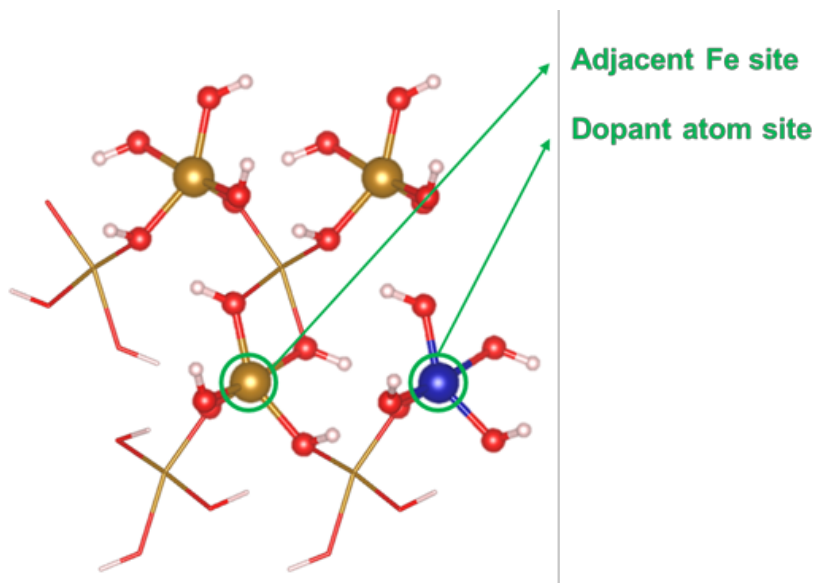


Figure 2.8. The top view of the dopant-doped (001) surface goethite slab. Two different active sites for OER are represented as dopant atom site, adjacent Fe site.

	OH*	→	O*	→	OOH*	→	*	→	OH*	Overpotential (V)
	μ	ΔG ₁ (eV)	μ	ΔG ₂ (eV)	μ	ΔG ₃ (eV)	μ	ΔG ₄ (eV)	μ	
Mn	4.301 (+3)	2.16	3.487 (+4)	1.25	4.268 (+3)	1.07	3.735 (+2)	0.44	4.301 (+3)	0.93
Cr	4.301 (+3)	2.17	3.483 (+4)	1.22	4.265 (+3)	1.07	3.734 (+2)	0.44	4.301 (+3)	0.94
Co	4.301 (+3)	2.17	3.497 (+4)	1.29	4.267 (+3)	1.07	3.734 (+2)	0.4	4.301 (+3)	0.94
Ni	4.301 (+3)	2.50	4.251 (+3)	0.84	4.283 (+3)	- 0.14	4,198 (+3)	1.73	4.301 (+3)	1.27

Table 2.8. Magnetic moment values with the oxidation state of adjacent Fe atom in dopant doped goethite for each interstate and the Gibbs energy difference for 4 steps.

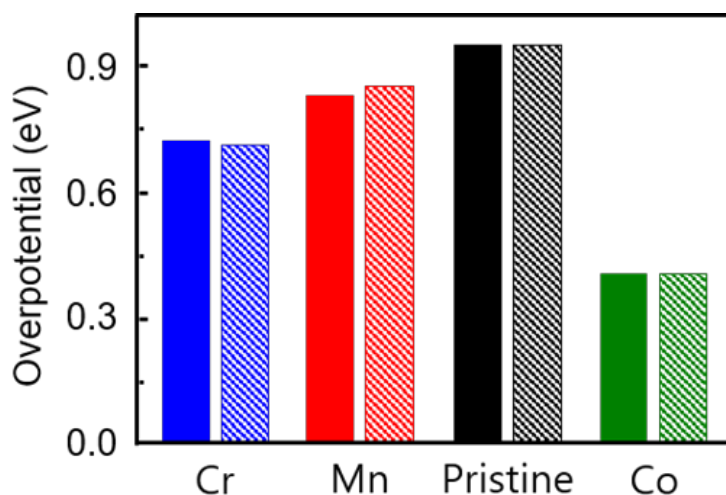


Figure 2.9. Overpotential values of pristine, dopant doped goethites with surface dopant concentration of 25% (colored), and 50% (slash line)

The Gibbs free energy of OER steps at dopant metal atoms is represented in Figure 2.7(b). The exact values of the Gibbs free energy difference for each step and oxidation state of the dopant atoms are stated in Table 2.9. For Mn and Co-doped goethites, they have their PDS in step 1, with an overpotential of 0.83 V and 0.41 V, respectively. On the other hand, PDS of Cr-doped goethite is step 2 with the overpotential of 0.72 V. In the case of Ni-doped goethite, OOH* and * are highly stabilized when compared to others, and step 4 becomes the PDS for Ni-doped goethite, with the overpotential of 0.72 V. We also checked whether the surface concentration of the dopant atoms affects the overpotential value. The energy difference of the OER steps was calculated on the slab with 50% of surface dopant concentration which corresponds to the slab with two dopant atoms at the outer most layer. The overpotential values are shown in Figure 2.9.

Regardless of the percentage of surface dopant atoms, overpotential values were almost constant for all different dopants which indicates that the critical point in the catalytic property enhancement is mainly due to the change of OER active site caused by introduced dopant atom. To confirm the accuracy of the GGA+U method in predicting the electronic structure, overpotential of pristine and Co-doped goethite is calculated using HSE06, as seen in Figure 2.10. Though the value changes, they shift equally and does not affect the trend between them.

	OH*	→	O*	→	OOH*	→	*	→	OH*	Overpotential (V)
	μ	ΔG_1 (eV)	μ	ΔG_2 (eV)	μ	ΔG_3 (eV)	μ	ΔG_4 (eV)	μ	
Mn	3.825 (+3)	2.06	3.178 (+4)	1.35	3.907 (+3)	1.00	4.549 (+2)	0.51	3.825 (+3)	0.83
Cr	2.991 (+3)	1.45	2.252 (+4)	1.95	3.033 (+3)	1.80	3.777 (+2)	-0.28	2.991 (+3)	0.72
Co	3.059 (+2)	1.64	2.048 (+3)	1.63	1.969 (3+)	0.63	2.643 (+2)	1.03	3.059 (+2)	0.41
Ni	2.080 (+2)	1.89	0.898 (+3)	0.83	1.766 (+2)	0.24	1.747 (+2)	1.95	2.080 (+2)	0.72

Table 2.9. Magnetic moment values with the oxidation state of introduced dopant atom for each interstate and the Gibbs energy difference for 4 steps.

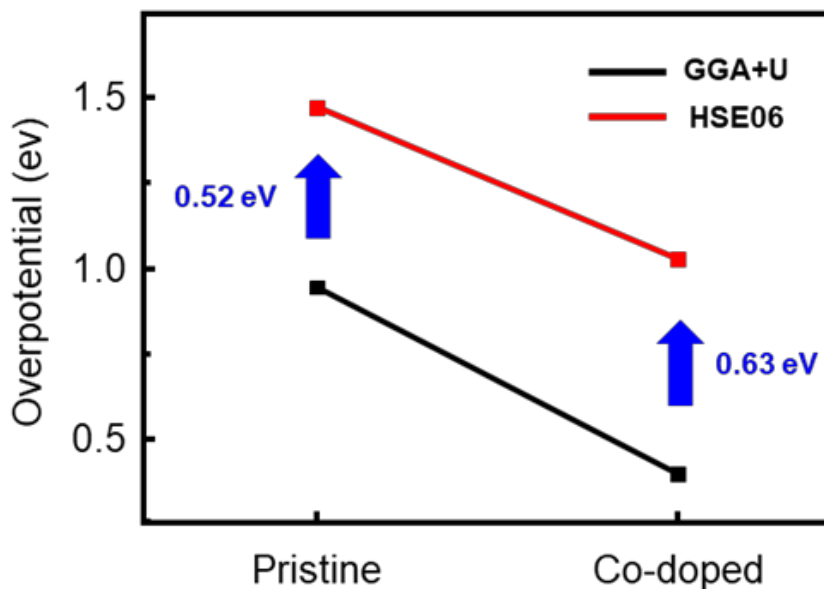


Figure 2.10. Overpotential value of pristine and Co-doped goethite from GGA+U and HSE06 calculation

Except for the Ni, it is possible to find out that the energy difference between the OOH* and OH* is almost constant. This relation can be plotted as scaling relation with the calculated adsorption energy of OOH* and OH*, which can be seen in Figure 2.11(a). Points in Figure 2.11(a) are fitted with the equation of $\Delta G_{\text{OOH}^*} = 0.9207\Delta G_{\text{OH}^*} + 3.42$ in high accuracy. This scaling relation of pure and TM-doped goethites is nearly identical to the universal scaling relation obtained from rutile oxides and perovskites. From the scaling relation, the activity of pristine and TM-doped goethites can be plotted as a volcano curve as shown in Figure 2.11(b). For the OER of catalyst that follows the scaling relation of OH* and OOH*, a PDS mostly occurs in step 1 and step 2 because two steps occupy the Gibbs energy difference of about 3.2 eV out of 4.92 eV.^[18,57-59] As explained in the thermodynamics of OER, the step with the maximum Gibbs free energy difference becomes PDS. Therefore, the PDS of the catalyst is determined by step 1 or step 2 according to the well-known OER descriptor $\Delta G_{\text{O}^*} - \Delta G_{\text{OH}^*}$ value. When the O* intermediate state has the close energy level to one of OH* or OOH*, the Gibbs free energy difference of step 1 or step 2 becomes extremely large, which leads to a large overpotential value. Therefore, for the goethite, the optimal value of the $\Delta G_{\text{O}^*} - \Delta G_{\text{OH}^*}$ is 1.71 eV, which is half of the Gibbs free energy difference of OOH* and OH*.

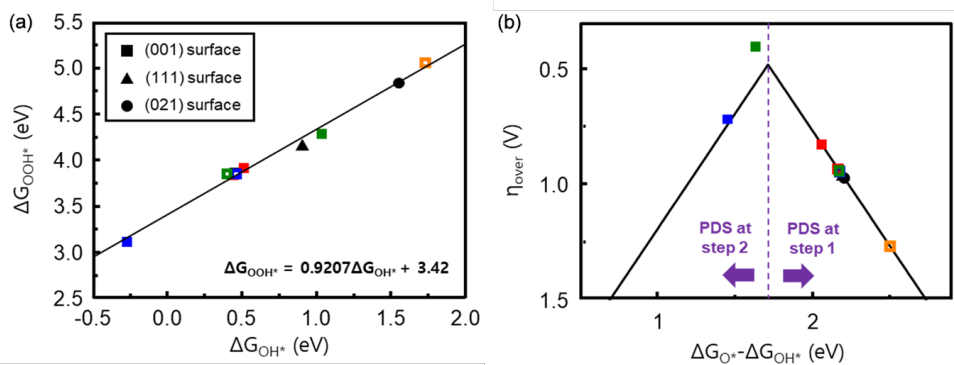


Figure 2.11. (a) Scaling relation between ΔG_{OOH^*} , ΔG_{OH^*} and (b) volcano curve based on the OER of pristine and dopant-doped goethite. The hollow symbols stand for the adjacent Fe site of dopant-doped goethites. The black, red, blue, green, orange colors denote pristine and Mn, Cr, Co, Ni-doped goethite, respectively.

2.4.4 The Correlation between OER Activity and Oxygen p-band center

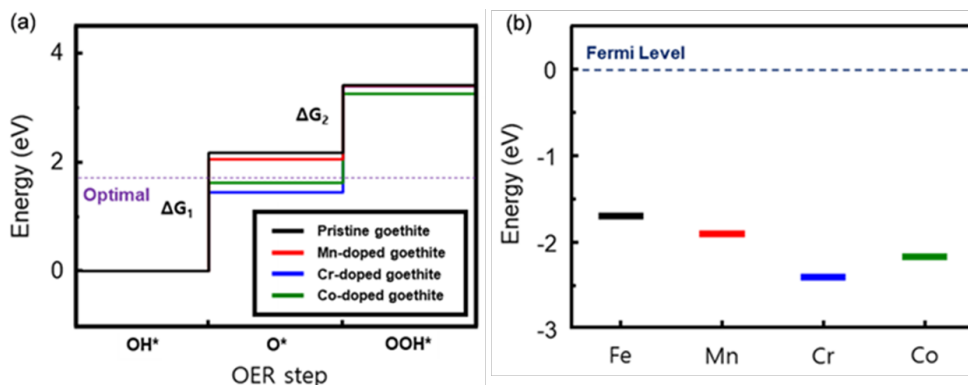


Figure 2.12. (a) Free energy diagram between the OH* state and the OOH* state (b) Oxygen p-band center of the adsorbed oxygen at the active site for pristine goethite and dopant-doped goethites

To explain the overpotential changes in pristine goethite and TM-doped goethite, we concentrated on the formation energy of O*, which directly affects the overpotential value. To make the overpotential value minimum, the relative formation energy of the O* has to be at the middle of OH* and OOH*. The formation energy of O* relative to the OH* is depicted in Figure 2.12(a). In the case of pristine goethite, the O* is placed at a higher energy than the optimal value of 1.71 eV, which leads to the high overpotential value. When the dopants are substituted at the OER active site, we can see that the O* is stabilized. Among the dopants, the Co-doped goethite has the O* closest to the optimal value. Because the stability of the O* is closely related to the bonding between the adsorbed oxygen and active site metal, we investigated the descriptor that can reflect the strength of the metal-oxygen binding, oxygen p-band center.

The oxygen p-band center has been widely used as the descriptor of the catalytic activity. Mainly for the perovskite, some studies reported the relationship with oxygen p-band center and iR-corrected potential, current density value for the OER.^[25,26,60] Hong et al. mentioned that the oxygen p-band center can effectively describe the covalency of the oxygen-metal bonding.^[61] By tuning the covalency of the metal-oxygen bonding, the catalytic property can be enhanced.^[62,63] Though these results well described the relationship of oxygen p-band center and catalytic property, they are mainly based on the electronic structure of the bulk state, which is not applicable to this study. On the other hand, Montoya et al. and Lee et al. investigated the relationship of the occupied oxygen p-band center of the adsorbate at the surface and the adsorption energy.^[64,65] When the center of the occupied oxygen p-band center versus the Fermi level decreases, the adsorption of the oxygen becomes more stable, which means that the metal-oxygen bonding becomes stronger. In Figure 6b, the occupied p-band center of the adsorbed oxygen in O* for various TM-doped goethites are presented. In the pristine and the TM-doped goethite, the oxygen p-band center was at the lower energy level in order of pristine, Mn, Co and Cr. These positions of the occupied oxygen p-band center coincide. Therefore, we concluded that the stability of the O* is related to the binding of oxygen at the active site metal, which can be investigated by the position of adsorbed oxygen p-band center.

2.4.5 Structural and Electrochemical Characterization

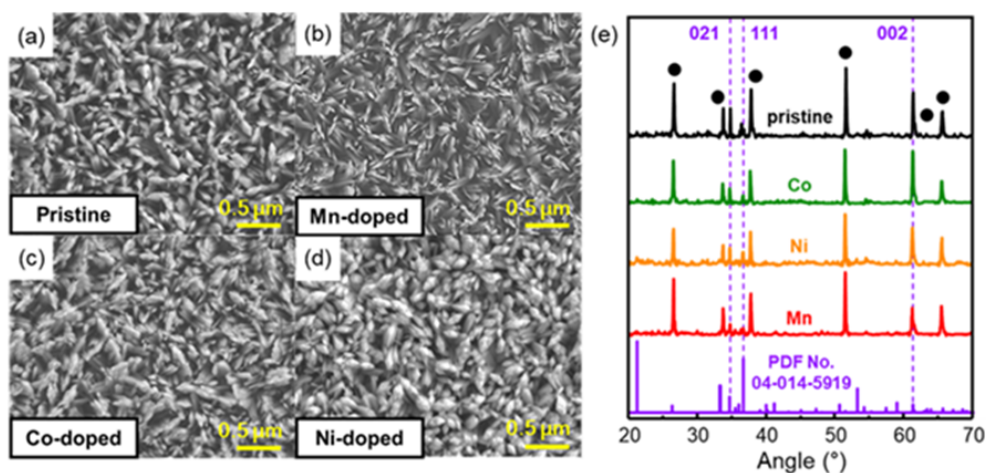


Figure 2.13. SEM image of (a) pristine, (b) Mn-doped, (c) Co-doped, and (d) Ni-doped goethites. (e) XRD data of pristine and dopant doped goethites. FTO reference peaks are marked with a black circle.

We have shown how the dopants can affect the catalytic property of the goethite thermodynamically and suggested the descriptor, occupied p-band center of the adsorbed oxygen. To demonstrate that the theoretical calculation result is consistent with the experimental result, the electrochemical data is collected under well-defined conditions.

In Figure 13(a)-(d), SEM images of the pristine goethite and TM-doped goethites are presented. Only the Cr-doped goethite was not able to be synthesized from the electrodeposition because the deposition potential of Cr was significantly different from other elements. The shape of the pristine goethite is similar to the rhombic-shaped pure goethite which is seen in another reference.^[53] The columnar structure of the synthesized pure goethite is consistent with the preferred crystallographic orientation of (002)

from both calculation and XRD data. The morphology of the TM-doped goethites was nearly the same as the pristine goethite. From the absence of the morphological difference, we could confirm that there was not any phase separation caused by the additional precursor. In addition, with similar morphology, all samples are expected to have comparable surface facets and surface area. Therefore, the difference in catalytic property between various dopants can be mainly dependent on the change of active site. SEM EDS analysis was conducted to confirm that the dopant concentration of each TM-doped goethite is at a similar level. The concentration of each dopant is obtained from 3 different sites and averaged as seen in Table 2.10. Due to the phase separation, which occurs when the dopant concentration reaches about 10%, the concentration of the dopants is maintained at 2–4%.

To investigate the structural properties of the goethite more strictly, XRD analysis was conducted as shown in Figure 2.13(e). Much sharper peaks are achieved from the XRD when compared to other studies, which indicates that goethite in this study is highly crystallized.^[41,50] Three peaks, except the substrate FTO peaks, are observed and they are all indexed with the orthorhombic FeOOH with the space group of Pbnm (PDF No. 04-014-5919). Peaks are indexed as (021), (111) and (002) (equivalent with (001)) as discussed in the surface energy calculation section. When compared to the reference peak intensities, synthesized dopant-doped goethites have relatively higher (002) peak intensity than the other 2 peaks. The increase of the specific surface peak intensity commonly means the preferential growth

of the material.^[66] For pristine and dopant-doped goethites, the strong intensity of (002) peak directly related to the preferential growth of goethites to the direction perpendicular to the c-axis and becomes the evidence of preferential exposure of (001) plane. This result corresponds to the calculation data, the lowest surface energy of (001) surface with OH and H adsorbed termination.

	Mn-doped FeOOH		Co-Doped FeOOH		Ni-doped FeOOH	
	Fe (atom %)	Mn (atom %)	Fe (atom %)	Co (atom %)	Fe (atom %)	Ni (atom %)
1	96.71	3.29	96.59	3.41	97.86	2.14
2	96.4	3.6	96.7	3.3	97.14	2.86
3	95.81	4.19	95.61	4.39	97.46	2.54
Average	96.31	3.69	96.3	3.7	97.48	2.52

Table 2.10. SEM EDS result of Mn, Co, and Ni-doped goethite.

The overpotential value for pristine and TM-doped goethite is measured from the linear sweep voltammograms, represented in Figure 2.14. The overpotential is defined at the current density level of 10 mA/cm². The pristine goethite has the overpotential of 530 mV, which is similar to that of other studies.^[41,50] For the TM-doped goethite, the overpotential decreases in a sequence of Mn (η =510 mV), Ni (η =495 mV), and Co (η =480 mV), which corresponds to the tendency observed in the calculation result. The difference in value is much smaller than expected, which seems to be caused by the low dopant concentration.

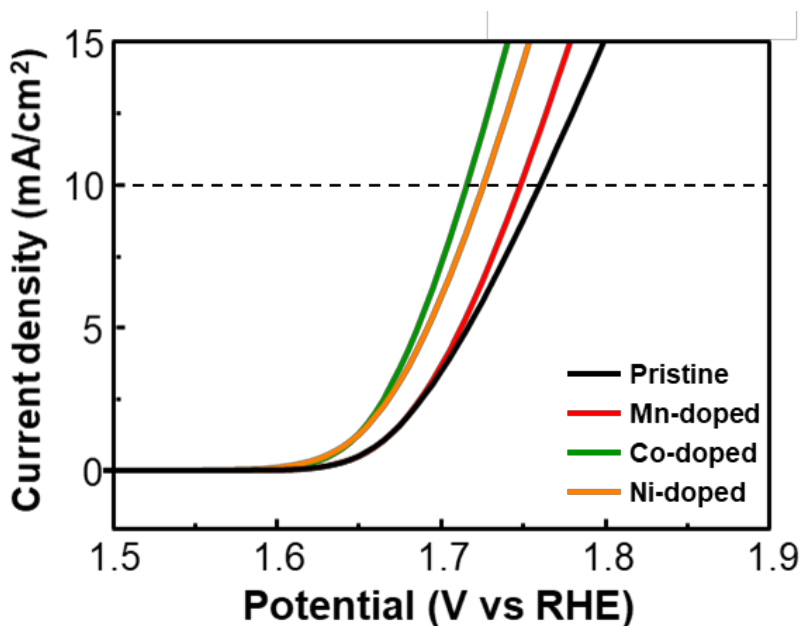


Figure 2.14. Linear Sweep voltammograms of pristine and dopant-doped goethites.

Tafel plots of samples are also investigated to confirm the rate-determining step (RDS) of OER on each sample. Depending on the reaction pathway, each reaction step has its own Tafel slope value. The reaction pathway used in the simulation part is the metal peroxide reaction pathway. The dehydrogenation step and the hydroxide adsorption step correspond to step 1 and step 4 in this study respectively. According to other studies, each step has a Tafel slope value of 30 mV/dec and 120 mV/dec.^[67] In Figure 2.15, the range of pristine, Mn-doped and Co-doped goethite Tafel slope is 40 ~ 43 mV/dec while the Tafel slope of Ni-doped goethite is 109.6 mV/dec. The measured Tafel slope indicates that the RDS of the Ni-doped goethite is different from other goethites and it can be also seen in the PDS of various goethites determined from first-principles calculations. According to the calculation of 4 OER steps, only Ni-doped goethite has the PDS in step 4, while the PDS of others is step 1. Therefore, we could conclude that the PDS determination in simulation can be directly related to the RDS of the experimental result.

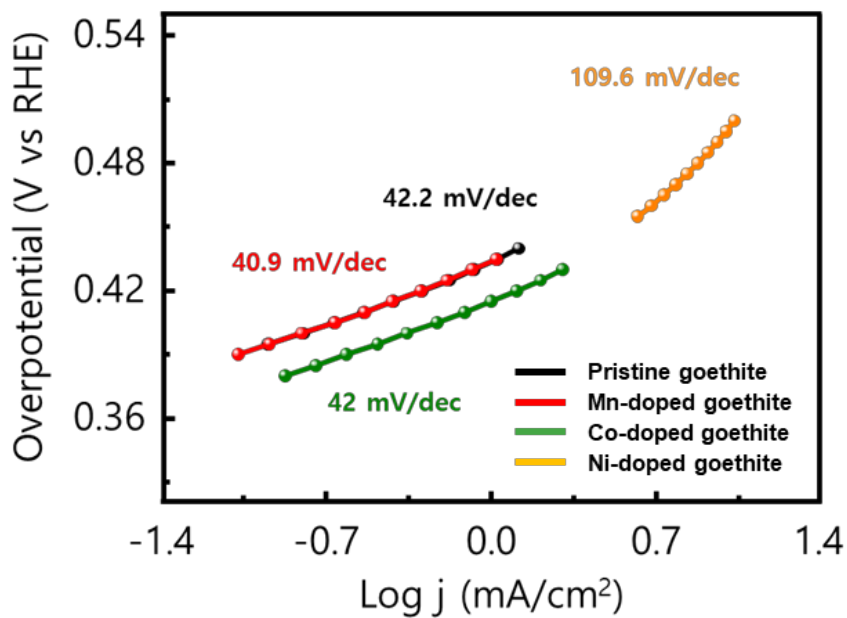


Figure 2.15. Tafel plot of pristine and dopant-doped goethites.

For further analysis of the factors that affect OER properties, the electrochemically active surface area (ECSA) of goethites is measured. Theoretically, the ECSA should be similar between different goethites, because there is no change in morphology and the number of exposed active sites when the dopants are introduced. In Figure 2.16, measured capacitive currents at different scan rates are presented. The cyclic voltammetry (CV) of goethites is achieved in the voltage range of 1.0 V to 1.2 V based on the reversible hydrogen electrode, related to the formation of the electric double layer. CV scan rates are 30 mV/s, 50 mV/s, 100 mV/s, 150 mV/s, and 200 mV/s. The specific capacitance is obtained from the slope of the linear fitting. Assuming that the specific capacitance of the thin film is the typical value of $40 \mu\text{F cm}^{-2}$, ECSA can be calculated as $\text{ECSA} = \text{specific capacitance} (\mu\text{F cm}^{-2}) / 40 \mu\text{F cm}^{-2} \text{ per cm}^{-2}$. Calculated ECSAs for pristine, Mn-doped, Co-doped and Ni-doped goethite were 0.264 cm^2 , 0.222 cm^2 , 0.234 cm^2 , and 0.241 cm^2 , respectively. As can be concluded from similar ECSA value, number of the catalytic active sites is not the major factor in explaining the different catalytic property of goethites.

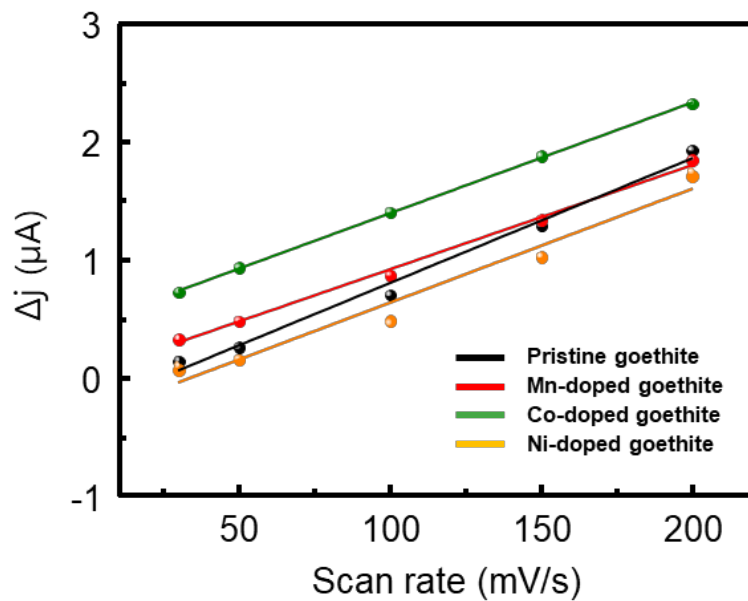


Figure 2.16. Capacitive currents of the pristine and dopant-doped goethites.

The above results indicate that the difference in catalytic property between goethites is caused by the change of active site at the surface of the catalyst and this can be also shown by the electrochemical impedance spectroscopy (EIS) measurement. EIS measurement is carried out at 1.70 V from 105 to 0.5 Hz in 1.0 M NaOH. In Figure 2.17, the Nyquist diagram of the EIS for pristine and dopant-doped goethites is presented. The diameter of the arc in the Nyquist plots represents the charge transfer resistance (R_{ct}) at the interface of catalyst surface and electrolyte. For pristine, Mn-doped, Co-doped, and Ni-doped goethites, we could obtain the R_{ct} values of 10.84 Ω , 8.05 Ω , 4.95 Ω , and 7.20 Ω , respectively. As the high charge transfer resistance interferes with the OER at the catalyst surface, with the decrease of charge transfer resistance, catalytic property enhances. The charge transfer resistance can be regarded as the barrier for OER and first-principles calculations result provides a reasonable explanation for the trend in EIS. The values for the other components in the EIS are almost the same. This indicates that the other electrical properties of different goethites are nearly constant and not a major factor in the trend of catalytic properties.

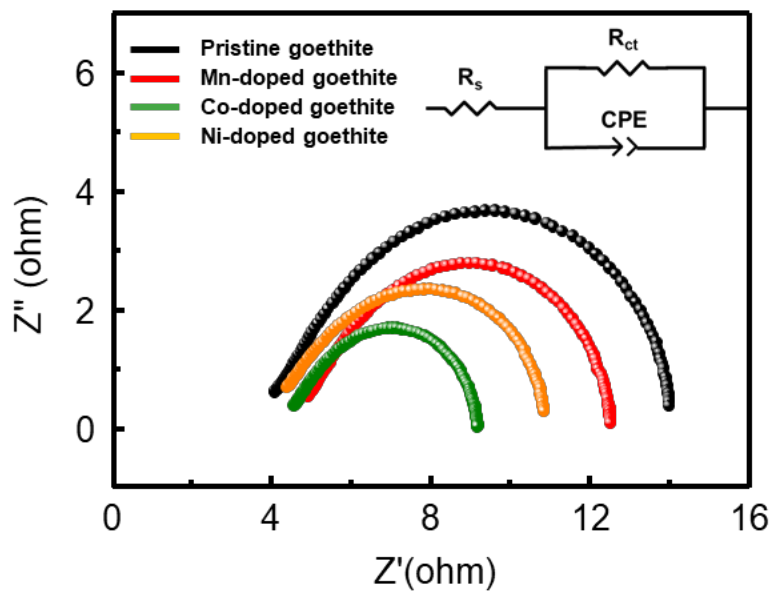


Figure 2.17. Nyquist diagrams of EIS for pristine and dopant-doped goethites in 1M NaOH.

The agreement between DFT results and experimental observations suggests that our approach is an effective method to develop a novel catalyst with maximum catalytic activity by doping. Generally, designing and optimizing new catalysts is a very time-consuming process requiring lots of trial and error. Instead, we use a systematic approach based on first-principles calculations and experimental verification. For the first-principles calculations, we first identify the dominant surface termination bonding with an adsorbate. Then, the overpotential at each step of the catalytic reaction is determined. Finally, the effect of dopants on overpotential is clarified. Though the overpotential values of calculation and experiment have a difference, the trend of catalytic properties in pristine and dopant-doped goethites matches well with each other. To reproduce the overpotential value matches perfectly with the experimental result, it is needed to consider other variables such as the solvent effect. However, the purpose of this work is to predict the trend of catalytic property among different dopants with cost-effective calculation and precise anticipation is out of scope. Since our study shows that first-principles calculation results match well with experimental observations, we believe that this approach can be used for developing a novel catalyst for OER efficiently.

2.5 Conclusion

In this chapter, we investigated the OER mechanisms in pristine, TM-doped goethite using first-principles calculations and verified them with the experiment under a strictly controlled condition. From the surface energy calculation, the plane and its termination, which mainly contribute to the OER, are determined as (001) plane with H & OH termination. The calculated overpotential was highest in the pristine goethite and gradually decreased in the order of Mn, Cr, Ni, and Co-doped goethite. The Fe atom site adjacent to the dopant was also checked. Except for the Ni-doped goethite, there was a scaling relation between ΔG_{OOH^*} and ΔG_{O^*} , which is universally found in other OER catalysts. For goethites with scaling relation, the overpotential is mainly determined by the O^* formation. The pristine goethite has a higher O^* energy than the optimal energy of 1.71 eV, which leads to the large overpotential of 0.94 V. For the TM-doped goethite, O^* is stabilized relative to the pristine goethite. The stabilization of O^* is not enough for Mn-doped goethite and is too much for the Cr-doped goethite. However, Co-doped goethite has the O^* formation energy near the optimal energy and gives the lowest over-potential of 0.41 V. The stabilization of O^* is due to the strengthening of the oxygen-metal binding in various dopant atom active sites. The occupied p-band center of adsorbed oxygen indicates the change in oxygen-metal binding well. To verify the calculation results, the pristine and TM-doped goethite are synthesized in high purity.

Synthesized goethites are highly crystalline and uniform, which are confirmed by the SEM and XRD analysis. The overpotential is measured for the pristine and Mn, Co, and Ni-doped goethites and the tendency of the overpotential change matches well with the calculation results. Findings in this study suggest the thermodynamic explanation about the OER performance of the goethite and provide the theoretical guideline to find out the optimal dopant for the catalyst material. We figured out that the dopant atom at the outermost layer becomes the active site of OER and the change of the active site is the most critical factor to reflect the catalytic property. Other factors such as surface dopant concentration or the presence of oxygen vacancy, have a negligible influence on the catalytic property. By excluding minor factors, we could efficiently find out the trend among various dopants. Though the result of this study is limited to the goethite, we anticipate that the methodology in this study can be the milestone for future catalyst development and optimization.

2.6 References

- [1] M. Gratzel, Photoelectrochemical Cells. *Nature* **2001**, 414, 338–344.
- [2] M. G. Walter, E. L. Warren, J. R. McKone, S. W. Boettcher, Q. Mi, E. A. Santori, N. S. Lewis, Solar Water Splitting Cells. *Chem. Rev.* **2010**, 110, 6446–6473.
- [3] H. Park, I. J. Park, M. G. Lee, K. C. Kwon, S. P. Hong, D. H. Kim, S. A. Lee, T. H. Lee, C. Kim, C. W. Moon, D.-Y. Son, G. H. Jung, H. S. Yang, J. R. Lee, J. Lee, N.-G. Park, S. Y. Kim, J. Y. Kim, H. W. Jang, Water Splitting Exceeding 17% Solar-To-Hydrogen Conversion Efficiency Using Solution-Processed Ni-Based Electrocatalysts and Perovskite/Si Tandem Solar Cell. *ACS Appl. Mater. Interfaces* **2019**, 11, 33835-33843
- [4] M. W. Louie, A. T. Bell, An Investigation of Thin-Film Ni-Fe Oxide Catalysts for the Electrochemical Evolution of Oxygen. *J. Am. Chem. Soc.* **2013**, 135, 12329-12337
- [5] L. Trotochaud, J. K. Ranney, K. N. Williams, S. W. Boettcher, Solution-Cast Metal Oxide Thin Film Electrocatalysts for Oxygen Evolution. *J. Am. Chem. Soc.* **2012**, 134, 17253-17261
- [6] J. Huang, J. Chen, T. Yao, J. He, S. Jiang, Z. Sun, Q. Liu, W. Cheng, F. Hu, Y. Jiang, Z. Pan, S. Wei, CoOOH Nanosheets with High Mass Activity for Water Oxidation. *Angew. Chem. Int. Ed.* **2015**, 54, 8722-8727
- [7] M. Gao, W. Sheng, Z. Zhuang, Q. Fang, S. Gu, J. Jiang, Y. Yan, Efficient Water Oxidation Using Nanostructured α -Nickel-Hydroxide as an

Electrocatalyst. *J. Am. Chem. Soc.* **2014**, 136, 7077-7084

[8] S. A. Lee, T. H. Lee, C. Kim, M. G. Lee, M. J. Choi, H. Park, S. Choi, J. Oh, H. W. Jang, Tailored NiOx/Ni Cocatalysts on Silicon for Highly Efficient Water Splitting Photoanodes via Pulsed Electrodeposition. *ACS Catal.* **2018**, 8, 7261-7269

[9] R. Subbaraman, D. Tripkovic, K. C. Chang, D. Strmcnik, A. P. Paulikas, P. Hirunsit, M. Chan, J. Greeley, V. Stamenkovic, N. M. Markovic, Trends in Activity for the Water Electrolyser Reactions on 3d M(Ni, Co, Fe, Mn) (Oxy)Hydroxide Catalysts. *Nat. Mater.* **2012**, 11, 550-557

[10] Q. Yu, X. Meng, T. Wang, P. Li, J. Ye, Hematite Films Decorated with Nanostructured Ferric Oxyhydroxide as Photoanodes for Efficient and Stable Photoelectrochemical Water Splitting. *Adv. Funct. Mater.* **2015**, 25, 2686-2692

[11] W. D. Chemelewski, H. C. Lee, J. F. Lin, A. J. Bard, C. B. Mullins, Amorphous FeOOH Oxygen Evolution Reaction Catalyst for Photoelectrochemical Water Splitting. *J. Am. Chem. Soc.* **2014**, 136, 2843-2850

[12] S. Zou, M. S. Burke, M. G. Kast, J. Fan, N. Danilovic, S. W. Boettcher, Fe (Oxy)Hydroxide Oxygen Evolution Reaction Electrocatalysis: Intrinsic Activity and the Roles of Electrical Conductivity, Substrate, and Dissolution. *Chem. Mater.* **2015**, 27, 8011-8020

[13] B. Kim, I. Park, G. Yoon, J. S. Kim, H. Kim, J. Jang, Atomistic Investigation of Doping Effects on Electrocatalytic Properties of Cobalt

Oxides for Water Oxidation. *Adv. Sci.* **2018**, 5, 1801632

[14] M. Bajdich, M. Garcia-Mota, A. Vojvodic, J. K. Norskov, A. T. Bell, Theoretical Investigation of Doping Effects on Electrocatalytic Properties on Cobalt Oxides for the Electrochemical Oxidation of Water. *J. Am. Chem. Soc.* **2013**, 135, 13521-13530

[15] B. Zhang, X. Zheng, O. Voznyy, R. Comin, M. Bajdich, M. Garcia-Melchor, L. Han, J. Xu, M. Liu, L. Zheng, F. P. G. de Arquer, C. T. Dinh, F. Fan, M. Yuan, E. Yassitepe, N. Chen, T. Regier, P. Liu, Y. Li, P. De Luna, A. Janmohamed, H. L. Xin, H. Yang, A. Vojvodic, E. H. Sargent, Homogeneously Dispersed Multimetal Oxygen-Evolving Catalysts. *Science*, **2016**, 352, 333-337

[16] L. Trotochaud, S. L. Young, J. K. Ranney, S. W. Boettcher, Nickel-Iron Oxyhydroxide Oxygen-Evolution Electrocatalysts: The Role of Intentional and Incidental Iron Incorporation. *J. Am. Chem. Soc.* **2014**, 136, 6744-6753

[17] Y. Dong, P. Zhang, Y. Kou, Z. Yang, Y. Li, X. A. Sun. A First-Principles Study of Oxygen Formation Over NiFe-Layered Double Hydroxides. *Surface Catal. Lett.* **2015**, 145, 1541-1548

[18] D. Friebel, M. W. Louie, M. Bajdich, K. E. Sanwald, Y. Cai, A. M. Wise, M.-J. Cheng, D. Sokaras, T.-C. Weng, R. Alonso-Mori, R. C. Davis, J. R. Bargar, J. K. Norskov, A. Nilsson, A. T. Bell, Identification of Highly Active Fe Sites in (Ni, Fe)OOH for Electrocatalytic Water Splitting. *J. Am. Chem. Soc.* **2015**, 137, 1305-1313

- [19] M. S. Burke, M. G. Kast, L. Trotochaud, A. M. Smith, S. W. Boettcher, Cobalt-Iron (Oxy)Hydroxide Oxygen Evolution Electrocatalysts: The Role of Structure and Composition on Activity, Stability, and Mechanisms. *J. Am. Chem. Soc.* **2015**, 137, 3638-3648
- [20] Y. F. Li, A. Selloni, Mechanism and Activity of Water Oxidation on Selected Surfaces of Pure and Fe-Doped NiO_x. *ACS Catal.* **2014**, 4, 1148-1153
- [21] D. Inohara, H. Maruyama, Y. Kakihara, H. Kurosawa, M. Nakayama, Cobalt-Doped Goethite-Type Iron Oxyhydroxide (α -FeOOH) for Highly Efficient Oxygen Evolution Catalysis. *ACS Omega* **2018**, 3, 7840-7845
- [22] W. D. Chemelwski, J. R. Rosenstock, C. B. Mullins, Electrodeposition of Ni-Doped FeOOH Oxygen Evolution Reaction Catalyst for Photoelectrochemical Water Splitting. *J. Mater. Chem. A* **2014**, 2, 14957-14962
- [23] J. Suntivich, K. J. May, H. A. Gasteiger, J. B. Goodenough, Y. Shao-Horn, A Perovskite Oxide Optimized for Oxygen Evolution Catalysis from Molecular Orbital Principles. *Science*, **2011**, 334, 1383-1385
- [24] W. Zhou, J. Sunarso, Enhancing Bi-Functional Electrocatalytic Activity of Perovskite by Temperature Shock: A Case Study of LaNiO_{3- δ} . *J. Phys. Chem. Lett.* **2013**, 4, 2982-2988
- [25] A. Grimaud, K. J. May, C. E. Carlton, Y. L. Lee, M. Risch, W. T. Hong, J. Zhou, Y. Shao-Horn, Double Perovskites as a Family of Highly Active Catalysts for Oxygen Evolution in Alkaline Solution. *Nat. Commun.* **2013**, 4,

- [26] R. Jacobs, J. Hwang, Y. Shao-Horn, D. Morgan, Assessing Correlations of Perovskite Catalytic Performance with Electronic Structure Descriptors. *Chem. Mater.* **2019**, 31, 785-797
- [27] C. Chen, F. Ciucci, Designing Fe-Based Oxygen Catalysts by Density Functional Theory Calculations. *Chem. Mater.* **2016**, 28, 7058-7065
- [28] W. T. Hong, K. A. Stoerzinger, Y. L. Lee, L. Giordano, A. Grimaud, A. M. Johnson, J. Hwang, E. J. Crumlin, W. Yang, Y. Shao-Horn, Charge-Transfer-Energy-Dependent Oxygen Evolution Reaction Mechanisms for Perovskite Oxides. *Energy Environ. Sci.* **2017**, 10, 2190-2200
- [29] J. Suntivich, W. T. Hong, Y. Lee, J. M. Rondinelli, W. Yang, J. B. Goodenough, B. Dabrowski, J. W. Freeland, Y. Shao-Horn, Estimating Hybridization of Transition Metal and Oxygen States in Perovskites from O K-edge X-ray Absorption Spectroscopy. *J. Phys. Chem. C* **2014**, 118, 1856-1863
- [30] G. Kresse, J. Furthmuller, Efficiency of Ab-Initio Total Energy Calculations for Metals and Semiconductors Using a Plane-Wave Basis Set. *Comput. Mater. Sci.* **1996**, 6, 15-50
- [31] G. Kresse, J. Furthmuller, Efficient Iterative Schemes for Ab Initio Total-energy Calculations Using a Plane-Wave Basis Set. *Phys. Rev. B: Condens. Matter Mater. Phys.* **1996**, 54, 11169-11186
- [32] P. Hohenberg, W. Kohn, Inhomogeneous Electron Gas. *Phys. Rev.* **1964**, 136, B864-B871

- [33] W. Kohn, L. J. Sham, Self-Consistent Equations Including Exchange and Correlation Effects. *Phys. Rev.* **1965**, 140, A1133-A1138
- [34] F. Han, Projector-Augmented Plane-Wave Method. *Probl. Solid State Phy. with Solut.* **2011**, 50, 391-396
- [35] G. Kresse, D. Joubert, From Ultrasoft Pseudopotentials to the Projector Augmented-Wave Method. *Phys. Rev. B: Condens. Matter Mater. Phys.* **1999**, 59, 1758
- [36] J. P. Perdew, K. Burke, M. Ernzerhof, Generalized Gradient Approximation Made Simple. *Phys. Rev. Lett.* **1996**, 77, 3865-3868
- [37] R. Barik, B. K. Jena, M. Mohapatra, Metal Doped Mesoporous FeOOH Nanorods for High Performance Supercapacitors. *RSC Adv.* **2017**, 7, 49083-49090
- [38] P. Makie, P. Persson, L. Osterlund, Solar Light Degradation of Trimethyl Phosphate and Triethyl Phosphate on Dry and Water Precovered Hematite and Goethite Nanoparticles. *J. Phys. Chem. C* **2012**, 116, 14917-14929
- [39] Y. Wu, W. Hu, R. Xie, X. Liu, D. Yang, P. Chen, J. Zhang, F. Zhang, Composite of Nano-Goethite and Natural Organic Luffa Spunge as Template: Synergy of High Efficiency Adsorption and Visible-Light Photocatalysis. *Inorg. Chem. Commun.* **2018**, 98, 115-119
- [40] V. Alexandrov, K. M. Rosso, Electron Transport in Pure and Substituted Iron Oxyhydroxides by Small-Polaron Migration. *J. Chem. Phys.* **2014**, 140, 234701

- [41] W. Luo, C. Jiang, Y. Li, S. A. Shevlin, X. Han, K. Quo, Y. Cheng, Z. Guo, W. Huang, J. Tang, Highly Crystallized α -FeOOH for Stable and Efficient Oxygen Evolution Reaction. *J. Mater. Chem. A* **2017**, 5, 2021-2028
- [42] V. Alexandrov, K. M. Rosso, Ab Initio Modeling of Fe(II) Adsorption and Interfacial Electron Transfer at Goethite (α -FeOOH) Surfaces. *Phys. Chem. Chem. Phys.* **2015**, 17, 14518-14531
- [43] K. Otte, W. W. Schmahl, R. Pentcheva, Density Functional Theory Study of Water Adsorption on FeOOH Surfaces. *Surf. Sci.* **2012**, 606, 1623-1632
- [44] A. Jain, G. Hautier, S. P. Ong, C. J. Moore, C. C. Fischer, K. A. Pearson, G. Ceder, Formation Enthalpies by Mixing GGA and GGA+U Calculations. *Phys. Rev. B: Condens. Matter Mater. Phys.* **2011**, 84, 045115
- [45] D. Tunega, Theoretical Study of Properties of Goethite (α -FeOOH) at Ambient and High-Pressure Conditions. *J. Phys. Chem. C* **2012**, 116, 6703-6713
- [46] J. B. Forsyth, I. G. Hedley, C. E. Johnson, The Magnetic Structure and hyperfine Field of Goethite (α -FeOOH). *J. Phys. C: Solid State Phys.* **1968**, 1, 179-188
- [47] C. F. Sampson, The Lattice Parameters of Natural Single Crystal and Synthetically Produced Goethite (α -FeOOH). *Acta Crystallogr. Sect. B: Struct. Crystallogr. Cryst. Chem.* **1968**, 25, 1683-1685
- [48] L. Bengtsson, Dipole Correction for Surface Supercell Calculations.

- Phys. Rev. B: Condens. Matter Mater. Phys.* **1999**, 59, 12301-12304
- [49] K. Reuter, M. Scheffler, Composition, Structure, and Stability of RuO₂(110) as a Function of Oxygen Pressure. *Phys. Rev. B: Condens. Matter Mater. Phys.* **2001**, 65, 035406
- [50] D. R. Chowdhury, L. Speccia, S. S. Amritphale, A. Paul, A. A. Singh, Robust Iron Oxyhydroxide Water Oxidation Catalyst Operating under near Neutral and Alkaline Conditions. *J. Mater. Chem. A* **2016**, 4, 3655-3660
- [51] B. Morgan, O. Lahav, The Effect of pH on the Kinetics of Spontaneous Fe(II) Oxidation by O₂ in Aqueous Solution – Basic Principles and a Simple Heuristic Description. *Chemosphere* **2007**, 68, 2080-2084
- [52] L. Martinez, D. Leinen, F. Martin, M. Gabas, J. R. Ramos-Barrado, E. Quagliata, E. A. Dalchiele, Electrochemical Growth of Diverse Iron Oxide (Fe₃O₄, α-FeOOH, and γ-FeOOH) Thin Films by Electrodeposition Potential Tuning. *J. Electrochem. Soc.* **2007**, 154, D126-D133
- [53] S. Bijani, L. Martinez, E. A. Dalchiele, M. Gabas, R. Schrebler, J. R. Ramos-Barrado, Surface Morphological Control of Nanostructured Single-Phase Fe₃O₄, α-FeOOH, and γ-FeOOH Electrodeposited Thin Films. *J. Electrochem. Soc.* **2016**, 163, D366-D373
- [54] B. Russell, M. Payne, L. C. Ciacchi, Density Functional Theory Study of Fe(II) Adsorption and Oxidation on Goethite Surfaces. *Phys. Rev. B: Condens. Matter Mater. Phys.* **2009**, 80, 165101
- [55] H. Guo, A. S. Barnard, Thermodynamic Modelling of Nanomorphologies of Hematite and Goethite. *J. Mater. Chem.* **2011**, 21,

11566-11577

[56] N. H. de Leeuw, T. G. Cooper, Surface Simulation Studies of the Hydration of White Rust $\text{Fe}(\text{OH})_2$, Goethite $\alpha\text{-FeO}(\text{OH})$ and Hematite $\alpha\text{-Fe}_2\text{O}_3$. *Geochim. Cosmochim. Acta* **2007**, 71, 1655-1673

[57] I. C. Man, H. Y. Su, F. Calle-Vallejo, H. A. Hansen, J. L. Martinez, N. G. Inoglu, J. Kitchin, T. F. Jaramillo, J. K. Norskov, J. Rossmeisl, Universality in Oxygen Evolution Electrocatalysis on Oxide Surfaces. *ChemCatChem* **2011**, 3, 1159-1165

[58] M. Garcia-Mota, A. Vojvodic, H. Metiu, I. C. Man, H. Y. Su, J. Rossmeisl, J. K. Norskov, Tailoring the Activity for Oxygen Evolution Electrocatalysis on Rutile $\text{TiO}_2(110)$ by Transition-Metal Substitution. *ChemCatChem* **2011**, 3, 1607-1611

[59] X. Cui, P. Ren, D. Deng, J. Deng, X. Bao, Single Layer Graphene Encapsulating Non-Precious Metals as High-Performance Electrocatalysts for Water Oxidation. *Energy Environ. Sci.* **2016**, 9, 123-129

[60] H. Li, Y. Chen, S. Xi, J. Wang, S. Sun, Y. Sun, Y. Du, Z. J. Xu, Degree of Geometric Tilting Determines the Activity of FeO_6 Octahedra for Water Oxidation. *Chem. Mater.* **2018**, 30, 4313-4320

[61] W. T. Hong, R. E. Welsch, Y. Shao-Horn, Descriptors of Oxygen-Evolution Activity for Oxides: A Statistical Evaluation. *J. Phys. Chem. C* **2016**, 120, 78-86

[62] G. Fu, X. Wen, S. Xi, Z. Chen, W. Li, J. Y. Zhang, A. Tadich, R. Wu, D. C. Qi, Y. Du, J. Cheng, K. H. L. Zhang, Tuning the Electronic Structure

- of NiO via Li Doping for the Fast Oxygen Evolution Reaction. *Chem. Mater.* **2019**, 31, 419-428
- [63] Y. Duan, S. Sun, S. Xi, X. Ren, Y. Zhou, G. Zhang, H. Yang, Y. Du, Z. J. Xu, Tailoring the Co 3d-O 2p Covalency in LaCoO₃ by Fe Substitution to Promote Oxygen Evolution Reaction. *Chem. Mater.* **2017**, 29, 10534-10541
- [64] J. H. Montoya, A. D. Doyle, J. K. Norskov, A. Vojvodic, Trends in Adsorption of Electrocatalytic Water Splitting Intermediates on Cubic ABO₃ Oxides. *Phys. Chem. Chem. Phys.* **2018**, 20, 3813-3818
- [65] Y. L. Lee, J. Kleis, J. Rossmeisl, S. H. Yang, D. Morgan, Prediction of Solid Oxide Fuel Cell Cathode Activity with First-Principles Descriptors. *Energy Environ. Sci.* **2011**, 4, 3966-3970
- [66] M. V. Morales, E. Asedegbega-Neto, A. Uglesias-Juez, I. Rodriguez-Ramos, A. Guerrero-Ruiz, Role of Exposed Surfaces on Zinc Oxide nanostructures in the Catalytic Ethanol Transformation. *ChemSusChem* **2015**, 8, 2223-2230
- [67] Y. H. Fang, Z. P. Liu, Tafel Kinetics of Electrocatalytic Reactions: From Experiment to First-Principles. *ACS Catal.* **2014**, 4, 4364-4376

Chapter 3.

Theoretical Approach on the Enhanced Catalytic Property of the Bi Decorated GaN Nanowire for the Formic Acid Generation

3.1 Introduction

With the abrupt rise of CO₂ emission, the amount of CO₂ in the atmosphere has been continuously increased. As it is well known, the CO₂ gas in the atmosphere plays a major role in elevating the temperature, which is called the greenhouse effect. The accumulating greenhouse gas in the atmosphere leads to worldwide climate change, brings about various environmental problems.^[1] Among problems, the sea level rise is one of the most urgent issues. According to the NASA Goddard Space Flight Center, from 1993, sea level has risen around 100 mm, mainly due to the melting of the glacier. To suppress such environmental issues, the net emission of CO₂ should be controlled under zero until 2050 for the limitation of temperature rise to 1.5 °C, the pre-industrial level.^[2]

Along with limiting the emission of CO₂ gas, various strategies to remove CO₂ from the atmosphere are also applied. Strategies can be categorized as decarbonization, carbon sequestration and, and carbon recycling. Decarbonization can be summarized as the usage of a low carbon power source, which leads to the reduction of CO₂ emissions. Carbon sequestration can be represented as the strategies like direct air capture and storage or ocean fertilization. The above methods to reduce the CO₂ in the atmosphere cannot be the ultimate solution in the long term, as the absolute amount of

CO₂ is maintained. On the other hand, carbon recycling chemically converts CO₂ into an advantageous material that can be utilized for other purposes. As CO₂ is the most oxidized form of carbon, the recycling process of CO₂ inevitably involves the reduction reaction. Similar to the hydrogen evolution reaction (HER) of the water splitting process, most CO₂ reduction is carried out through an electrochemical process.

The electrochemical reduction of CO₂ can generate various products, from carbon monoxide, formic acid, methanol to even multicarbon hydrocarbons. Due to diverse products, the reaction pathways of the CO₂ reduction are extremely complex as seen from Figure 3.1.^[3] With the complicated reaction kinetics, it is very difficult to achieve a high yield for the desired product. Therefore, not only for the highly efficient reaction process with low overpotential but also for the selectivity toward the desired product, numerous approaches on CO₂ reduction catalysts are in progress.

In this chapter, the highly efficient Bi nanoparticles (NPs)-supported on GaN nanowires (NWs) CO₂ reduction catalyst grown on Si substrate will be demonstrated. According to the experimental results acquired by W. J. Dong, Bi NPs with GaN NW gives high selectivity toward the formic acid generation. Based on the electrochemical measurement and characterization results, the mechanism of high selectivity and efficiency achievement will be discussed by the first-principles calculations simulation. Through the stepwise comparison of GaN NW/Si, Bi NP/Si and Bi NP/GaN NW/Si, the improved selectivity and enhanced photocurrent density can be explained

3.2 Experimental Results

3.2.1 Fabrication of Bi/GaN NWs/Si

As mentioned in the introduction, whole fabrication, photoelectrochemical measurements, and characterization data were acquired by W. J. Dong. In this section, experimental results, which are essential to understand the theoretical approach presented in the following chapter, will be briefly demonstrated.

As the substrate for GaN NWs and Bi NPs, the n^+ -p junction was fabricated at the surface of the Si wafer through a thermal diffusion process. The GaN NWs were grown with plasma-assisted molecular-beam epitaxy on the silicon wafer. Bi NPs were deposited on GaN NWs/Si and Si by a thermal evaporation method.

3.2.2 Characterization of Bi/GaN NWs/Si

The morphology of synthesized GaN NWs and Bi decorated GaN NWs was investigated with scanning electron microscopy (SEM) analysis. According to Figure 3.2(a), GaN NWs have a diameter of ~ 50 nm and length of ~ 400 nm with a uniform morphology throughout the deposited area. After the decoration of Bi NPs on the GaN NWs, the presence of the Bi NPs can be notified by the roughened surface morphology, as can be seen from Figure 3.2(b).

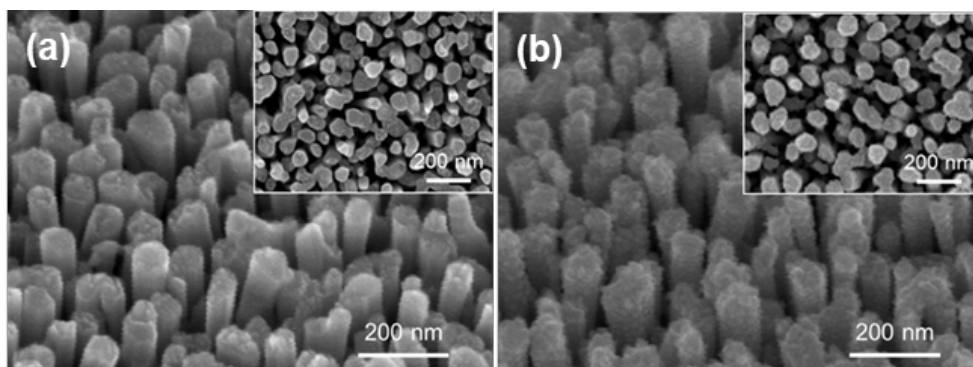


Figure 3.2. SEM images of the (a) GaN NWs and, (b) Bi NPs decorated GaN NWs.

To confirm the microstructure of GaN NWs and decorated Bi NPs, transmission electron microscopy analysis was performed. From the high magnification image of Figure 3.3, it was possible to observe the uniformly deposited Bi NPs. With the diffraction pattern of the GaN NW acquired from Fast Fourier Transform (FFT), the GaN NWs are turned out to grow in direction of [002], with the exposed surface facet of (100). The size of decorated Bi NPs was around 10~15 nm.

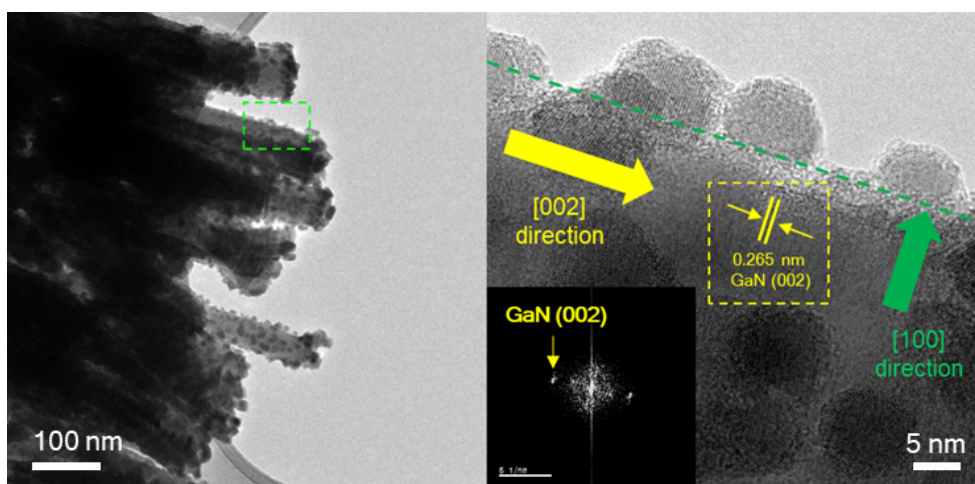


Figure 3.3. TEM images of Bi NPs decorated GaN NWs.

For the investigation of surface chemical bonding states, X-ray photoelectron spectroscopy (XPS) was carried out. XPS spectra for GaN NWs, as-synthesized Bi/GaN NWs, and Bi/GaN NWs after CO₂ reduction reaction are presented in Figure 3.4. From the Ga 2p_{3/2} spectra, a major peak of Ga-N bond (1118.0 eV) with a minor peak of Ga-O bond (1119.2 eV) is observed for all samples.^[4] For the N 1s spectra, N-Ga bond and Ga LMM Auger electrons peaks are considered to be the major peaks while the N-H minor peak is also separated.^[5, 6] The bond state of Bi NPs can be revealed from the deconvolution of Bi 4f spectra. For the as-synthesized Bi/GaN NWs, the decorated Bi has the peak of metallic Bi⁰ (156.4 and 161.7 eV) and Bi³⁺ (158.5 and 163.6 eV).^[7] It is noteworthy that the Bi³⁺ peak, which assumed to be originated from native oxide of Bi surface, gives much stronger intensity compared to the metallic Bi⁰. Even in the sample after CO₂ reduction, the metallic Bi⁰ completely disappeared, which means that Bi is fully oxidized during the reaction. The O 1s peaks can be deconvoluted into 4 peaks of oxygen species on GaN and Bi. That on GaN NWs is indexed as O-Ga (531.1 eV) while those on Bi NPs are confirmed to be O-Bi (529.4 eV) and OH-Bi (530.9 eV). One remaining peak is figured out to be adsorbed water molecules and hydroxyls (532.2 eV).^[8, 9]

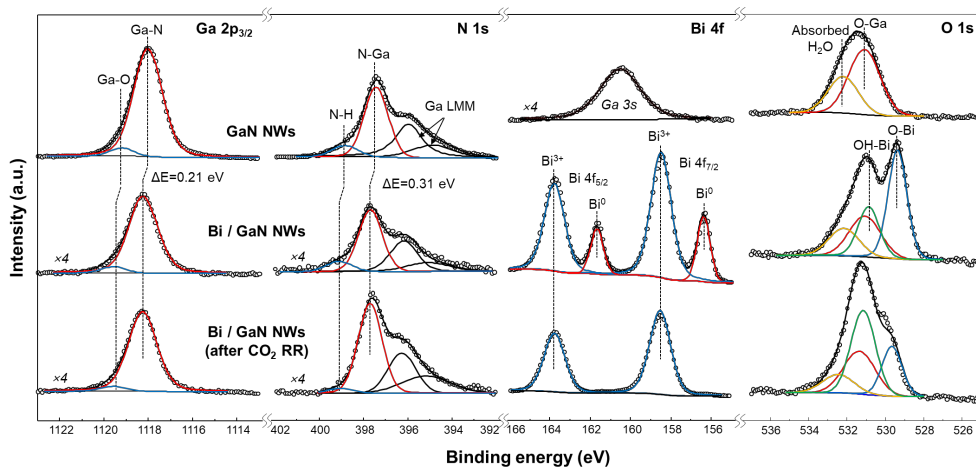


Figure 3.4. XPS spectra of GaN NWs, Bi/GaN NWs, and Bi/GaN NWs after CO₂ reduction reaction.

3.2.3 Photoelectrochemical Measurement of Bi/GaN NWs/Si

To compare the catalytic property of the GaN NWs/Si, Bi/Si and, Bi/GaN NWs/Si samples, photoelectrochemical measurement was performed by illuminating light of 100 mW/cm^2 . The overall outline of the Bi/GaN NWs/Si sample is presented in Figure 3.5. With the narrow bandgap of 1.1 eV, the Si layer mainly plays the role of light absorption, especially for the visible light range. For GaN NWs, they form the type-II junction with Si substrate, which effectively separates the photogenerated electrons and holes, suppressing the recombination. In addition, GaN NWs also prevent the photodegradation of the Si substrate by passivating the surface of Si. Bi is deposited as a co-catalyst on the surface of GaN NWs and catalytic reaction for formic acid generation is anticipated to occur at the Bi surface.

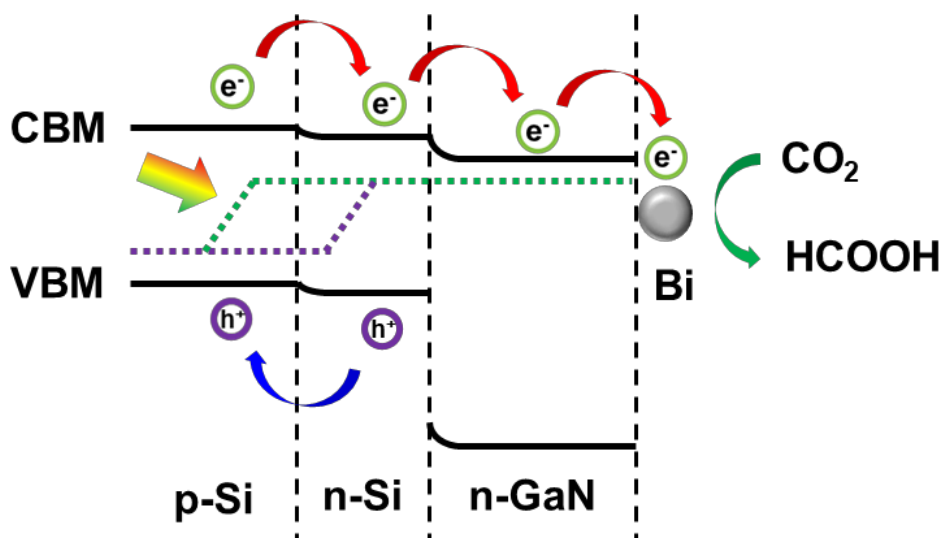


Figure 3.5. Band alignment diagram of the Bi/GaN NWs/Si.

As the simulation part mainly focuses on the efficient generation of the formic acid among other CO₂ reduction products, the measurement results are primarily represented as the comparison between CO₂ reduction products. In Figure 3.6, the faradaic efficiency of the CO₂ reduction reaction for GaN NWs/Si, Bi/Si, and Bi/GaN NWs/Si samples are presented. According to the faradaic efficiency of GaN NWs/Si, the total efficiency value for CO₂ reduction reaction is much lower than others. This is because the hydrogen evolution reaction, the side reaction for CO₂ reduction, mainly occurs at the GaN NWs, as the combination of GaN and Si was known to be an effective photoelectrode for water splitting reaction.^[10, 11] Besides, the CO₂ reduction on GaN NWs generates carbon monoxide, formic acid and methane. At the low potential range, carbon monoxide, and formic acid are observed while the portion of methane increases at a higher potential. The portion of formic acid between other products is $FE_{\text{HCOOH}} = 69.7\%$ at $-0.5 V_{\text{RHE}}$, even lower at the higher potential. On the other hand, for the Bi/Si sample, the total CO₂ reduction is mostly composed of the formic acid generation with the faradaic efficiency of $FE_{\text{HCOOH}} > 92\%$. Such tendency of high HCOOH faradaic efficiency is also observed from the Bi/GaN NWs/Si sample, which means that the decoration of Bi NPs provides the selectivity toward formic acid generation by CO₂ reduction.

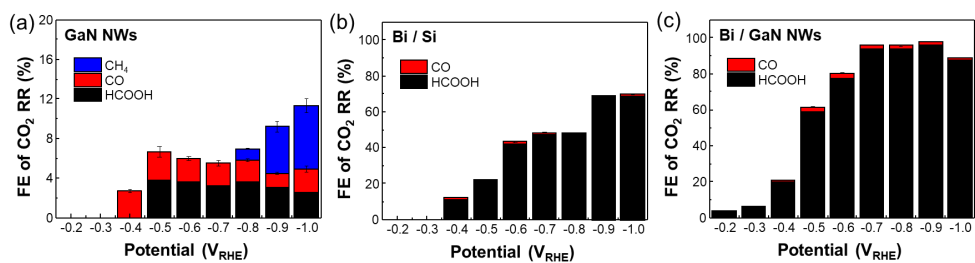


Figure 3.6. Faradaic efficiency for CO₂ reduction reaction products of (a) GaN NWs/Si, (b) Bi/Si, and (c) Bi/GaN NWs/Si sample.

Along with faradaic efficiency, the photocurrent of CO₂ reduction products is investigated for each sample. According to Figure 3.7, the GaN NWs/Si gives the low photocurrent value for a total ~ 1 mA/cm² at the -1.0 V_{RHE}, due to the low reactivity of GaN toward CO₂ reduction reaction. With the use of Bi catalyst, the photocurrent increased to nearly twice, which is mostly from formic acid generation. Still, even larger enhancement was observed from the Bi/GaN NWs/Si sample, as seen in Figure 3.7(c). With the excellent selectivity toward the formic acid, the current density of ~8 mA/cm² at -1.0 V_{RHE} is acquired, which is almost 4 times higher than that of Bi/Si. Though the faradaic efficiency for the formic acid of Bi/GaN NWs/Si sample increased nearly 20~40% when compared to Bi/Si, considering the degree of the photocurrent enhancement, it is not enough to explain with faradaic efficiency alone.

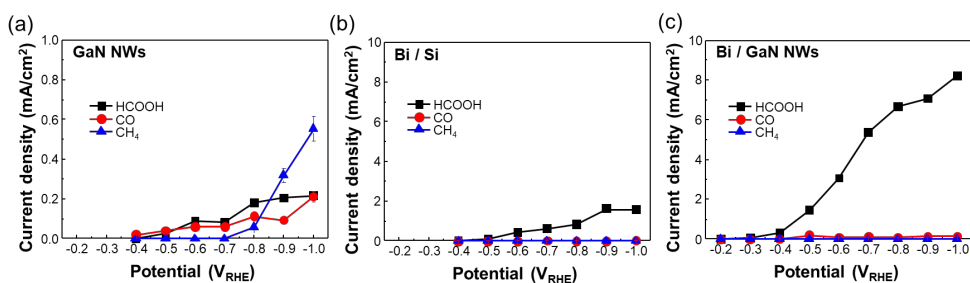


Figure 3.7. Partial current density of photoelectrochemical CO₂ reduction reaction products for (a) GaN NWs/Si, (b) Bi/Si, and (c) Bi/GaN NWs/Si.

To sum up the photoelectrochemical measurement data, the catalytic property enhancement can be summarized in two steps. First, from the faradaic efficiency of samples, it is confirmed that the selectivity toward formic acid can be achieved. Second, the construction of Bi/GaN NWs/Si heterostructure can generate a much higher photocurrent than individual GaN NWs or Bi catalysts. In the following chapter, each catalytic property enhancement will be explained with the first principles calculation results.

3.3 Theoretical Approach

3.3.1 Computational Details

First-principles density functional theory (DFT) calculations were performed with the projector augmented wave (PAW) method and the generalized gradient approximation of Perdew, Burke, and Ernzerhof (PBE) for exchange-correlation potential and implemented in Vienna Ab initio Simulation Package (VASP) code.^[12-17] The conventional DFT energy is corrected by Grimme's method (D3) in order to describe van der Waals interaction properly. Dipole correction along the slab cell c-axis is employed due to the asymmetric layer arrangement. An energy cutoff of 400 eV was used for the plane-wave representation of the wavefunctions. Atomic structures were relaxed until all the Hellman-Feynman forces were < 0.01 eV/Å and the criteria for the electronic step convergence was 10^{-5} .

3.3.2 Surface Modeling

All GaN, Bi₂O₃, and GaN-Bi₂O₃ composite slabs are constructed from the fully relaxed bulk structure of GaN and Bi₂O₃. Based on the crystallographic direction of GaN NW and surface energy of Bi₂O₃,^[18] surface vacuum slab with (100) and (010) surface are fabricated respectively. The thickness of the GaN and Bi₂O₃ slabs are controlled to be at least 12 Å, composed of 5 unit cells periodically along the direction perpendicular to the surface. To mimic the bulk-like property, the bottom 2 layers are fixed while the surface 3 layers are fully relaxed. For GaN-Bi₂O₃ composite slab, to alleviate the computational load, the thickness of the GaN slab is reduced to 3 layers. A (010) surface of Bi₂O₃ single unit cell is placed on the most energetically favorable site of fully relaxed GaN (100) surface followed by complete relaxation. The vacuum region of slab cells was set to be more than 15 Å, to avoid the artificial interaction between periodic images. For the GaN and GaN-Bi₂O₃ slab with rectangular cell modeling, Monkhorst-Pack k-point sampling with a grid of 4×2×1 was used for the Brillouin zone integration. In the case of monoclinic Bi₂O₃, gamma-centered k-point sampling of 4×4×1 is employed.

To determine the surface termination of GaN (100) and Bi₂O₃ (010) surfaces, the binding energy of adsorbates on both surfaces is calculated. As the CO₂ reduction reaction occurs at an aqueous solution of 0.1 M KHCO₃ electrolyte, types of adsorbates are limited to OH, O, H, and H₂O. The

binding energy (E_b) can be calculated as below.

$$E_b = -[E_{ads} - E_{slab} - n\mu_{ads}]$$

The energy of surface slab with and without adsorbate is represented as E_{ads} and E_{slab} respectively. μ_{ads} denotes the chemical potential of adsorbates and the equation of the adsorbate chemical potential can be found in Chapter 2.2.3. The number of adsorbate atoms/molecules is expressed as n for the surface termination coverage.

3.3.3 Reaction Pathway of CO₂ Reduction

As the purpose of the simulation is to understand the mechanism of enhanced selectivity toward formic acid, not whole the reaction pathways for CO₂ reduction products will be considered. From Figure 3.1, it is possible to figure out that the branching of the reaction pathway between formic acid and other products in the CO₂ reduction reaction is determined at the initial steps of the full reaction. The initial steps of the CO₂ reduction reaction are depicted in Figure 3.8. From numerous researches, most mechanisms agree that the binding form of the reaction intermediate determines the final product. As seen in Figure 3.8, if the reaction intermediate binds on the catalyst surface through the oxygen atom, the formate is generated while the carbon bonding leads to the carbon monoxide pathway. Therefore, whether this intermediate binds through a carbon atom or oxygen atom can be the key distinction to determine the selectivity toward formic acid generation.

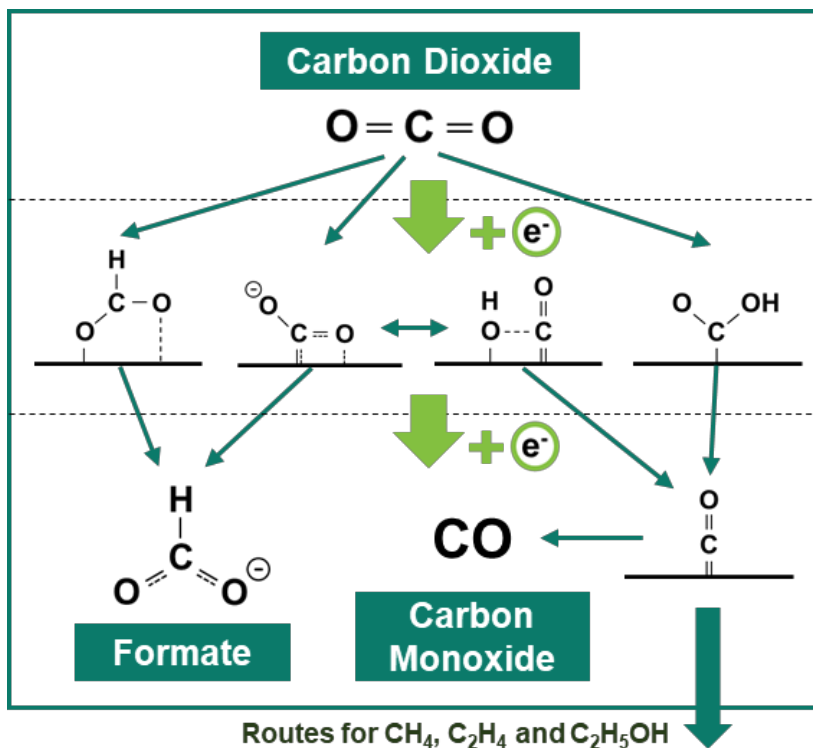
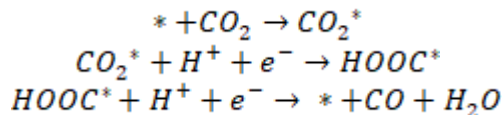


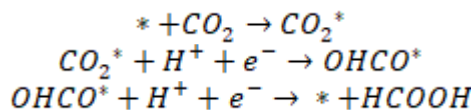
Figure 3.8. Initial steps of the CO_2 reduction reaction.

To calculate the reaction barrier of the CO₂ reduction reaction, the exact steps for the formic acid and carbon monoxide are expressed as below

For carbon monoxide pathway,



and for formic acid pathway,



The reaction barrier for each steps can be presented as follows. (2-1 & 3-1

for CO pathway and 2-2 & 3-2 for HCOOH pathway)

$$\begin{aligned} \Delta E_1 &= E_{\text{CO}_2^*} - E_* + \Delta \text{ZPE} + eU \\ \Delta E_{2-1} &= E_{\text{HOOC}^*} - E_{\text{CO}_2^*} - E_{\text{H}} + \Delta \text{ZPE} + eU \\ \Delta E_{3-1} &= E_{\text{CO}} + E_{\text{H}_2\text{O}} - E_{\text{HOOC}^*} - E_{\text{H}} + \Delta \text{ZPE} + eU \\ \Delta E_{2-2} &= E_{\text{OHCO}^*} - E_{\text{CO}_2^*} - E_{\text{H}} + \Delta \text{ZPE} + eU \\ \Delta E_{3-2} &= E_{\text{HCOOH}} - E_{\text{OHCO}^*} - E_{\text{H}} + \Delta \text{ZPE} + eU \end{aligned}$$

In equations, U is the electrode potential with respect to the normal hydrogen electrode (NHE) at the standard condition. E_i and ZPE denote the energy of the intermediate state or gas molecule and the zero-point energy, respectively. The ZPE is calculated only for the adsorbed species and reactant molecules. The formation energy and ZPE values for gas molecules are presented in Table 3.1.

	H ₂	H ₂ O	CO	CO ₂	HCOOH
E_{DFT} (eV)	-6.73	-14.22	-14.8	-22.99	-29.92
ZPE (eV)	0.26	0.71	0.21	0.29	1.04

Table 3.1. Calculated total energy and zero-point energy of reactants and

product molecules

3.4 Result and Discussion

3.4.1 Surface Determination

Before discussing the reaction barriers of GaN and Bi₂O₃, the most stable surface termination was determined based on the adsorbate binding energy.

In Figure 3.9(a), the binding energy of various adsorbates on the GaN (100)

surface is presented. Among different adsorbates, the chemisorption of the water molecule is confirmed as the most stable surface structure. As seen in Figure 3.9(b) and (c), the oxygen of the hydroxide binds with the gallium atom while the separated hydrogen atom binds to the nitrogen atom. The surface structure of GaN from simulation matches well with the XPS data of Figure 3.4, which confirmed that GaN NWs have surface bonding of Ga-O and N-H. The coverage of the hydrogen chemisorption on the GaN (100) surface is also investigated in Figure 3.10. The binding energy increases until the GaN surface is completely covered with a chemisorbed water molecule, indicating that the fully water-chemisorbed surface termination is thermodynamically the most stable. The surface structure of the water chemisorbed GaN (100) surface with 100 % coverage is depicted in Figure 3.10(b) and (c).

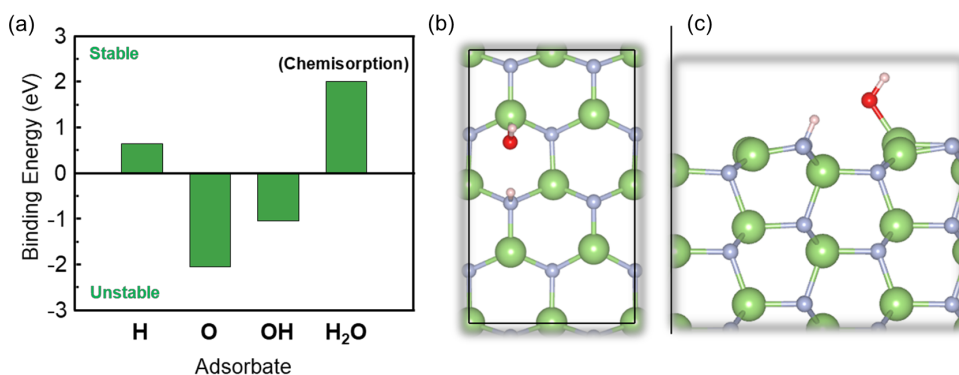


Figure 3.9. (a) Calculated binding energy of various adsorbates on the GaN (001) surface. (b) Top view image and (c) side view image of the water molecule chemisorbed GaN (001) surface.

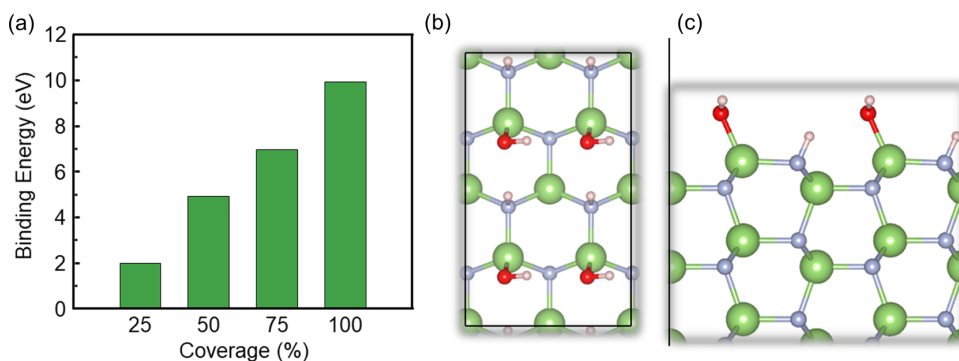


Figure 3.10. (a) Calculated binding energy of H₂O chemisorption with various coverage on the GaN (001) surface. (b) Top view image and (c) side view image of the GaN (001) surface fully covered with the chemisorbed water molecule.

The Bi catalyst of the experiment is modeled as Bi₂O₃, based on the XPS result of Bi 4f spectra. As mentioned in Chapter 3.2.2, Bi is completely

oxidized to Bi^{3+} during the CO_2 reduction reaction. Thus the Bi_2O_3 is selected as the most stable oxidized form of Bi for simulation. Similar to GaN (100) surface, the binding energy for adsorbates was investigated on Bi_2O_3 (010) surface as shown in Figure 3.11(a). While the adsorption of other adsorbates is confirmed to be thermodynamically unstable, only the chemisorption of the water molecule has positive binding energy. Due to the high electronegativity of the Bi, the additional chemisorption of the water molecule did not occur. The surface structure of the water molecule chemisorbed Bi_2O_3 (010) surface is presented in Figure 3.11(b) and (c).

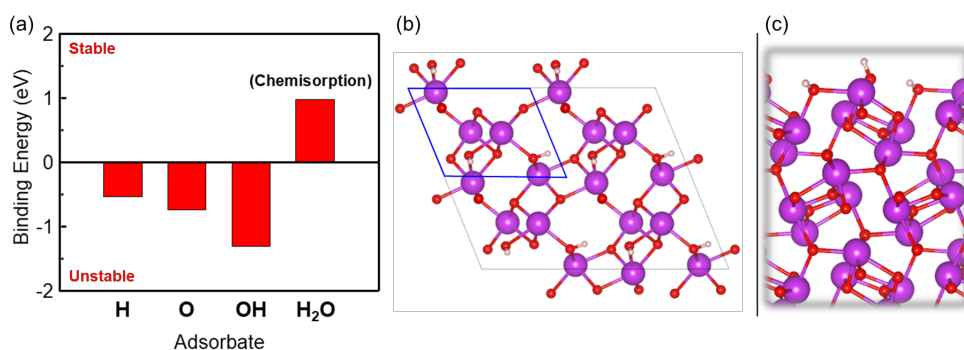


Figure 3.11. (a) Calculated binding energy of various adsorbates on the Bi_2O_3 (001) surface. (b) Top view image and (c) side view image of the water molecule chemisorbed Bi_2O_3 (001) surface.

Finally, the surface termination of the GaN- Bi_2O_3 composite is determined based on the results of individual GaN and Bi_2O_3 surfaces. For the GaN surface, without the position which bonds with Bi_2O_3 , the exposed surface is

fully covered with a chemisorbed water molecule. The Bi_2O_3 cluster is placed on the GaN (100) surface, followed by the relaxation. At the interface of GaN (100) surface and Bi_2O_3 (010) surface, the Bi bonds with N while the O bonds with Ga. Unlike the bulk-like slab of Bi_2O_3 , 2 water molecules are chemisorbed, which is due to the unsaturated coordination of edge Bi atoms. The surface structure of the water chemisorbed GaN- Bi_2O_3 is presented in Figure 3.12.

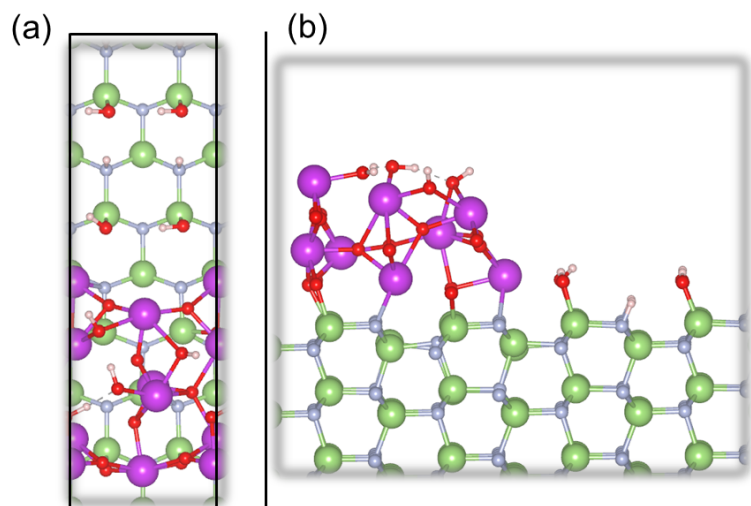


Figure 3.12. (a) Top view image and (b) side view image of the GaN- Bi_2O_3 composite with surface water chemisorption.

3.4.2 CO_2 Reduction on the GaN (100) Surface

Based on the surface termination of the former chapter, the reaction barrier

for the CO₂ reduction on GaN (100) surface was calculated. In the case of GaN, as the surface is fully covered with adsorbates, the reaction is carried out after the desorption of adsorbates. Various sites for each reaction pathway are marked on the surface of GaN in Figure 3.13(a). Among those pathways, the pathway 1 and 2 proceed to formic acid generation while the pathway 3 and 4 are carbon monoxide pathway. The calculated free energy for steps of each reaction pathway is presented in Figure 3.13(b). For all 4 pathways, the potential determining step (PDS) was the desorption step of *OCHO and *COOH. For reaction pathway 1 to 4, the value of reaction barrier was $\mu_1=2.10$ eV, $\mu_2=2.44$ eV, $\mu_3=1.93$ eV and $\mu_4=2.96$ eV respectively. The form of reaction intermediate binding for each pathway is presented in Figure 3.13(c). As the reaction for carbon monoxide and formic acid generation will go through the pathway with the lowest reaction barrier, the practical reaction pathway for each product will be the pathway 1 and 3 respectively. Comparing the reaction barrier of pathway 1 (CO generation) and pathway 3 (HCOOH generation), the value of the carbon monoxide route is slightly lower than that of the formic acid route, which means that the carbon monoxide generation occurs at the lower potential. In fact, according to Figure 3.6, it is possible to figure out that the faradaic efficiency of the carbon monoxide is observed first, rather than formic acid. Still, the difference of the reaction barrier for each product, 0.17 eV, is not significant enough to achieve a strong selectivity toward the single product.

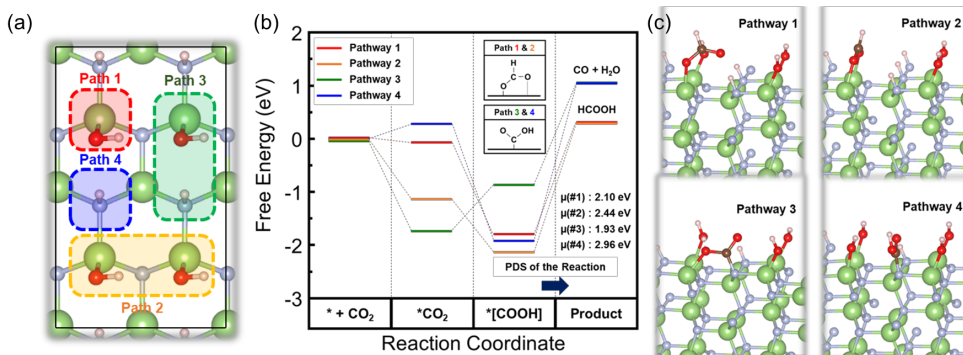


Figure 3.13. (a) Reaction intermediate binding site for each reaction pathway. (b) Potential energy diagram of the carbon monoxide and formic acid generation on the GaN (001) surface. (c) The optimized structure of reaction intermediate binding for each pathway.

3.4.3 CO₂ Reduction on the Bi₂O₃ (010) Surface

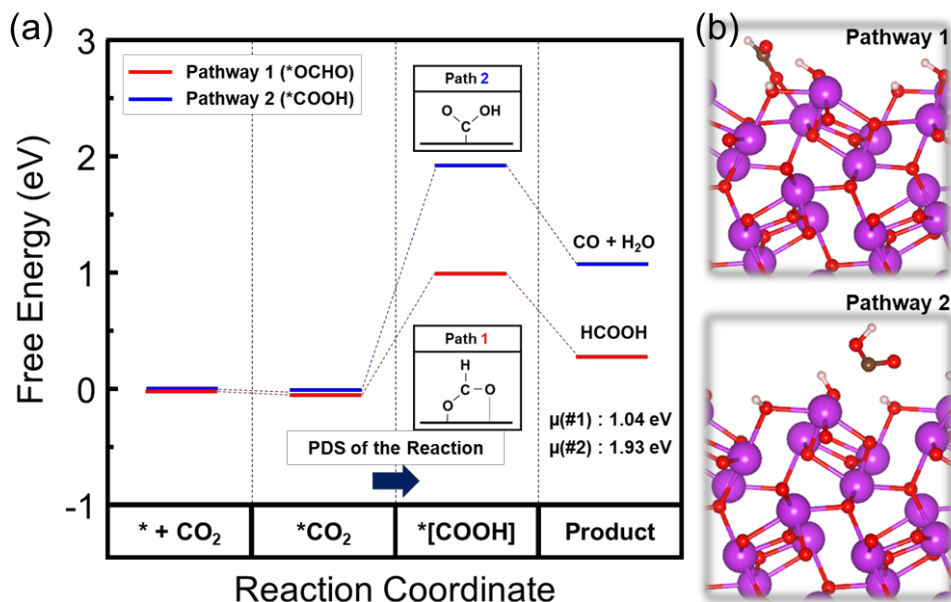


Figure 3.14. (a) Potential energy diagram of the carbon monoxide and formic acid generation on the Bi₂O₃ (010) surface. (b) The optimized structure of reaction intermediate binding for each pathway.

Same as the former chapter, the free energy of reaction steps is calculated for Bi₂O₃ (010) surface. As shown in Figure 3.14(a), for the Bi₂O₃, the PDS of the whole reaction becomes the adsorption step of the reaction intermediate, due to the destabilization of the intermediate state. The destabilization of the intermediate adsorption is assumed to be due to the electronegativity difference of the elements in GaN and Bi₂O₃. The electronegativity difference of Bi (2.02) and O (3.44) is 1.42 while that of Ga (1.81) and N (3.04) is 1.23. With the larger electronegativity difference, the charge transfer between Bi and O is more intense, which let Bi and O become more positive or negative than Ga and N respectively. For *OCHO,

the oxygen binds with metal atoms, extracting the electron, while the carbon bonds with the oxygen of catalyst for *COOH, donating the electron. At the Bi₂O₃, more positive (negative) Bi (O) interact with *OCHO (*COOH) with less charge transfer between reaction intermediate which leads to weaker bonding for both pathways. The scheme of the intermediate bond strength comparison is depicted in Figure 3.15.

With the destabilization of the intermediate step, the reaction barrier value for the carbon monoxide and formic acid pathway is 1.93 eV and 1.04 eV respectively. The structure of intermediate binding is presented in Figure 3.14(b). When compared to that of GaN, the difference in reaction barrier between two pathways is much higher, with the value of 0.89 eV. As the reaction barrier for formic acid generation is significantly lower than carbon monoxide generation, CO₂ reduction on Bi₂O₃ is thermodynamically concentrated on the production of formic acid, with strong selectivity. Thus, through the comparison of reaction barriers for each product, the strong selectivity of the Bi decorated samples in experimental results can be explained.

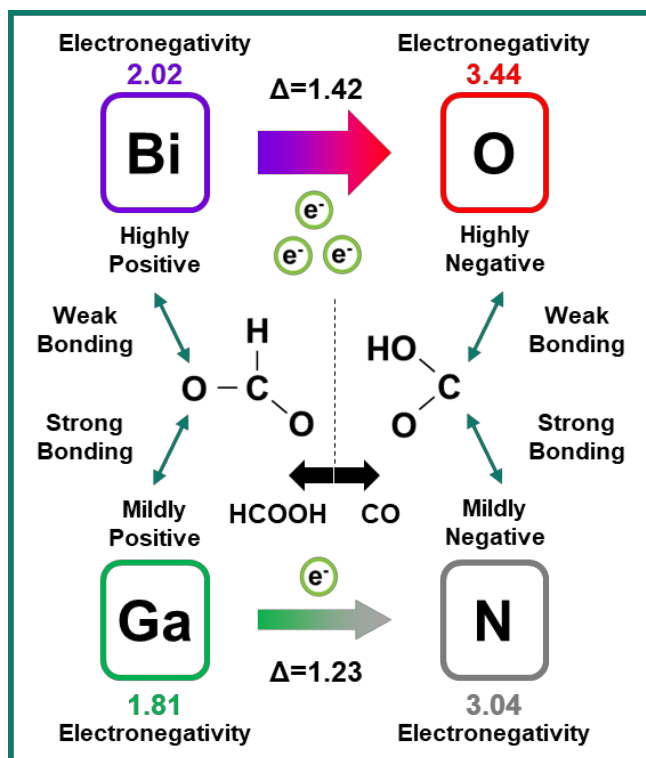


Figure 3.15. Scheme of the reaction intermediate bond strength with GaN or Bi₂O₃

3.4.4 CO₂ Reduction on the GaN-Bi₂O₃ Composite Structure

To understand the mechanism of the enhancement of photocurrent in Bi/GaN NWs/Si sample, the reaction steps on GaN-Bi₂O₃ structure are investigated. In Figure 3.16, a calculated free energy diagram is provided with the surface structure of pathways. The energy level for steps was almost the same as that of the Bi₂O₃ (010) surface, either for reaction barrier values of 1.93 eV (CO generation) and 0.95 eV (HCOOH generation). Only the barrier for formic acid generation decreases slightly from 1.04 eV to 0.95 eV, when compared to Bi₂O₃. Such negligible change may account for the mild increase in faradaic efficiency of Bi/GaN NWs/Si as seen in Figure 3.6. However, it is considered to be not enough to elucidate the mechanism of the noticeable increase of photocurrent.

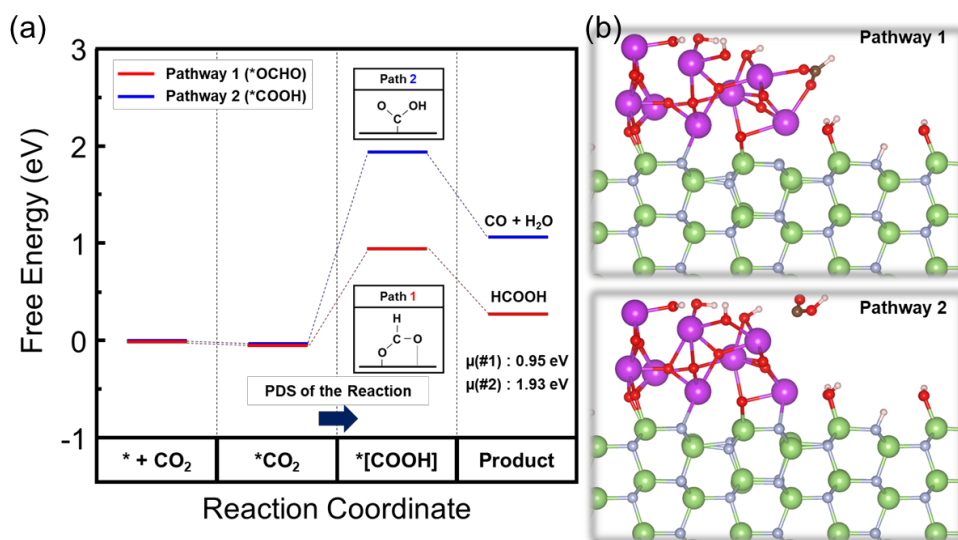


Figure 3.16. (a) Potential energy diagram of the carbon monoxide and formic acid generation on the GaN-Bi₂O₃ composite. (b) The optimized structure of reaction intermediate binding for each pathway.

For further interpretation of the photocurrent enhancement, the electronic structure of the GaN-Bi₂O₃ composite is investigated. In Figure 3.17(a), the density of states (DOS) for GaN slab and GaN-Bi₂O₃ composite are presented. When compared to the DOS of GaN slab, the shift of conduction band toward lower energy level is observed in GaN-Bi₂O₃ composite. To figure out the reason for the conduction band shift, the partial density of states (PDOS) for each element is plotted in Figure 3.17(b). According to the PDOS plot, the conduction band minimum (CBM), which is the shifted part, is mainly composed of the p-orbital of the Bi atoms. This implies that the energy level of the Bi₂O₃ CBM is at a lower position compared to that of GaN.

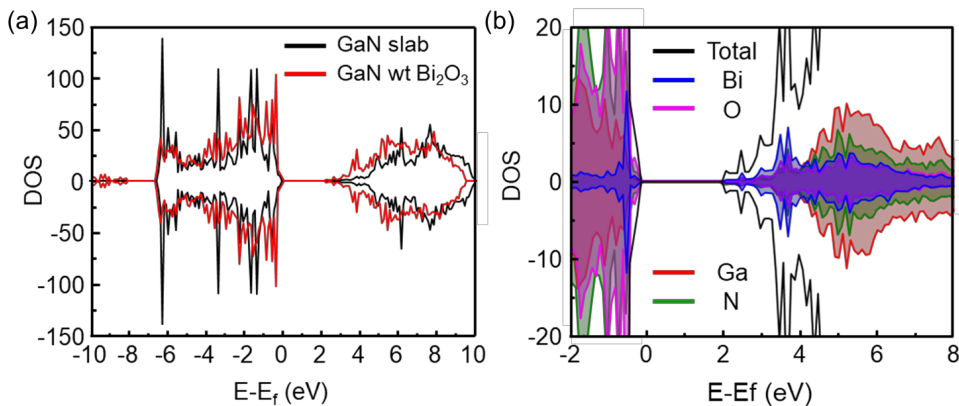


Figure 3.17. (a) Density of states diagram for the GaN slab and GaN with Bi₂O₃. (b) Partial density of states diagram for GaN with Bi₂O₃.

To show the influence of conduction band shift on charge transfer, the band alignment schematic is depicted in Figure 3.18(a). In the figure, shifted conduction band of the Bi_2O_3 is marked with a red line. As the band of Bi_2O_3 resides at a lower energy level than GaN CBM, similar to the junction between Si and GaN, the additional built-in potential for the electron is formed at the interface of GaN and Bi_2O_3 accelerating the charge transfer toward Bi_2O_3 . To confirm the direction of charge transfer, the differential charge density is visualized on the system cell of GaN- Bi_2O_3 in Figure 3.18(b). The region which gained the charge is marked as yellow isosurface, while the loss of charge is colored with sky blue. From the image, the movement of the charge density is concentrated at the interface of GaN and Bi_2O_3 , especially at the side of Bi_2O_3 . It is also can be seen from the 2D plot of the differential charge density and this leads to the conclusion that due to the charge transfer from GaN to Bi_2O_3 , additional charge density is accumulated at the interfacial Bi_2O_3 . The electron transfer between GaN and Bi_2O_3 can have two positive effects. First, as the electron is concentrated in the Bi_2O_3 with highly selective toward the formic acid, the efficiency of the formic acid generation can be improved. Secondly, as the electron is under stronger potential toward the catalyst surface, the photocarrier recombination at the Si decreases. Therefore, based on the electronic structure of the GaN- Bi_2O_3 , it is possible to conclude that the enhancement of photocurrent in Bi/GaN NWs/Si sample is mainly owing to the boosted electron transfer by additional built-in potential from interfacial GaN- Bi_2O_3

heterojunction.

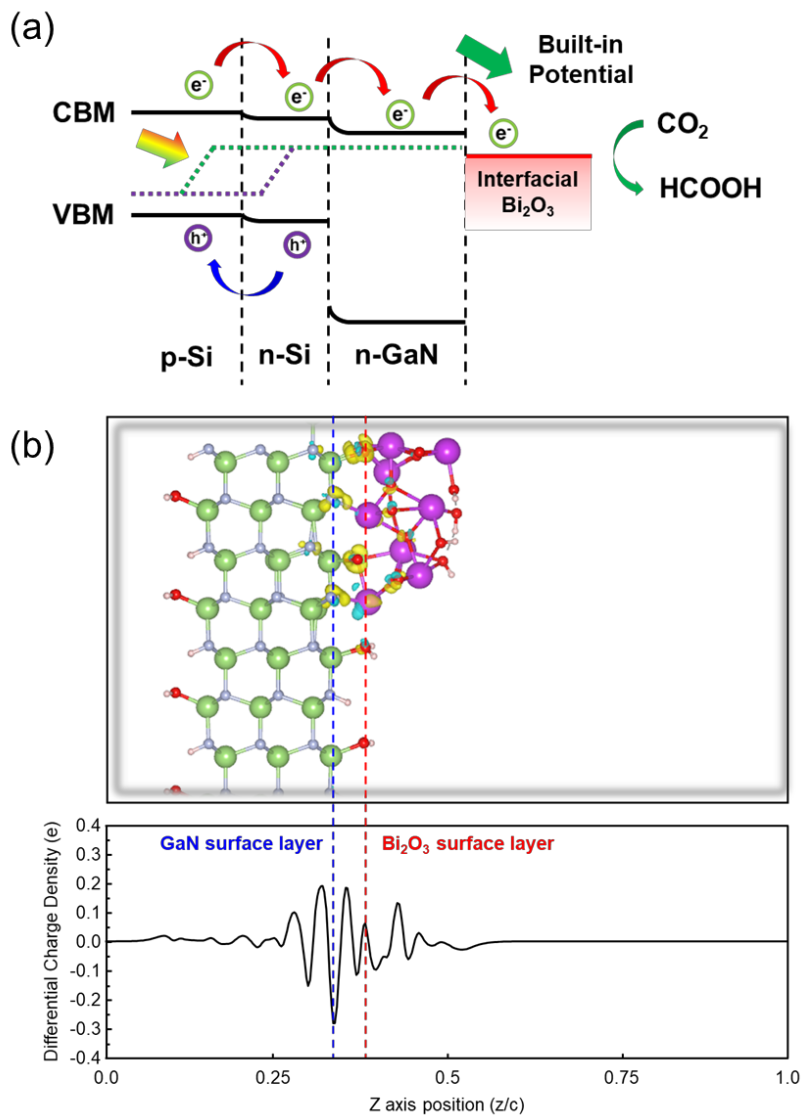


Figure 3.18. (a) Band alignment diagram of Bi₂O₃/GaN NWs/Si based on the calculated GaN-Bi₂O₃ composite density of states. (b) Visualized differential charge density with its linear plot.

3.5 Conclusion

In summary, the mechanism of superior selectivity and photocurrent toward the formic acid achieved from the Bi NPs decoration on GaN NWs was explained through a theoretical approach. According to the experimental results, it is confirmed that the usage of Bi catalyst provides the strong selectivity for the formic acid and the formation of Bi/GaN NWs/Si structure can generate remarkable photocurrent compared to individual catalysts. To understand such improvement, thermodynamic reaction barriers and electronic structure were investigated for various catalyst models, represented as GaN, Bi₂O₃, and GaN-Bi₂O₃ composite. The reaction barrier difference between the carbon monoxide pathway and the formic acid pathway was more significant in Bi₂O₃ rather than GaN, indicating that Bi₂O₃ has strong selectivity toward the formic acid generation reaction due to low reaction barrier. For the GaN-Bi₂O₃ composite, it is figured out that the decorated Bi₂O₃ leads to the shift of conduction band at the GaN-Bi₂O₃ interface, which provides the additional built-in potential for photo-generated electrons. As a result, with the enhanced electron transfer kinetics, the decrease of photocarrier recombination contributes to the increase of the photocurrent for the formic acid generation. From the methodology of interpretation on the mechanism of the selectivity acquisition with Bi decoration and synergetic effect between GaN-Bi₂O₃, we expect further understandings about CO₂ reduction

reactions on various catalyst materials through theoretical approaches.

3.6 References

- [1] Intergovernmental Panel on Climate Change. Climate Change 2014: *Synthesis Report*, **2014**
- [2] Intergovernmental Panel on Climate Change. IPCC Special Report on the Impacts of Global Warming of 1.5 °C-Summary for Policy Makers, Incheon, **2018**
- [3] S. Nitopi, E. Bertheussen, S. B. Scott, X. Liu, A. K. Engstfeld, S. Horch, B. Seger, I. E. L. Stephens, K. Chan, C. Hahn, J. K. Norskov, T. F. Jaramillo, I. Chorkendoff, Progress and Perspectives of Electrochemical CO₂ Reduction on Copper in Aqueous Electrolyte. *Chem. Rev.* **2019**, 119, 7610-7672
- [4] M. Grodzicki, P. Mazur, S. Zuber, J. Brona, A. Ciszewski, Oxidation of GaN(0001) by low-energy ion bombardment. *Appl. Surf. Sci.* **2014**, 304, 20-23
- [5] S. Kizir, A. Haider, N. Biyikli, Substrate impact on the low-temperature growth of GaN thin films by plasma-assisted atomic layer deposition. *J. Vac. Sci. Technol. A* **2015**, 34, 041511
- [6] M. Grodzicki, J.-G. Rousset, P. Ciechanowicz, E. Piskorska-Hommel, D. Hommel, XPS studies on the role of arsenic incorporated into GaN. *Vacuum* **2019**, 167, 73-76
- [7] X. Li, Y. Sun, T. Xiong, G. Jiang, Y. Zhang, Z. Wu, F. Dong, Activation of amorphous bismuth oxide via plasmonic Bi metal for efficient visible-

light photocatalysis. *J. Catal.* **2017**, 352, 102-112

[8] M. Mishra, T. C. S. Krishna, N. Aggarwal, M. Kaur, S. Singh, G. Gupta, Pit assisted oxygen chemisorption on GaN surfaces. *Phys. Chem. Chem. Phys.* **2015**, 17, 15201

[9] S. Singh, R. K. Sahoo, N. M. Shinde, J. M. Yun, R. S. Mane, W. Chung, K. H. Kim, Asymmetric faradaic assembly of Bi₂O₃ and MnO₂ for a high-performance hybrid electrochemical energy storage device. *RSC Adv.* **2019**, 9, 32154

[10] G. Zeng, T. A. Pham, S. Vanka, G. Liu, C. Song, J. K. Cooper, Z. Mi, T. Ogitsu, F. M. Toma, Development of a photoelectrochemically self-improving Si/GaN photocathode for efficient and durable H₂ production. *Nat. Mater.* **2021**

[11] M. G. Kibria, S. Zhao, F. A. Chowdhury, Q. Wang, H. P. T. Nguyen, M. L. Trudeau, H. Guo, Z. Mi, Tuning the surface Fermi level on p-type gallium nitride nanowires for efficient overall water splitting. *Nat. Commun.* **2014**, 5, 3825

[12] G. Kresse, J. Furthmuller, Efficiency of Ab-Initio Total Energy Calculations for Metals and Semiconductors Using a Plane-Wave Basis Set. *Comput. Mater. Sci.* **1996**, 6, 15-50

[13] G. Kresse, J. Furthmuller, Efficient Iterative Schemes for Ab Initio Total-energy Calculations Using a Plane-Wave Basis Set. *Phys. Rev. B: Condens. Matter Mater. Phys.* **1996**, 54, 11169-11186

[14] P. Hohenberg, W. Kohn, Inhomogeneous Electron Gas. *Phys. Rev.*

1964, 136, B864-B871

[15] W. Kohn, L. J. Sham, Self-Consistent Equations Including Exchange and Correlation Effects. *Phys. Rev.* **1965**, 140, A1133-A1138

[16] F. Han, Projector-Augmented Plane-Wave Method. *Probl. Solid State Phy. with Solut.* **2011**, 50, 391-396

[17] G. Kresse, D. Joubert, From Ultrasoft Pseudopotentials to the Projector Augmented-Wave Method. *Phys. Rev. B: Condens. Matter Mater. Phys.* **1999**, 59, 1758

[18] Y.-H. Lei, Z.-X. Chen, Density functional study of the stability of various α -Bi₂O₃ surfaces. *J. Chem. Phys.* **2013**, 138, 054703

Chapter 4.

Theoretical Analysis on the Mechanism for improved Selectivity of the Precious Metal Decorated MoS₂ Gas Sensor

4.1 Introduction

In recent days, managing the quality of the air becomes essential for a better human life. Because detrimental gases and air pollutants such as fine dust, CO, SO₂, and CO₂ causes respiratory diseases, sensor device with high sensibility is extensively required for the human health.^[1-3] Not only for the health problem but also the air quality monitoring becomes necessary for the next-generation electronics due to the recent progress in the Internet of Things (IoT) interconnected devices.^[4] For the versatile application of the gas sensor, it is essential to fabricate the electronic nose, which can detect various types of gases.

Chemoresistive gas sensors based on semiconductor materials are considered promising candidates for application as a base material of electronic nose due to their facile fabrication processes, small sizes, low costs, and easy integration into integrated circuits. Especially the 2D semiconductor material, MoS₂, is gaining extensive attention due to its high surface-to-volume ratio and electrochemically active edge site.^[5, 6] However, due to the high portion of the inert planar regions, the sensitivity of the MoS₂ still far from the application. Furthermore, the individual MoS₂ cannot obtain sensitivity toward multiple gases.

As the approach toward highly sensitive sensor fabrication, the decoration of the noble metal elements is a well-known method. With the addition of noble metal elements, the electronic structure of the material can be

manipulated and it affects the sensitivity of the sensor material. Moreover, by changing the noble metal element for decoration, selectivity for various gases can be also acquired. With the array of single sensors with high selectivity and sensitivity, the electronic nose can be fabricated.

Herein, in this study, experimental results of the noble metal nanoparticle (NP) decorated MoS₂ gas sensor will be presented. Based on the response toward various gases, the sensitivity and selectivity of each noble metal decoration are discussed. TEM and XPS characterization were carried out for the system modeling in the simulation part. The whole experimental measurement and characterization were performed by S. Y. Park and T. H. Kim. Based on the experiment, the change in sensitivity and selectivity along with various noble metal decorations on MoS₂ will be explained through the first-principles calculations result.

4.2 Experimental Results

4.2.1 Fabrication of the Noble Metal NP Decorated MoS₂

As the base material, the layered MoS₂ powder (~90 nm powder, 99% purity, 5g; Graphene supermarket) is used. As the precursor of noble metals for decoration, gold chloride monohydrate (HAuCl₄·H₂O), potassium tetrachloropalladate (K₂PdCl₄), and Potassium tetrachloroplatinate (K₂PtCl₄) were selected. The principle for the noble metal decoration is presented as a schematic in Figure 4.1. Due to the lower reduction potential of the noble metal chloride ions compared to the work function of MoS₂, the redox reaction spontaneously occurs when the MoS₂ and the noble metal salt are mixed in Distilled water, After the decoration of noble metals, each solution is centrifuged with deionized water with 13500 rpm for 10 min to remove the residual metal salts.

For the sensor fabrication with the synthesized noble metal decorated MoS₂, the final solution is dispersed in 1 ml of DI water. Then the diluted solution was drop cast on the interdigitated electrode (IDE) with the amount of 0.5 μl followed by drying for 30 min at 100 °C. Fabricated sensors are heat-treated at 500 °C under the Ar ambient condition by Rapid Thermal Annealing (RTA) to crystallize the noble metal NPs.

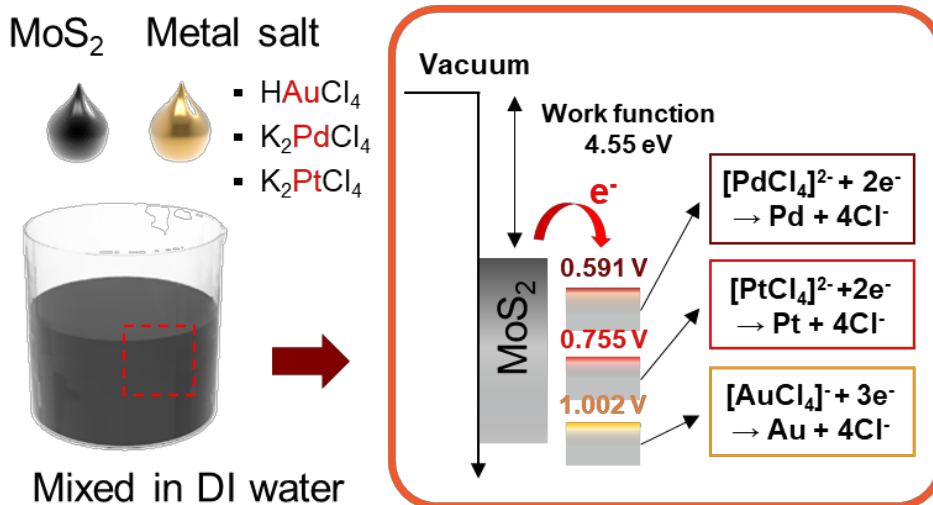


Figure 4.1. Schematic illustration of the noble metal decorated MoS₂ synthesis and energy diagram showing the work function of MoS₂ with reduction potential of each noble metal.

4.2.2 Characterization of the Noble Metal NP Decorated MoS₂

For the reasonable modeling for the simulation in the following chapter, the crystal structure, surface bond state, and particle size of decorated noble metal NPs are investigated through various characterizations. In Figure 4.2, the high magnification image of the MoS₂ and decorated noble NPs are presented. From the diffraction pattern achieved from the Fast Fourier Transform (FFT) of images, the crystal structure of each material is confirmed as MoS₂ (P6₃/mmc, PDF No. 00-037-1492), Au (Fm-3m, PDF No. 00-004-0784), Pd (Fm-3m, PDF No. 00-046-1043), and Pt (Fm-3m, PDF No. 00-004-0802). To check the size and distribution of noble metal NPs, low magnification images and scanning transmission electron microscopy images are provided in Figure 4.3. From the TEM images, the size of noble metal particles was observed as 20~30 nm for palladium and 2~4 nm for platinum and gold. In addition to particle size, for platinum, the agglomeration of particles was identified. The distribution of noble metal NPs was able to be seen from STEM images. Mostly decorated particles are located along the edge of MoS₂.

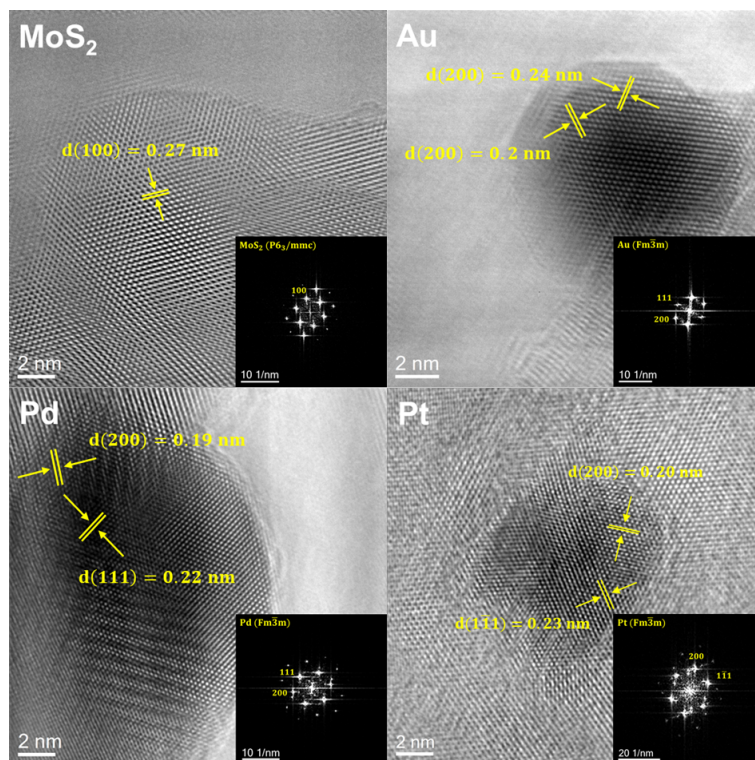


Figure 4.2. HRTEM images of MoS₂ and synthesized noble metal particles with the diffraction pattern acquired from FFT.

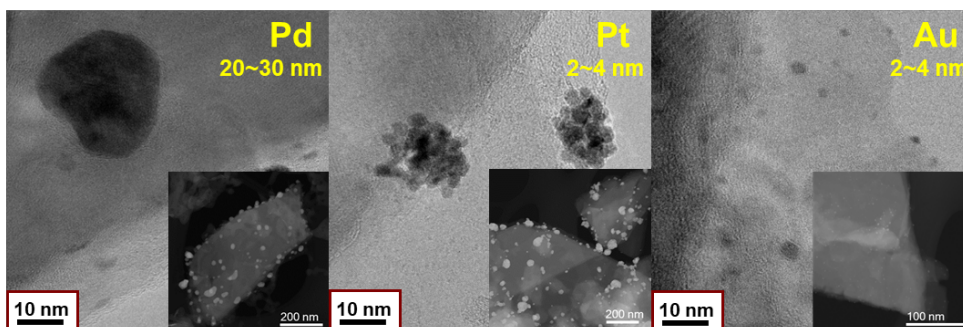


Figure 4.3. Low magnification TEM images and STEM images of decorated noble metal particles.

The surface chemical bonding state of the decorated noble metal NP was

investigated X-ray photoelectron spectroscopy (XPS). According to the XPS spectra of Au 4f, only the peak of Au (83.6 eV, 87.2 eV) was detected, which indicates the absence of surface adsorbates or oxidation.^[7] On the other hand, from the XPS spectra of Pd 3d, along with the Pd metal peak (335.2 eV, 340.5 eV), PdO peaks (336.6 eV, 342.0 eV) were also deconvoluted.^[8] Similar to Pd, Pt 4f spectra either has both Pt peaks (71.3 eV, 74.6 eV), and PtO (72.8 eV, 76.1 eV) peaks.^[9] The presence of the mild PdO, and PtO peaks indicates that the surface of both NPs are oxidized while the inner region remains as a metallic state.^[10]

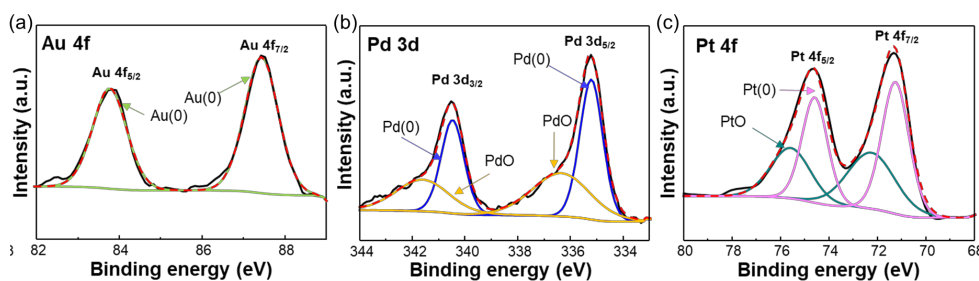


Figure 4.4. XPS spectra of the (a) Au-decorated MoS₂, (b) Pd-decorated MoS₂, and (c) Pt-decorated MoS₂ samples.

4.2.3 Gas Sensing Properties of the Noble Metal NP

Decorated MoS₂

To identify the sensitivity and selectivity of the samples toward various gases, the response value was presented in Figure 4.5 based on the resistance change of the sample during the target gas flow. 6 gases, hydrogen (H₂), ammonia (NH₃), ethanol (C₂H₅OH), nitrogen dioxide (NO₂), hydrogen sulfide (H₂S), and acetone (CH₃COCH₃), are tested to check the response. Four consecutive pulses are acquired with a flow of 50 ppm for NH₃, H₂, C₂H₅OH, CH₃COCH₃, and 5 ppm for NO₂, H₂S. According to the response curve of the pristine MoS₂, a strong response of 651.53% is observed toward NH₃ while the response for other gases is less than 100%. When the Au is decorated on the MoS₂, the remarkable decrease of NH₃ response is detected while the C₂H₅OH response slightly increases. The Pd-decorated MoS₂ shows the superior response toward H₂, simultaneously losing the sensitivity toward NH₃. The Pt-decorated MoS₂ gives a similar tendency with Pd decoration, an increase of H₂ response and decrease of NH₃ response, but the amount of H₂ response increase is much smaller than that of Pd. The exact response values are presented in Table 4.1. As a result of comparing the response curves of each sample, when the pristine MoS₂ was decorated with the noble metal, the types of gases whose response value mainly changed were H₂ and NH₃ while other changes of other gases were mild. The response change value with noble metal decoration for two gases was provided in Table 4.2.

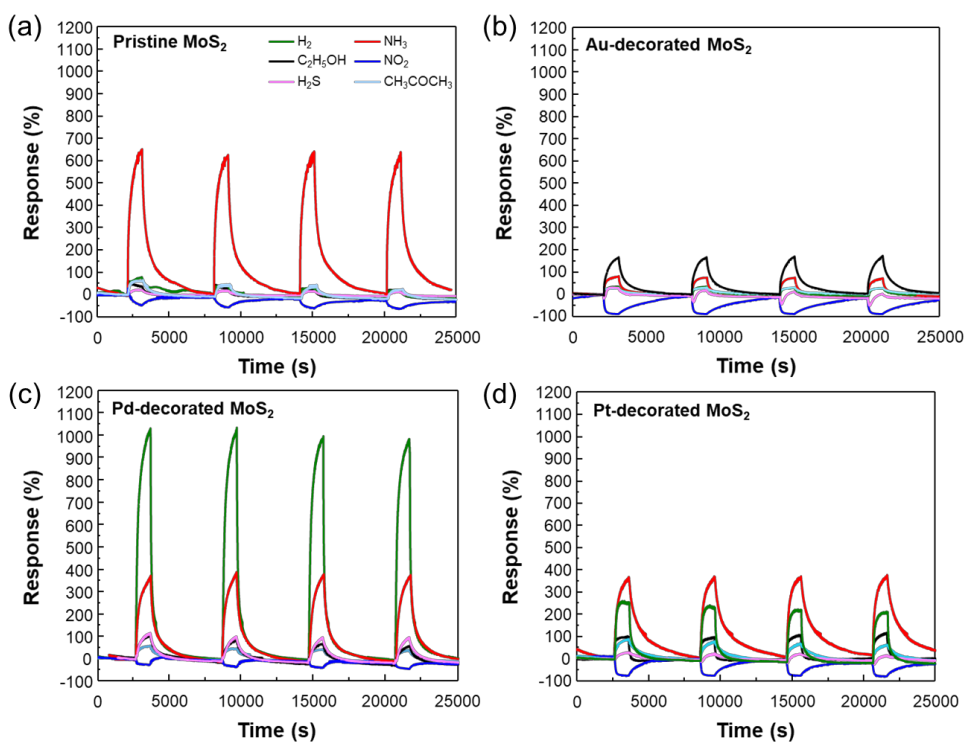


Figure 4.5. The response curves of (a) pristine MoS₂, (b) Au-decorated MoS₂, (c) Pd-decorated MoS₂, and (d) Pt-decorated MoS₂.

H ₂	NH ₃	C ₂ H ₅ OH	NO ₂	H ₂ S	CH ₃ COCH ₃
----------------	-----------------	----------------------------------	-----------------	------------------	-----------------------------------

MoS₂	77.33 %	651.53 %	40.02 %	46.64 %	23.05 %	63.46 %
Au	36.86 %	80.37%	165.28 %	87.0 %	32.71 %	29.35 %
Pd	1027.1 %	371.69 %	102.62 %	26.92 %	113.79 %	58.32 %
Pt	256.5 %	366.71 %	101.41 %	77.38 %	27.8 %	89.48 %

Table 4.1. Response values for various gases measured from pristine MoS₂ and noble metal decorated MoS₂ gas sensors

	Response Change for H₂ (%)	Response Change for NH₃ (%)
Pd	77.33 → 1027.1 (947.77)	651.53 → 371.69 (-279.84)
Pt	77.33 → 256.5 (179.17)	651.53 → 366.71 (-284.82)
Au	77.33 → 36.86 (-40.47)	651.53 → 80.37 (-571.16)

Table 4.2. H₂ and NH₃ gas response change in noble metal decorated MoS₂ sensors when compared to the pristine MoS₂ sensor. The amount of response change is presented in brackets.

In order to check the selectivity of pristine and noble metal decorated

MoS₂ samples, the response for various gases is represented as a polar plot, as shown in Figure 4.6. The pristine MoS₂ sensor shows strong selectivity toward NH₃ with its high sensitivity. For the Au-decorated MoS₂, the Au decoration stiffly decreases the NH₃ sensitivity, which leads to C₂H₅OH selectivity. As mentioned before, Pd and Pt decoration show similar response change tendency of NH₃ response decrease and H₂ response increase. However, the degree of H₂ response increase is much larger with Pd decoration, the Pd-decorated MoS₂ could obtain strong selectivity for H₂ gas while Pt-decorated MoS₂ shows poor selectivity to a single type of gas.

From the gas sensor properties, we could realize that the sensitivity change with the noble metal decoration is mainly observed for H₂ and NH₃ gas, and the mechanism of selectivity acquisition also depends on the sensing behavior of H₂ and NH₃. Therefore, in the following chapter, the simulation on the gas sensing behavior of pristine and noble metal decorated MoS₂ sensors will be primarily focused on H₂ and NH₃ gas.

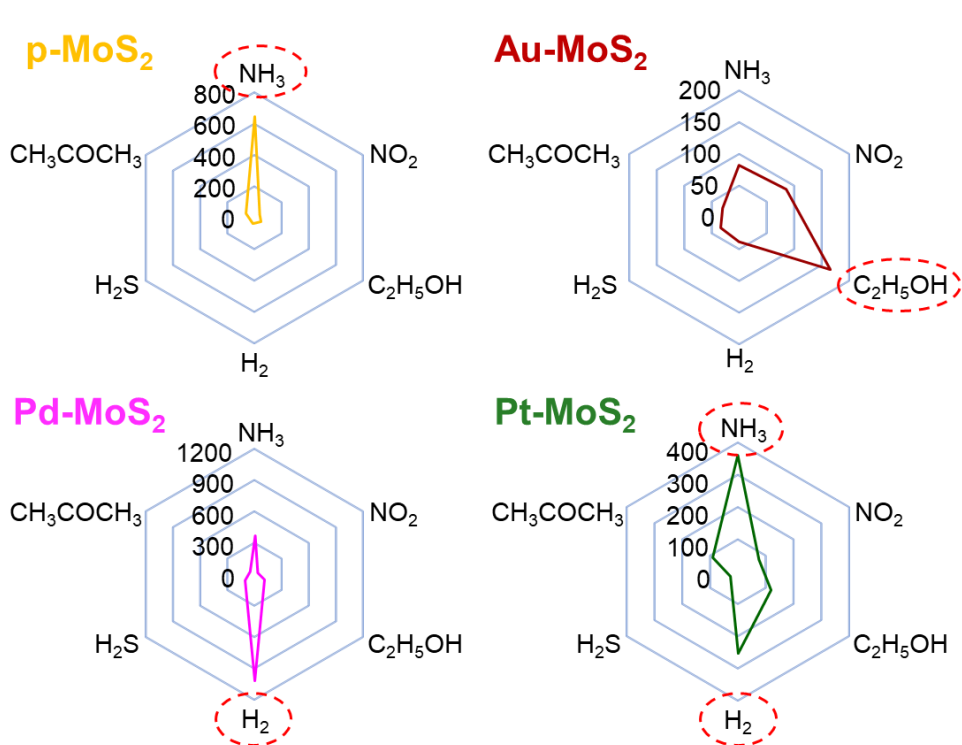


Figure 4.6. Polar plot of response values acquired from pristine MoS₂ and noble metal decorated MoS₂ sensors.

4.3 Theoretical Approach

4.3.1 Computational Details

The first-principles calculations in this study were performed using the projected augmented wave (PAW) method and Perdew-Burke-Ernzerhof (PBE) generalized gradient approximation (GGA) exchange-correlation functional with the Vienna Ab initio Simulation Package (VASP).^[11-13] For the vacuum slab cell, dipole correction in direction of the c-axis is employed to correct the influence of the asymmetric layer arrangement. To properly apply the Van der Waals interaction of gas molecules, the DFT-D3 method by Grimme and co-workers was included.^[14-16] An energy cutoff of 400 eV and electronic step convergence cutoff of 10^{-5} eV were used for the electronic relaxation of the system. For the ionic relaxation, the geometry of atoms was relaxed until the Hellman-Feynman forces were below 0.01 eV/Å.

4.3.2 Details on System Modeling

In this chapter, to investigate the gas adsorption behavior of various samples with different morphology, size, and surface termination, distinct models for each case are constructed. For the pristine MoS₂, MoS₂ with exposed basal plane and edge were modeled. The MoS₂ basal plane is composed of monolayer MoS₂, with 25 Mo atoms and 50 S atoms, relaxed with the Gamma-centered k-point grid of 2x2x1. In the case of the MoS₂ edge model, the thickness of the slab was 6 unit cell layers along the direction of (100). The k-points sampling of the 8x2x1 Monkhorst grid is applied for relaxation. To mimic the bulk-like property of the inner layer, only 3 layers at the edge for gas adsorption were fully relaxed, while the other 3 layers are fixed. To determine the edge termination of MoS₂, the edge energy (E_{edge}) of various terminations with a different number of edge sulfur atoms was calculated as below.

$$E_{edge} = E_{term} - nE_{bulk} - k\mu_S$$

E_{term} denotes the energy of the MoS₂ edge slab with sulfur termination. E_{bulk} is the energy of bulk MoS₂ unit cell and n is the number of MoS₂ unit cells in the MoS₂ edge slab. μ_S is the chemical potential of the sulfur atom and k is the number of additional sulfur atoms in the MoS₂ edge slab when compared to the stoichiometric state. The chemical potential of the sulfur is calculated from the energy of hydrogen sulfide, as the sulfurization of Mo for MoS₂ synthesis is carried out under the flow of hydrogen sulfide. The formula for sulfur chemical potential is presented as below.

$$\mu_S = E_{H_2S} - E_{H_2}$$

For the modeling for bulk-like metal surface, the slab with the thickness of 6 unit cell layers to the direction of (111) is fabricated, as the (111) surface is known to be the most stable facet for noble metals with face-centered cubic (FCC) structure. Same as MoS₂, only the surface 3 layers are relaxed with the 4x4x1 Monkhorst k-points grid. The structure of surface oxidation for noble metal particles is determined based on the adsorption energy of oxygen. The adsorption energy (E_{ads}) is calculated as below.

$$E_{ads} = E_{term} - E_{slab} - \frac{n}{2} E_{O_2}$$

Each E_{term} and E_{slab} means the energy of slab cell with and without surface oxygen. E_{O_2} is the DFT energy of the oxygen gas molecule and n is the number of oxygen atoms at the metal surface.

Nanoparticles of noble metal with quantum dot size are modeled as the nanocone cluster. With the shape of a tetrahedron, all 4 exposed surface has the (111) facet, same as the bulk-like metal slab. Nanocones are placed in the cubic vacuum cell with the size of 25 Å x 25 Å x 25 Å, large enough to ignore the interaction between periodically repeated cells. The nanocone cluster is composed of 20 metal atoms and all atoms are fully relaxed with the 2x2x2 Monkhorst k-points grid. Surface oxidation is also considered for the nanocone cluster model based on the surface oxygen adsorption energy, as done in the bulk-like slab model.

4.3.3 Details on the Binding Energy Calculation of Gas Molecules

For the comparison with the experimental response value of H₂ and NH₃, the binding energy (E_{bind}) was calculated with the equation below.

$$E_{\text{bind}} = -[E_{\text{ads}} - E_{\text{slab}} - E_{\text{gas}} + \Delta\text{ZPE}]$$

The energy of the slab/cluster with adsorbed gas molecule is stated as E_{ads} , while E_{slab} denotes the slab/cluster without gas adsorption. E_{gas} is the DFT energy of the gas molecule and ΔZPE is the difference of the ZPE of the gas molecule for the adsorbed state (ZPE_{ads}) and isolated state (ZPE_{iso}), expressed in the following equation

$$\Delta\text{ZPE} = \text{ZPE}_{\text{ads}} - \text{ZPE}_{\text{iso}}$$

The values of the DFT energy and ZPE for each gas are presented in Table 4.3 and Table 4.4.

H ₂	NH ₃
----------------	-----------------

E_{DFT} (eV)	-6.77	-19.54
ZPE (eV)	0.35	0.91

Table 4.3. Calculated DFT energy and zero-point energy of H₂ and NH₃ gas molecule.

	H₂	NH₃
MoS₂ basal plane	0.35 eV	0.91 eV
MoS₂ edge	0.28 eV	0.91 eV
Bulk-like Au	0.27 eV	0.96 eV
Bulk-like Pd	0.57 eV	0.94 eV
Bulk-like Pt	0.59 eV	0.90 eV
Au cluster	0.28 eV	0.97 eV
Pt cluster	0.62 eV	0.93 eV

Table 4.4. Calculated zero-point energy of adsorbed H₂ and NH₃ gas molecule on MoS₂ and noble metal surface.

4.4 Result and Discussion

4.4.1 Gas Adsorption on the Pristine MoS₂

To understand the sensitivity of pristine MoS₂ toward H₂ and NH₃, the binding energy on the MoS₂ basal plane was first investigated. Both NH₃ and H₂ gas molecule binds with the MoS₂ basal plane through Van der Waals force which is shown from the binding structure of Figure 4.7. As the atoms of the MoS₂ basal plane are inert, the binding energy for NH₃ and H₂ has a small value of 0.08 eV and 0.06 eV respectively. According to the experimental response values in Figure 4.5, the pristine MoS₂ shows higher sensitivity toward NH₃, which does not match with the binding energy on the MoS₂ basal plane. Thus, we can conclude that the basal plane is not a major binding site for gas molecules.

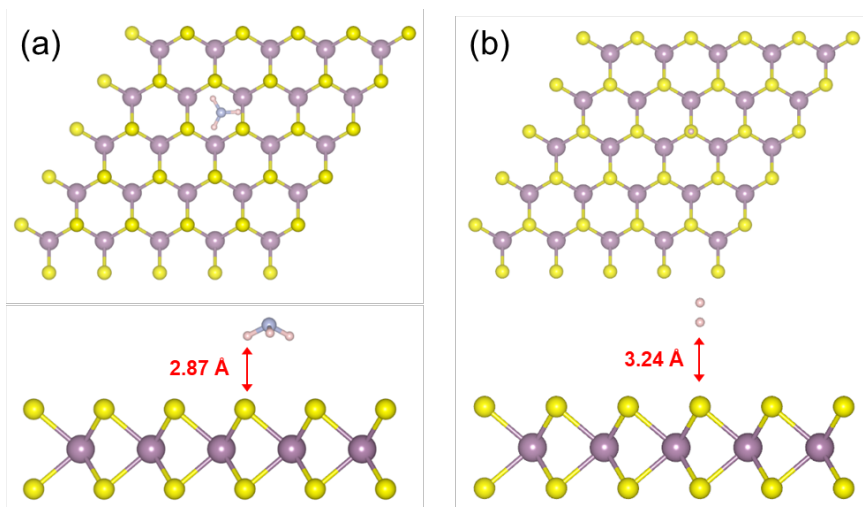


Figure 4.7. Adsorption site of the (a) NH₃ molecule and (b) H₂ molecule on the MoS₂ basal plane.

The edge site of the MoS₂ has long been reported as the reactive site when compared to the basal plane. For the investigation of the gas adsorption at the MoS₂ edge site, the edge site termination is determined based on the edge energy. As shown in Figure 4.8(a), the MoS₂ has 2 types of edge, named Mo-edge and S-edge. The termination of the edge site varies with the number of sulfur atoms and thermodynamically the most stable edge structure is confirmed through edge energy calculation, which is explained in chapter 4.3.2. First, the shape and the edge energy of the Mo-edge are presented in Figure 4.8(b). With the lowest edge energy of 8.51 eV, the termination with 1 sulfur atom is determined as the most stable structure. With the 1S Mo-edge, the edge energy of the S-edge with the various number of sulfur atoms is investigated in Figure 4.8(c). For S-edge, the termination with 2 sulfur atoms has the lowest edge energy and is adopted as the edge structure for the gas molecule adsorption.

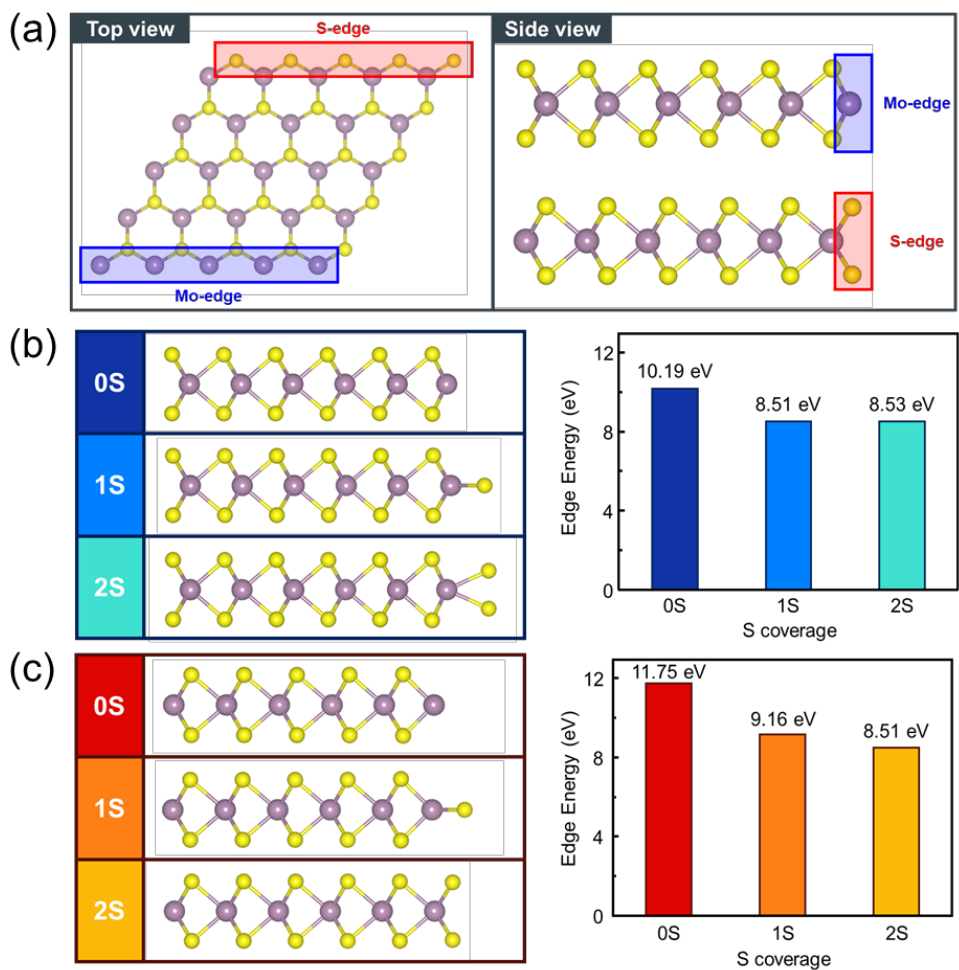


Figure 4.8. (a) Top and side view of the pristine MoS₂. Edge energy of (b) Mo-edge and (c) S-edge with various number of sulfur atoms.

Based on the MoS₂ edge model with the most stable edge termination

structure in Figure 4.9(a), the binding energy of the NH_3 and H_2 gas molecules are calculated as 0.54 eV and 0.15 eV respectively. According to Figure 4.9(b), it is possible to notice that the binding energy increased at the edge site for both gas molecules when compared to the binding at the basal plane. Furthermore, the binding energy of the NH_3 is more than 3 times larger than that of H_2 , which explains the high NH_3 gas selectivity of pristine MoS_2 from experimental results. Therefore, we could conclude that the MoS_2 edge site is the major binding site for gas molecules and the strong binding of NH_3 gas at the MoS_2 edge leads to the excellent selectivity toward NH_3 gas of pristine MoS_2 sensor.

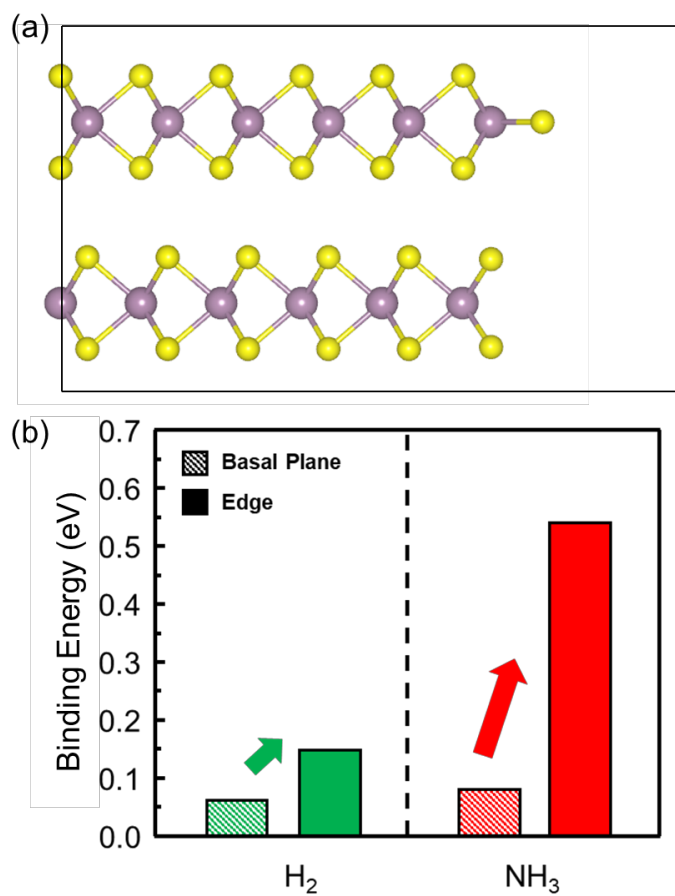


Figure 4.9. (a) The structure of MoS₂ edge model with the most stable edge termination. (b) H₂ and NH₃ molecule binding energy at MoS₂ basal plane and edge site.

4.4.2 Gas Adsorption on the Bulk-like Noble Metal slab

Model

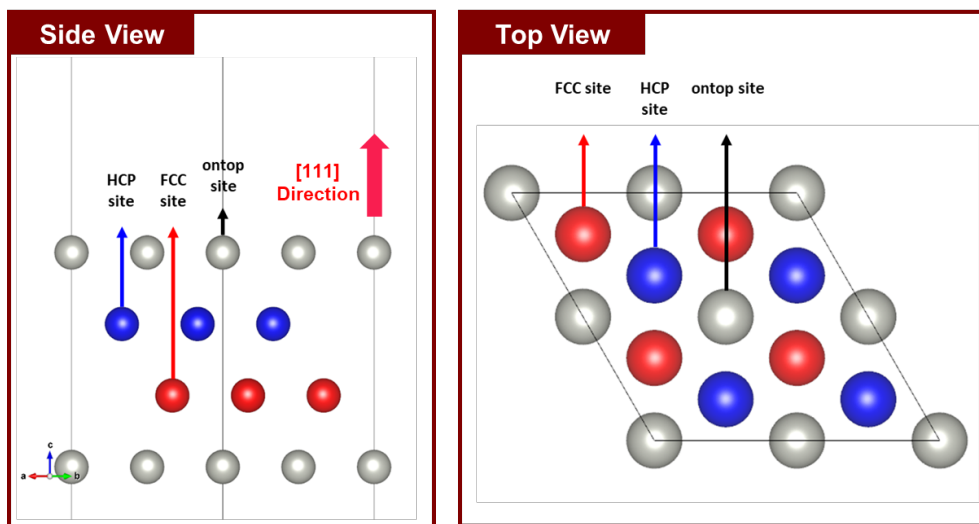


Figure 4.10. Side and top view of the bulk-like noble metal slab with (111) surface. Inequivalent oxygen adsorption sites of FCC, HCP and ontop sites are colored with red, blue and silver.

In order to investigate the noble metal decoration effect on gas sensing properties, each noble metal NP is modeled as a bulk-like vacuum slab. As seen in the XPS spectra in Figure 4.4, surface oxidation is observed for Pd and Pt NPs. From chapter 4.3.2, the surface oxidized metal slab is modeled based on the oxygen adsorption energy. For the (111) surface of FCC metal, there are 3 inequivalent sites for oxygen adsorption, as represented in Figure 4.10. The oxygen adsorption energy on the ontop, FCC, and HCP site for Pd and Pd surface is provided in Figure 4.11(a). Both for Pd and Pt surface, the FCC site was the most favorable site for oxygen adsorption. The coverage of the oxygen adsorption on the FCC site is also investigated by calculating the adsorption energy. According to Figure 4.11(b), either Pd and Pt

surfaces have the lowest adsorption energy of -3.007 eV and -2.802 eV for the coverage of 75 %. The top view image of the metal slab model for various oxygen coverages is presented in Figure 4.12. The structure of the surface oxidized bulk-like slab of Pd, Pt, and metallic Au bulk-like slab with a metallic surface, which were used for H₂ and NH₃ gas adsorption, are presented in Figure 4.13.

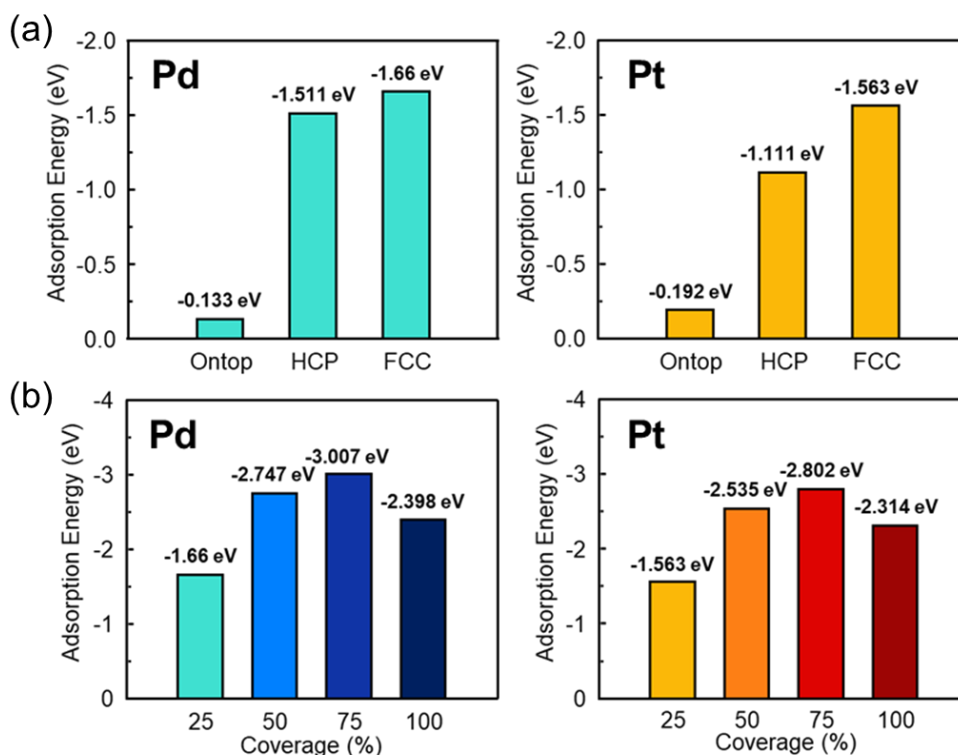


Figure 4.11. (a) Oxygen adsorption energy on various sites of Pd and Pt (111) surface slab. (b) Oxygen adsorption energy on FCC site of Pd and Pt (111) surface slab with variety of coverages.

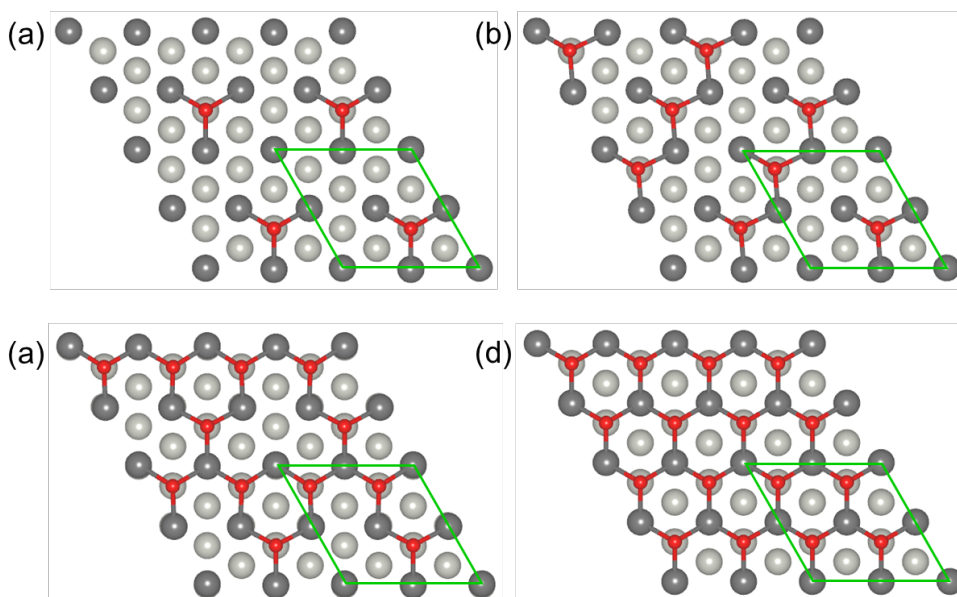


Figure 4.12. Top view of the bulk-like metal slab for various oxygen coverage, respectively (a) 25 %, (b) 50 %, (c) 75 %, and (d) 100 %. The metal atoms at the outermost layer are colored with dark gray while the other metal atoms are light gray and oxygen atoms are red. The unit cell used for calculation is marked with green line.

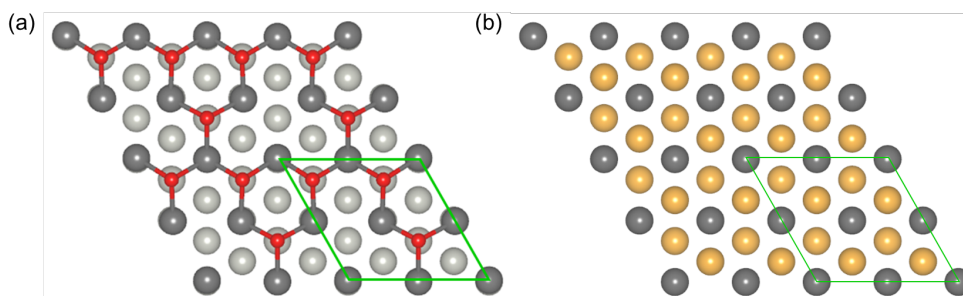


Figure 4.13. Top view of the surface structure of (a) Pd and Pt bulk-like slab and (b) Au bulk-like slab which used for the gas molecule binding energy calculation. The outermost metal atoms are colored with dark grey and oxygen atoms are colored with red.

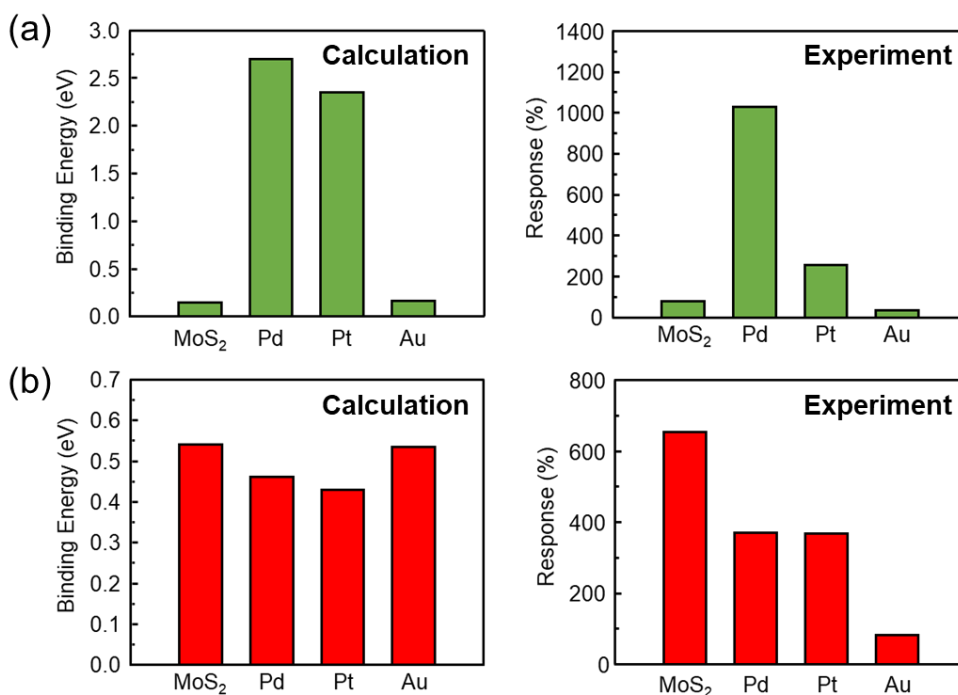


Figure 4.14. Comparison of calculated binding energy from bulk like noble metal slab and experimental response value for (a) H₂ gas and (b) NH₃ gas.

Based on the constructed surface structure, the binding energy of the H₂ and NH₃ is calculated. For H₂ gas molecule, the binding energy of 2.47 eV, 2.34 eV, and 0.16 eV was acquired while the NH₃ binding energy has the value of 0.46 eV, 0.43 eV, and 0.53 eV on Pd, Pt, and Au bulk-like slab. The trend of binding energy value and experimental response is presented in Figure 4.14. The H₂ binding energy is extremely increased for the Pd and Pt bulk-like slab, which somehow matches with experimental data. The strong binding of the H₂ on the Pd and Pt slab is due to the surface oxygen, which becomes the highly reactive site for hydrogen chemisorption as shown in Figure 4.15. For all noble metal slabs, the binding energy of NH₃ gas decreased when compared to the pristine MoS₂ edge. Though, the trend of

the binding energy did not match well with that of experimental response values. The structure of NH_3 binding for each noble metal slabs can be seen in Figure 4.15.

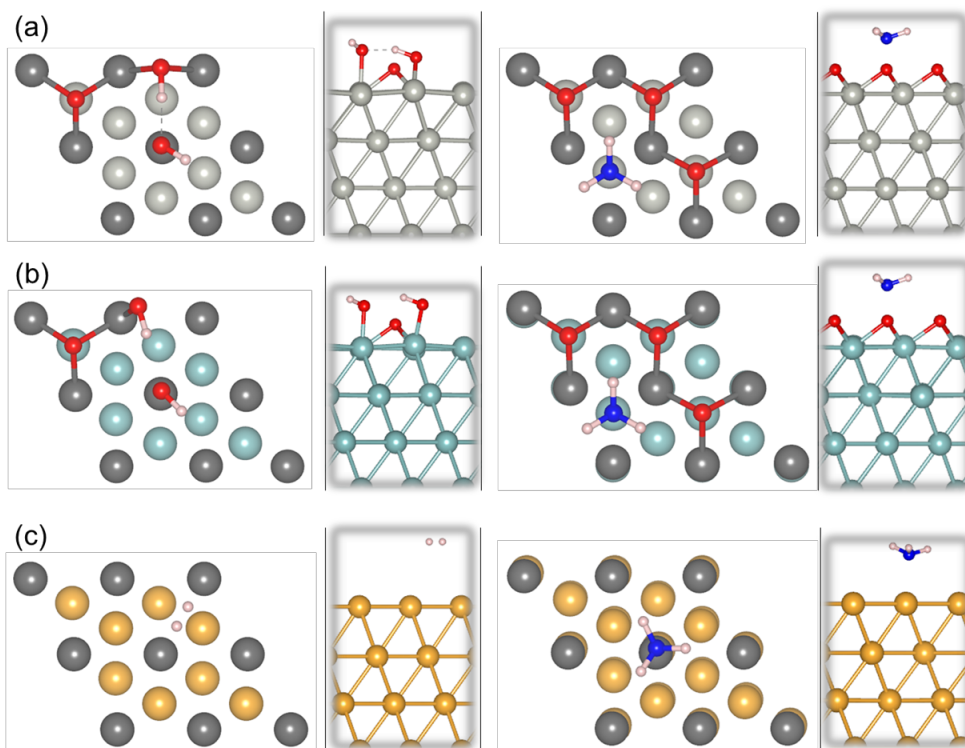


Figure 4.15. The binding structure of H_2 and NH_3 molecule on the bulk-like slab of (a) Pd, (b) Pt, and (c) Au.

4.4.3 Gas Adsorption on the Noble Metal Nanocone Cluster

Model

From the particle size difference observed in TEM images of Figure 4.3, the nanocone cluster model is considered for the Pt and Au decoration, which have the quantum dot size particles. Similar to the bulk-like slab model, surface oxidation is considered for the Pt nanocone cluster. The oxygen adsorption energy at the Pt nanocone surface along with the increase of coverage is provided in Figure 4.16. According to Figure 4.16, the surface oxidized Pt nanocone is the most stable when the whole surface is fully covered with oxygen atoms. The structure of modeled Au and Pt nanocone cluster is presented in Figure 4.17.

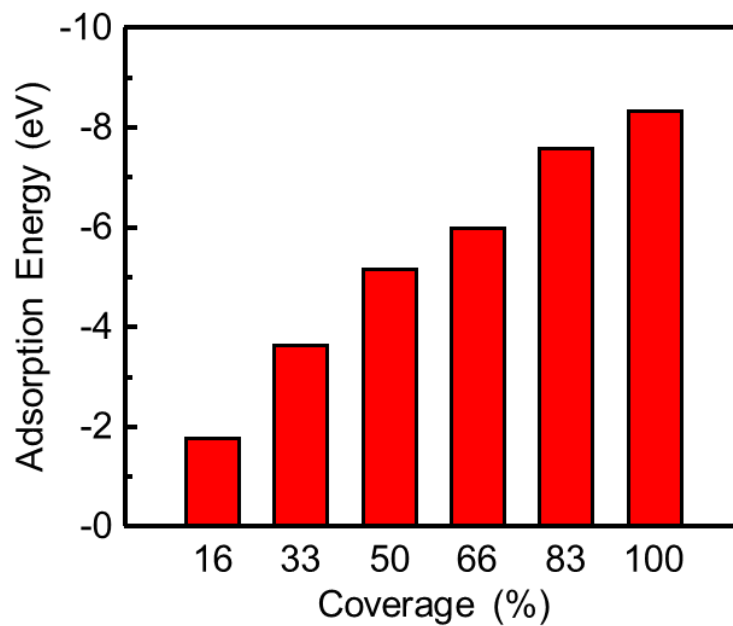


Figure 4.16. Oxygen adsorption energy on Pt nanocone cluster with variety of coverages.

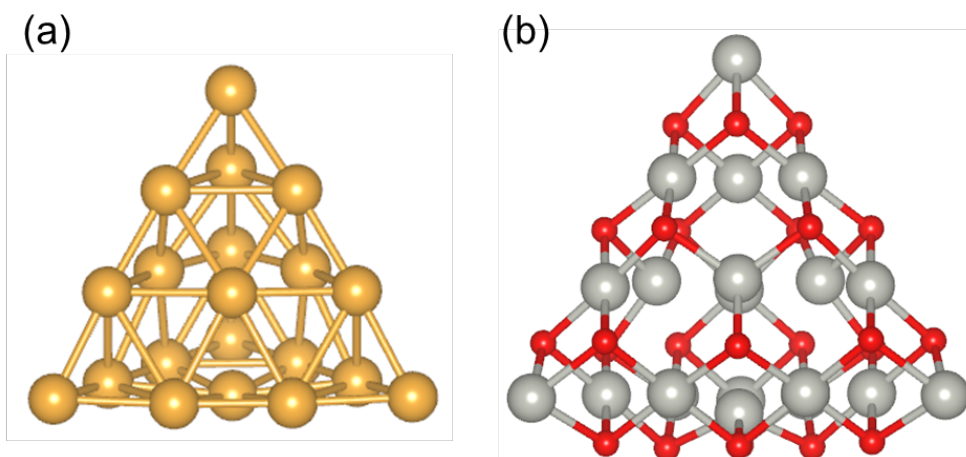


Figure 4.17. Nanocone cluster model of (a) Au and (b) Pt.

For Pt and Au, the binding energy of H_2 and NH_3 was calculated again

with the nanocone cluster model. The binding energy on Pt and Au nanocone clusters was 1.94 eV, 0.14 eV for H₂ gas molecule and 0.22 eV, 0.41 eV for NH₃ gas molecule. From Figure 4.18, it was possible to figure out that the binding energy of gas molecules decreased compared to the bulk-like slab when the nanocone cluster model is adopted. With the decrease of the binding energy for Pt and Au, the trend of the H₂ binding energy changed to be more consistent with that of the experimental response.

As the binding energy nicely reproduced the experimental results, we could confirm that the influence of the noble metal decoration can be understood from the binding energy calculation with various surface models. On the other hand, the binding energy of NH₃ still shows an inconsistent trend with response values, despite the adoption of the nanocone cluster model. To understand the mechanism of the NH₃ gas sensitivity change along with the various noble metal decoration, another factor is considered in the following chapter.

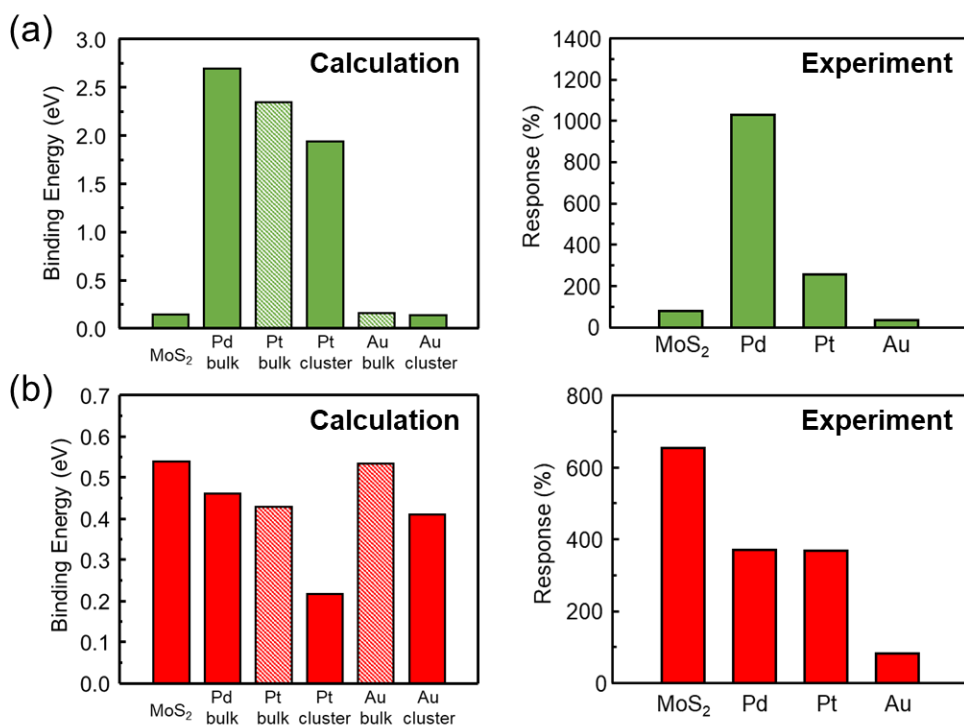


Figure 4.18. Comparison of calculated binding energy from bulk-like Pd slab, Au, Pt nanocone cluster and experimental response value for (a) H₂ gas and (b) NH₃ gas.

4.4.4 Coverage Effect of the Noble Metal NPs on the NH₃ Gas Sensitivity

From the binding energy values of NH₃ gas molecules in Figure 4.18, we could identify that the decorated noble particle is not a major binding site for the NH₃ gas molecule, as the binding energy is highest for pristine MoS₂ edge. This indicates that the sensitivity toward NH₃ gas of the noble metal decorated MoS₂ is strongly related to the extent of the exposed MoS₂ edge sites. As mentioned in chapter 4.2.2, the deposition of noble metal NPs is concentrated at the edge region of MoS₂, which is also shown from STEM images in Figure 4.3. The concentration of noble metal NPs at the edge region can be explained by the adsorption energy of the metal atom. In Table 4.5, the noble metal atom adsorption energy on the MoS₂ basal plane and edge site is presented. From the comparison of the adsorption energy, for every type of noble metal, the deposition at the edge site is thermodynamically stable.

	Basal plane (eV)	Edge (eV)
Au	-0.62	-1.65
Pd	-2.19	-2.30
Pt	-2.87	-5.17

Table 4.5. Adsorption energy of the noble metal atom at the MoS₂ basal plane and edge site.

From the major NH_3 binding site and region of noble metal NPs decoration, we could deduce that the decoration of noble metal NPs blocks the binding site, which disrupts the sensing of NH_3 gas. Here, the change in response for NH_3 gas varies with the extent how much the metal NPs are dispersed at the MoS_2 edge. In the case of Pd NPs, as can be inferred from large particle size, they prefer to grow in larger size rather than to be dispersed with small particles. For Pt and Au particles, in order to investigate the degree of distribution at the MoS_2 edge, the adsorption energy with an increasing number of metal atoms, which is also called the clustering energy, is calculated. Thermodynamically, the metal atoms are agglomerates until the clustering energy becomes positive. According to Figure 4.19, it is possible to assume that Pt tends to cluster strongly compared to Au. Even from the morphology of clustered metal atoms, Pt atoms have the tendency to be gathered, while Au atoms prefer to be dispersed. The evidence of Au NP dispersion can be also inferred from the surface energy of noble metals. According to Table 4.6, the surface energy of Au is much smaller than Pd and Pt. While the Pd NPs have larger sizes, Pt NPs with the size of 2~4 nm are forced to be agglomerated to stabilize the high surface energy. On the other hand, with the low surface energy, Au NPs widely dispersed along the MoS_2 edge rather than agglomerated form.

Finally, from the clustering energy and the surface energy of noble metals, we could conclude that the distribution of Au NPs is comparatively more dispersed than Pd or Pt NPs. Due to the widespread distribution of Au NPs

at the MoS₂ edge, there is a further block of the NH₃ binding site, which leads to a stiffer decrease of NH₃ sensitivity for Au NPs decorated MoS₂ sensor when compared to others.

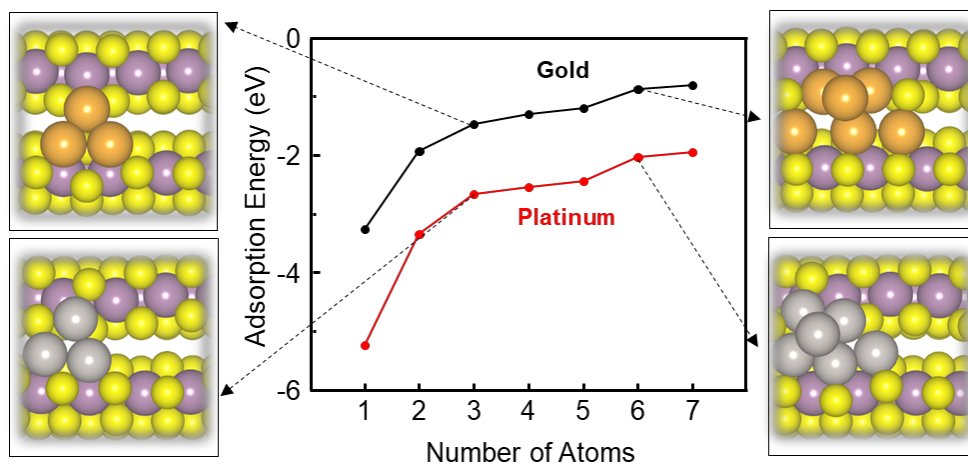


Figure 4.19. Clustering Energy of Au and Pt at the edge site of MoS₂. For the structure of clustered metal atoms in inset, each Mo, S, Au, and Pt atoms have the purple, yellow, orange, and grey color.

Bulk slab	Surface Energy (J/m ²)
Au	1.48
Pd	2.21
Pt	2.46

Table 4.6. Surface energy of the Au, Pd, and Pt slab with (111) surface

4.5 Conclusion

In summary, we investigated the mechanism of the modification of the sensitivity with various noble metal decorations. While the pristine MoS₂ has a high sensitivity toward NH₃, selectivity toward H₂ and C₂H₅OH gas was acquired through the decoration of Pd and Au NPs. The change of the selectivity was found to be primarily due to the variation of H₂ and NH₃ sensitivity compared to pristine MoS₂. From the TEM and XPS analysis, the difference in the particle size and surface oxidation in Pd, Pt NPs are identified. Based on the experimental results, the binding energy of the H₂ and NH₃ gas molecule was calculated for pristine MoS₂ first. By comparing the basal plane and the edge site, the edge site was confirmed as the main binding site for both gases and NH₃ shows higher binding energy than H₂, which explains the high NH₃ gas selectivity of the pristine MoS₂. Various models are adopted to imitate the gas adsorption on the noble metal decorated MoS₂. For the large-sized particle with surface oxidation, the bulk-like slab with surface oxygen model is adopted for Pd. For smaller particles of Au and Pt, the nanocone cluster model is used while the surface oxidation was considered only for Pt. For the H₂ gas molecule, the binding energy on the Pd and Pt increased relative to pristine MoS₂, due to the highly reactive surface adsorbed oxygen. Unlike H₂ gas, the binding energy on noble metal NPs is all decreased when compared to pristine MoS₂. Thus, the sensitivity is closely related to the portion of exposed MoS₂ edge sites.

From the clustering energy and surface energy, Au was identified to have the most dispersed distribution, severely blocking the binding site of NH₃ on MoS₂. From the interpretation of the selectivity improvement with the noble metal decoration, we presented the explanation by considering not only the conventional binding energy for H₂ gas sensing but also the coverage effect in NH₃ gas sensing. We believe that the novel approach in this study will contribute to the fabrication of sensors with high sensitivity and selectivity, even for the wider variety of materials.

4.6 References

- [1] D. Guo, D. Zhang, N. Li, L. Zhang, J. Yang, A Novel Breath Analysis System Based on Electronic Olfaction. *IEEE Trans. Biomed. Eng.* **2010**, *57*, 2753-2763
- [2] S. Dragonieri, M. P. van der Schee, T. Massaro, N. Schiavulli, P. Brinkman, A. Pinca, P. Carratu, A. Spanevello, O. Resta, M. Musti, P. J. Sterk, An electronic nose distinguishes exhaled breath of patients with Malignant Pleural Mesothelioma from controls. *Lung Cancer* **2012**, *75*, 326-331
- [3] A. D. Wilson, M. Baietto, Applications and Advances in Electronic-Nose Technologies. *Sensors* **2009**, *9*, 5099-5148
- [4] L. Zhang, F. Tian, H. Nie, L. Dang, G. Li, Q. Ye, C. Kadri, Classification of multiple indoor air contaminants by an electronic nose and a hybrid support vector machine. *Sens. Actuator B* **2012**, *174*, 114-125
- [5] Y.-S. Shim, K. C. Kwon, J. M. Suh, K. S. Choi, Y. G. Song, W. Sohn, S. Choi, K. Hong, J.-M. Jeon, S.-P. Hong, S. Kim, S. Y. Kim, C.-Y. Kang, H. W. Jang, Synthesis of Numerous Edge Sites in MoS₂ via SiO₂ Nanorods Platform for Highly Sensitive Gas Sensors. *ACS Appl. Mater. Interfaces* **2018**, *10*, 31594-31602
- [6] S.-Y. Cho, S. J. Kim, J.-S. Kim, W.-B. Jung, H.-W. Yoo, J. Kim, H.-T. Jung, Highly Enhanced Gas Adsorption Properties in Vertically Aligned MoS₂ Layers. *ACS Nano*, **2015**, *9*, 9314-9321

- [7] M. Sivakumar, K. Venkatakrishnan, B. Tan, Characterization of MHz pulse repetition rate femtosecond laser-irradiated gold-coated silicon surfaces. *Nanoscale Res. Lett.* **2011**, 6, 78
- [8] A. Elhage, A. E. Lanterna, J. C. Scaiano, Catalyst farming: reaction rotation extends catalyst performance. *Chem. Sci.* **2019**, 10, 1419
- [9] J. H. Kim, J. Y. Cheon, T. J. Shin, J. Y. Park, S. H. Joo, Effect of surface oxygen functionalization of carbon support on the activity and durability of Pt/C catalysts for the oxygen reduction reaction. *Carbon* **2016**, 101, 449-457
- [10] M. A. van Spronsen, J. W. M. Frenken, I. M. N. Groot, Observing the oxidation of platinum, *Nat. Commun.* **2017**, 8, 429
- [11] G. Kresse, J. Furthmuller, Efficient iterative schemes for ab initio total-energy calculations using a plane-wave basis set. *Phys. Rev. B* **1996**, 54, 11169-11186
- [12] G. Kresse, D. Joubert, From ultrasoft pseudopotentials to the projector augmented-wave method. *Phys. Rev. B* **1999**, 59, 1758-1775
- [13] P. E. Blochl, Projector augmented-wave method. *Phys. Rev. B* **1994**, 50, 17953-17979
- [14] S. Grimme, Semiempirical GGA-Type Density Functional Constructed with a Long-Range Dispersion Correction. *J. Comput. Chem.* **2006**, 27, 1787-1799
- [15] S. Grimme, J. Antony, S. Ehrlich, H. Krieg, A consistent and accurate ab initio parametrization of density functional dispersion correction (DFT-D) for the 94 elements H-Pu. *J. Chem. Phys.* **2010**, 132, 154104

[16] S. Grimme, S. Ehrlich, L. Goerigk, Effect of the Damping Function in Dispersion Corrected Density Functional Theory. *J. Comput. Chem.* **2011**, 32, 1456-1465

Abstract (in Korean)

다양한 촉매 반응 메커니즘 연구에 있어서, 각 촉매 물질의 표면 화학은 매우 중요한 요소이다. 모든 촉매의 반응 과정은 촉매 표면과 반응 물질 간의 상호 작용을 바탕으로 진행되므로 촉매 표면 상태에 대한 정확한 이해는 촉매 활성에 대한 해석과 직접적으로 연관된다. 오늘날, 다양한 반응에 대한 촉매의 활성을 예측, 해석하기 위하여 제일 원리 계산 기반 시뮬레이션 연구가 활발하게 진행되고 있다. 특히 하이스루풋 스크리닝(high-throughput screening)을 통한 경제적인 최적 촉매 물질 탐색은 시뮬레이션 연구의 궁극적인 목표라고 볼 수 있다. 하이스루풋 스크리닝에서 가장 필수적인 것은 촉매 반응에 대한 기술자 선정으로, 기술자는 실제 촉매 물질의 물성을 반영하면서 동시에 적은 계산 자원을 바탕으로 구할 수 있어야 한다. 이러한 기술자를 찾기 위해서는 촉매 반응에 대한 실험 및 이론적 연구 결과의 교차 검증은 바탕으로 한 반응 메커니즘의 이해가 기반이 되어야 한다. 따라서 촉매 반응 메커니즘을 정확히 예측하기 위하여는 앞서 언급한 촉매 표면 화학의 정확한 모사를 바탕으로 한 이론적 접근이 필수적이다. 다만 현재 대부분의 촉매 연구는 단일 물질만을 적용하는 경우는 거의 없는 실정이다. 대부분 촉매 활성의 추가적인 향상을 위하여 다양한 개질 전략들이 적용되고 있다. 이들 전략은 크게 구조 제어, 원자 단위 개질 그리고 조촉매 적용 등으로 분류할 수 있다. 본 논문에서는 위의 다양한 촉매 개질 전략의 적용이 촉매 특성에 영향을 미치는 메커니즘에 대하여 제일 원리 계산 기반의

시뮬레이션을 바탕으로 설명하였다.

첫 번째 연구에서는, 물 분해 촉매인 알파 상 철 수산화물의 활성을 향상시키기 위하여 최적의 전이 금속 도펀트를 찾고 이에 따른 특성 향상 메커니즘을 설명하였다. 먼저 전기전착법을 이용하여 좋은 결정성을 가지는 알파 상 철 수산화물을 합성하였고 이에 성공적으로 일정한 농도의 Mn, Co, Ni 도펀트를 도입하였다. 도펀트가 도입된 경우에도 알파 상 수산화물에서 상 분리, 형상 변화 및 결정성 변화가 나타나지 않음을 확인하였고, 이 때 Co에서 가장 우수한 촉매 특성이 나타남을 확인하였다. 도펀트 첨가에 따른 촉매 활성 변화 메커니즘을 규명하기 위하여 실험 결과를 바탕으로 시뮬레이션을 진행하였다. X선 회절 분석 결과를 바탕으로 알파 상 철 수산화물에서 주요하게 나타나는 (001), (021) 그리고 (111) 면을 모델링하였고, 해당 면에서 반응의 이론적 과전압을 계산하였다. 그 결과 (001)면이 가장 낮은 과전압을 가져 실제 반응에 주요하게 참여함을 확인할 수 있었다. 또한 (001)면에 도펀트 원자를 도입하여 도펀트 종류에 따른 이론적 과전압 값의 변화를 살펴보았다. 그 결과, 실험 결과와 마찬가지로 Co가 도핑된 모델에서 가장 낮은 과전압이 나타났다. 각 도펀트에서의 시뮬레이션 결과를 바탕으로 알파 상 수산화물에서의 volcano curve를 유도하였고 이 때 산소 흡착 반응 단계에서의 산소 p-band center가 촉매 활성의 기술자로 작용하는 것을 알 수 있었다. 본 연구에서는 촉매에서 나타나는 다양한 면 및 첨가된 도펀트 종류와 같은 변수에 의해 촉매의 활성이 변하는 메커니즘에 대해 성공적으로 설명하였다.

두 번째 연구는, Bi를 장식한 GaN 나노와이어를 이용한 고효율 이산화탄소 환원 촉매의 메커니즘을 주요하게 다루었다. 해당 실험은 동완재 박사가 진행하였고 본 연구는 실험 결과를 이론적으로 검증하는데 집중하였다. 실험 파트에서 GaN 나노와이어에 Bi를 장식한 경우 크게 두 가지 특성 변화가 나타나는 것을 확인할 수 있다. 첫번째로는 이산화탄소 환원 생성물 중 포름산에 대한 선택성이 크게 증가하였다. 두번째로는 전체적인 광전류가 눈에 띄게 증가하는 것을 확인할 수 있었다. 이러한 특성 향상을 설명하기 위하여 본 연구에서는 GaN, Bi₂O₃ 그리고 GaN-Bi₂O₃ 복합체를 모사하여 이산화탄소 환원 반응 단계 에너지를 계산하였다. Bi₂O₃의 경우 X선광전자분광법 결과, Bi가 완전히 산화된 것을 확인하여 위와 같이 모델링하였다. 먼저 생성물에 대한 선택성은 반응 중간체의 촉매 표면과의 결합 형태로 확인이 가능하였다. 포름산이 생성되는 경우는 반응 중간체의 산소가 촉매 표면과 결합을 이루고, 반대로 일산화탄소 및 여타 생성물이 발생하기 위해서는 반응 중간체의 탄소가 결합을 생성하여야 한다. 이 두 가지 반응 경로에 대하여 반응 결정 단계의 배리어를 각 모델링에서 계산하였을 때, Bi₂O₃가 존재하지 않을 경우는 일산화탄소 및 포름산 생성 반응의 배리어 차이가 거의 없었지만 (1.93 eV, 2.10 eV), Bi₂O₃ 존재 시 포름산 생성 반응의 배리어만 크게 감소함 (1.04 eV)을 확인할 수 있었다. 이를 바탕으로 비스무스 장식이 포름산 선택성에 주요한 역할을 함을 확인하였다. 또한 광전류의 증가는 GaN-Bi₂O₃ 복합체의 전자 구조 분석을 통해 설명할 수 있었다. GaN에 Bi₂O₃가 장식될 경우 Bi₂O₃에 의하여 전도띠가 낮은 에너지 준위로 이동하고

이에 따라 두 물질의 계면에 빌트인 퍼텐셜이 생성된다. 이에 따라 광전자의 촉매 표면으로의 이동이 촉진되어 광전류값이 크게 향상되는 것임을 확인하였다. 본 연구에서는 GaN과 Bi_2O_3 의 상이한 표면 화학에 따른 반응 메커니즘 변화, 그리고 Bi_2O_3 조촉매 적용에 따른 물질 계면에서의 전자 이동이 촉매 활성에 미치는 영향에 대해 이론적인 설명을 제시하였다.

세번째 연구는, MoS_2 가스 센서에 귀금속 입자를 장식하는 것으로 다양한 기체에 대해 선택성 확보 및 선택성 변화 메커니즘 규명을 주요하게 다루었다. 본 연구의 실험은 박서연 박사 및 김태훈 연구원이 진행하였다. 기존의 MoS_2 센서의 경우 암모니아에 대한 감도 및 선택성이 우수함을 확인할 수 있었다. MoS_2 센서에 귀금속을 장식한 경우, 기존 감도 값에서 수소와 암모니아의 감도가 크게 변화하는 것을 확인하였다. Pd와 Pt가 장식되었을 때 두 경우 모두 수소 감도가 증가하고 암모니아 감도가 감소하였고, Au가 장식된 경우는 암모니아 감도만 크게 감소하였다. 이 때 Pd의 경우 수소 감도 증가가 매우 커 수소에 대한 선택성이 우수하였고, Au의 경우는 암모니아 감도가 감소하면서 기존 에탄올의 감도가 상대적으로 크게 나타나 에탄올에 대하여 선택성을 획득하였다. 센서 특성 측정에서, 귀금속 장식에 따른 감도 변화는 수소와 암모니아에 대해 주요하게 나타나므로 시뮬레이션에서는 두 기체의 결합 에너지만을 고려하였다. 시뮬레이션 파트에서는 먼저 MoS_2 센서의 선택성을 결합 에너지를 바탕으로 확인하였다. MoS_2 의 바닥면의 경우 낮은 활성으로 인해 기체가 거의 흡착되지 않는 반면, MoS_2 의 모서리에서는 수소와 암모니아

모두 더욱 강하게 결합하였다. 또한 수소와 암모니아의 결합 에너지를 비교하였을 때 암모니아의 결합 에너지가 더욱 커서 실험에서 나타나는 MoS_2 의 높은 암모니아 감도는 주로 모서리가 주요한 결합 위치로 작용함에 따라 나타나는 특성임을 확인하였다. 귀금속 장식을 모사하기 위해서 본 연구에서는 다양한 모델을 적용하였다. 이 때 모델링을 위하여 여러 분석 결과를 참조하였는데, 먼저 투과전자현미경 분석을 통해 Pd가 20~30 nm, Pt와 Au가 2~3 nm의 입자 크기를 가지는 것을 확인하였다. 또한 X선광전자분광법 결과 Pd와 Pt 입자에 대해서만 표면에 산화과 일어났음을 발견하였다. 분석 결과를 종합하여, Pd의 경우 bulk-like한 표면 산화된 (111)면을 모델링하였고, 입자 크기가 작은 Pt와 Au는 20개의 원자로 이루어진 정사면체 형태의 클러스터 모델을 적용하였다. 이때 Pt는 Pd와 마찬가지로 표면 산화를 고려하였다. 이러한 모델링을 바탕으로 기체의 결합 에너지를 계산한 결과, 먼저 수소의 경우 Pd 및 Pt 모델에서 MoS_2 대비 높은 결합 에너지를 가지는 것이 밝혀졌다. 이 때 수소의 결합 에너지 증가는 두 금속 입자 모델의 표면 산소가 수소와 강한 결합을 형성함에 따라 나타나는 현상임을 확인하였다. 수소의 경우 결합 에너지와 측정된 감도의 경향성이 거의 일치한 반면 암모니아는 그렇지 못하였다. 측정값과 같이 귀금속 모델에서 암모니아의 결합 에너지는 모두 MoS_2 보다 작은 값을 가졌지만 경향성이 다르게 나타났다. 즉 이는 결합 에너지는 암모니아 감도를 설명하기엔 적절치 못한 지표임을 뜻한다. 암모니아의 경우 수소와의 차이는 모든 귀금속에 대해 가장 열역학적으로 안정한 결합 위치가 귀금속이 아닌 MoS_2 모서리라는 것이다. 즉 이것은

결국 금속 입자에서의 결합 에너지보다는 각 귀금속 입자가 장식되었을 때 기존의 MoS_2 모서리가 어느 정도 노출되어 있는가가 실질적으로 감도 변화에 직결됨을 뜻한다. 먼저 Pd의 경우는 입자 크기가 커 상대적으로 분산 정도가 덜하므로 노출된 MoS_2 모서리가 많음을 확인할 수 있었다. 입자 크기가 같은 Pt, Au의 분산 정도를 확인하기 위해 두 금속의 표면 에너지와 클러스터링 에너지를 계산하였다. 그 결과 Pt의 경우 클러스터링 에너지 및 표면 에너지가 커 작은 입자의 경우 표면을 안정화시키기 위하여 집합체를 형성하는 반면 상대적으로 Au는 분산되어 분포함을 확인할 수 있었다. 그 결과 Au 입자는 암모니아 기체의 결합 위치 차폐율이 높아 상대적으로 더 큰 암모니아 감도 감소가 일어난 것임을 확인하였다. 본 연구에서는 표면 산화에 따른 결합 에너지 변화 및 입자 크기, 촉매의 분포 형태가 기체 감도에 미치는 영향을 성공적으로 설명하였다.

본 박사학위 논문은 위의 결과를 바탕으로 여러 촉매 반응에 있어 다양한 개질 전략이 가지는 효과를 제일 원리 계산 시뮬레이션을 통해 성공적으로 설명할 수 있음을 보였다. 본 연구의 촉매 활성 향상 메커니즘에 대한 이론적 접근은 다른 다양한 촉매 반응 및 물질에서의 개질 전략에 대한 방향성을 제시할 수 있고 이를 바탕으로 최적의 촉매 활성 확보를 기대할 수 있다.

키워드: 제일 원리 계산, 표면 화학, 촉매, 물 분해, 이산화탄소 환원, 가스 센서

학번: 2016-20817

성명: 이태형